ANTENNA INTEGRATION FOR WIRELESS AND SENSING APPLICATIONS

A Dissertation
Presented to
The Academic Faculty

by

Terence Wu

In Partial Fulfillment
of the Requirements for the Degree
Doctor of Philosophy in the
Electrical and Computer Engineering

Georgia Institute of Technology
August 2011

ANTENNA INTEGRATION FOR WIRELESS AND SENSING APPLICATIONS

Approved by:

Dr. Manos Tentzeris, Advisor
School of Electrical and Computer
Engineering
Georgia Institute of Technology

Dr. Ian Akyildiz
School of Electrical and Computer
Engineering
Georgia Institute of Technology

Dr. Andrew Peterson
School of Electrical and Computer
Engineering
Georgia Institute of Technology

Dr. Yang Wang
School of Civil and Environmental
Engineering
Georgia Institute of Technology

Dr. Mark Allen
School of Electrical and Computer
Engineering
Georgia Institute of Technology

Dr. Krishna Naishadham
School of Electrical and Computer
Engineering
Georgia Institute of Technology

Date Approved: April 22, 2011

To my family and friends.

ACKNOWLEDGEMENTS

TABLE OF CONTENTS

LIST OF TABLES

LIST OF FIGURES

SUMMARY

As integrated circuits become smaller in size, antenna design has become the size limiting factor for RF front ends. The size reduction of an antenna is limited due to tradeoffs between its size and its performance. Thus, combining antenna designs with other system components can reutilize parts of the system and significantly reduce its overall size. The biggest challenge is in minimizing the interference between the antenna and other components so that the radiation performance is not compromised. This is especially true for antenna arrays where the radiation pattern is important.

Antenna size reduction is also desired for wireless sensors where the devices need to be unnoticeable to the subjects being monitored. In addition to reducing the interference between components, the environmental effect on the antenna needs to be considered based on sensors' deployment.

This dissertation focuses on solving the two challenges: 1) designing compact multi-frequency arrays that maintain directive radiation across their operating bands and 2) developing integrated antennas for sensors that are protected against hazardous environmental conditions.

The first part of the dissertation addresses various multi-frequency directive antennas arrays that can be used for base stations, aerospace/satellite applications. A cognitive radio base station antenna that maintains a consistent radiation pattern across the operating frequencies is introduced. This is followed by multi-frequency phased array designs that emphasize light-weight and compactness for aerospace applications. The

size and weight of the antenna element is reduced by using paper-based electronics and internal cavity structures.

The second part of the dissertation addresses antenna designs for sensor systems such as wireless sensor networks and RFID-based sensors. Solar cell integrated antennas for wireless sensor nodes are introduced to overcome the mechanical weakness posed by conventional monopole designs. This can significantly improve the sturdiness of the sensor from environmental hazards. The dissertation also introduces RFID-based strain sensors as a low-cost solution to massive sensor deployments. With an antenna acting as both the sensing device as well as the communication medium, the cost of an RFID sensor is dramatically reduced. Sensors' strain sensitivities are measured and theoretically derived. Their environmental sensitivities are also investigated to calibrate them for real world applications.

Chapter 1

INTRODUCTION

1.1.   Motivation

Radio frequency (RF) systems have progressed significantly over the past 20 years with the advancements in cellular devices and the mobile network. MAC layer improvements such as OFDM and CDMA have increased the throughput and range dramatically from the analog methods [1]. At the same time, advancements in miniaturization and system integration such as system-on-chip, system-on-package and system-in-package have reduced the physical size and hardware cost of these devices from the original Motorola Dyna 8000X [2],[3]. With mobile data traffic exceeding 400 petabytes in 2009, the trend of higher throughput, longer range, and smaller form factor will continue into 4G LTE wireless broadband [4]. These technological enhancements also enable other sensing and tracking applications, from radio frequency identification (RFID) and wireless sensor network (WSN) to aerospace vehicles [5]-[8].

As integrated circuits become smaller in size, antenna design has become the size-limiting factor for RF front ends [9]-[11]. Important antenna parameters such as bandwidth and efficiency are compromised when reducing its size below the operating wavelength [12]-[14]. Thus, combining the antenna with its system can significantly improve the performance and compactness of a system by reutilizing the system area.

Two types of antenna integration exist in the literature: (1) multi-frequency integration, which combines different frequency antennas while considering their coupling effects in the near-field and their overall radiation pattern [15], and (2) package integration, which optimizes antennas with other system components and/or packaging to achieve better performance in a smaller form factor [16][17][18]. In some cases, both of these methods can be applied at the same time to further reduce size at the cost of design complexity. The type of integration and topology selected is heavily dependent on the specifications that best fit the application: frequency, bandwidth, gain, orientation, size, cost, etc.

The challenges in integration are reducing antenna size, loss of directionality, and minimizing the surrounding near-field effects to the antenna (impedance detuning, gain reduction, and radiation pattern distortion). Shrinking the antenna often results in poor efficiency and narrow bandwidth [19]-[24]. The radiation pattern is greatly altered by nearby metals or larger radiators; thus many multi-frequency designs appear in mobile applications where directionality is not needed. Also, when these large metals are packaged close to an antenna, the antenna will be detuned due to the near-field coupling, leading to further optimization or undesirable performance. Minimizing the near-field effects can eliminate excessive antenna optimizations. Alternatively, if a designer can modify the packaging to his/her advantage, antennas with smaller feature sizes can be obtained.

1.2. Objective

The objective of this work is to (1) develop compact multi-band antenna arrays suitable for base stations and aerospace vehicles and (2) miniaturize sensors by

2

integrating antennas with existing wireless sensor nodes and RFID tags. Designs that minimize the antenna-to-antenna coupling and the radiation pattern distortion are demonstrated in the multi-band antenna array designs. On the other hand, antenna designs on sensors address the antenna interference with system components and environmental conditions.

The dissertation is organized as follows:

Chapter CHAPTER 2 reviews the techniques of conventional multi-band antennas and introduces a compact multi-band unidirectional antenna. It demonstrates the use of symmetry to reduce beam tilting of the element at various frequencies.

Chapter CHAPTER 3 describes a base station antenna for cognitive radio. This antenna is capable of delivering all of the existing commercial wireless standards from 800 MHz to 6 GHz with similar radiation pattern. This antenna makes it easier for wireless operators to plan their coverage area.

Chapters CHAPTER 4 and CHAPTER 5 address the need for multi-band phased array for aerospace applications where light weight, beam steering, and aerodynamics becomes a concern. Chapter CHAPTER 4 starts with a paper based dual-frequency array to reduce the antenna weight. Chapter CHAPTER 5 enhances the design by covering three frequencies with a frequency separation of 16 to 1 while reducing the overall antenna thickness to $\lambda/36$. This design has the potential of becoming the foundation of conformal phased arrays that dramatically improve the aerodynamics of the design.

Chapter CHAPTER 6 discusses methods of integrating antennas with solar cells that would enable autonomous wireless sensor nodes in outdoor environments. Since antennas and solar cells both need to be placed on the exterior of a sensor to be effective,

combining these two components in the same design becomes a packaging challenge. Methods of reducing the interference between the antenna and solar cells while providing a low-profile design for the sensor is introduced.

Chapter CHAPTER 7 introduces a low-cost, wireless strain sensor that is achieved by using RFID technology. By eliminating the complex analog-to-digital converter and transceivers in the sensor, the cost of a single sensor is reduced. To reduce the environmental effects on the sensor, temperature and humidity sensitivity are identified so that their effects can be calibrated out of the measurement.

Finally, Chapter CHAPTER 8 summarizes the contributions in this dissertation and suggests future research directions.

Chapter 2

MULTI-FREQUENCY ANTENNAS: BASIC CONCEPTS

2.1. Introduction: Omnidirectional Multi-band Antennas

In the past 20 years, two trends have emerged in the evolution of cellular designs: (1) aesthetic improvement with a compact form factor and (2) expansion of wireless connectivity to support worldwide operation and multimedia data. To continue this trend, a compact antenna that can operate in both current and future wireless standards is needed. This is an extremely competitive research area where commercial phone developers such as Apple, RIM, Nokia, and Motorola, and academia are continuously seeking better solutions. The wireless standards can be categorized into four main frequency bands of interest: traditional cellular service around 900 MHz, broadband cellular service and WLAN from 1.7-2.4 GHz, WiMAX spectrum between 3.3-3.6 GHz, and WLAN/WiMAX standards between 5.1-5.9 GHz. A desired cellular antenna needs to have: (1) low-cost manufacturing methods, (2) a compact size for ease of integration and portability, (3) high radiation efficiency for better quality of service and reduced power consumption, (4) an omnidirectional pattern to allow maximum user mobility and (5) wideband return loss matching that makes the device operable under more wireless standards, and less susceptible to environmental detuning [25].

Several techniques have been reported while attempting to meet these multi-band requirements. Techniques such as additional slots [25]-[27], and multiple wire paths [28][30][31] can create multiple resonances for multi-band operations. Electromagnetic

coupling can also be used to extend the bandwidth of operations [29]-[31]. These multi-band designs are good for omnidirectional operation, but are not suitable for direct point to point communication. However, some of these multi-band techniques can be reapplied to realize directive multi-band antennas.

2.2.   Unidirectional Multi-band Antennas

In this section, a step-by-step process of designing a point-to-point multi-band antenna is described. This is a detail description of Ronglin Li's work in [32] that was not included in the conference proceeding. The design combines the multiple-wire-paths concept with structure symmetry to achieve a compact, directive antenna across 3 different frequencies. The frequencies of interest for the design are the WLAN/WiMax frequencies at 2.4-2.5 GHz, 3.3-3.6 GHz, and 5.1-5.9 GHz bands. A dual-band antenna design covering 2.5 and 5.5 GHz frequency bands is first introduced, and later extended to cover the 3.5 GHz band.

2.2.1. Dual-band Antenna

The dual-band unidirectional antenna is first investigated. The structure begins with a blade dipole above a ground plane at the lower frequency of 2.4GHz-2.5GHz. A Rogers RT/Duroid 5880 (ε_r=2.2) 20 mils (0.5mm) substrate was used to construct the microstrip feed and radiator of the blade dipole. The dipole is placed H = 12 mm above a ground plane to provide enough antenna bandwidth around the 2.45 GHz band. Then two radiating dipoles operating at 5.5 GHz are added around the low-frequency dipole structure symmetrically as shown in Figure 2.1. The symmetry along the Y axis is needed to overcome the high-frequency pattern distortion from the center dipole element. The antenna is fed from a 50Ω, 0.085" semi-rigid coaxial cable that connects to the microstrip

line stub on the top of the substrate. The semi-rigid cable holds the antenna above a 100 mm × 60 mm copper ground plane.
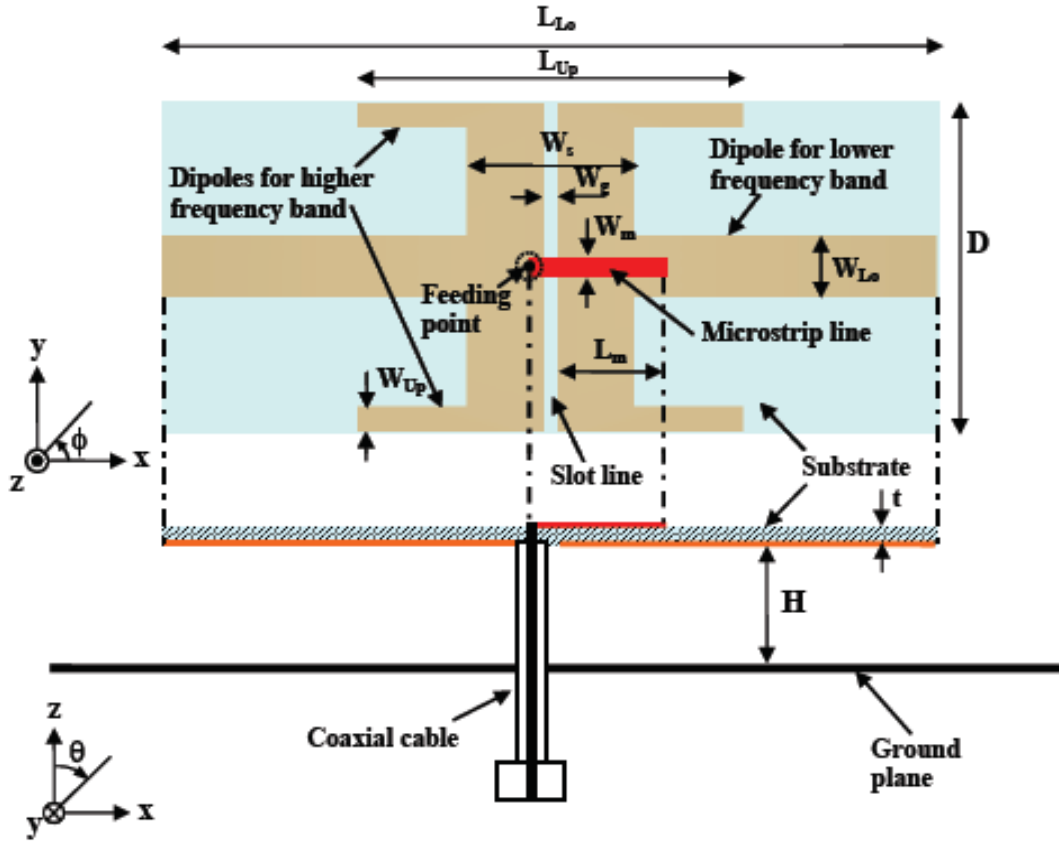
Figure 2.1 Dual-band unidirectional antenna dimensions. L_{Up}=30mm, L_{Lo}=60mm, H=12mm, D=26mm, W_{Up}=2mm,W_{Lo}=5mm, W_g=1mm, W_s=13mm, W_m=1.5mm, L_m=10mm, t=0.5mm.

The structure is simulated by a commercial time-domain solver, CST Microstripes [33]. The simulated current distribution in Figure 2.2 shows that the low frequency resonance correlates to the center dipole while the high frequency resonance excites the dipole pair on the sides. The technique of multiple wire path in omnidirectional antennas [28][30][31] applies to the unidirectional structure.

7

(a) At 2.45 GHz.

(b) At 5.5 GHz.

Surface current (dB)
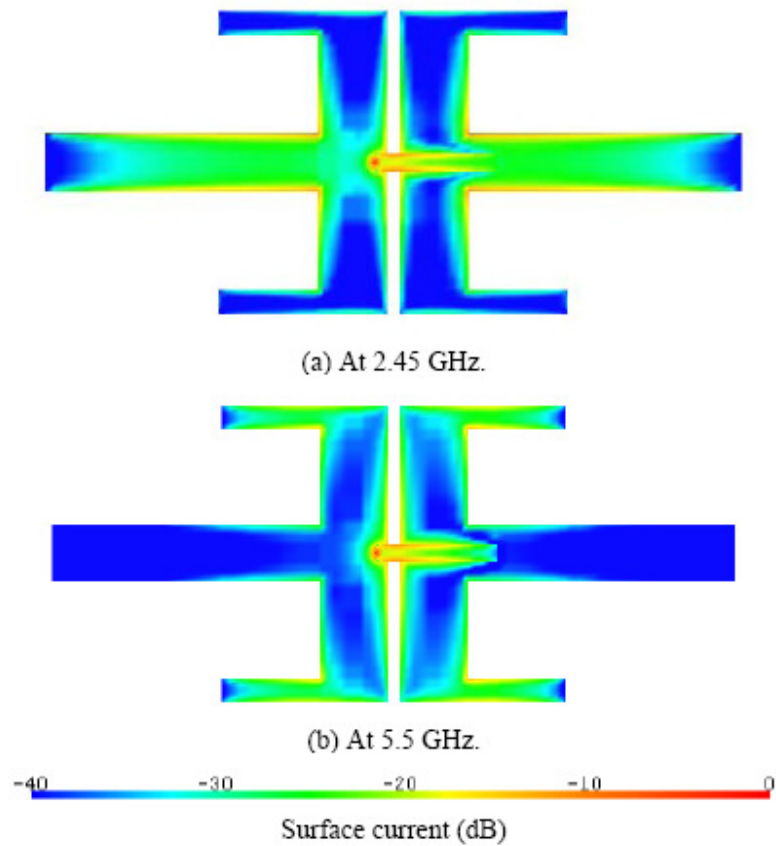
Figure 2.2 Current distribution of dual band antenna.

Figure 2.3 summarizes the simulated and measured return loss of the structure with the respective radiation patterns at those frequencies. The return loss measured by a VNA agrees with the simulated result. Also notice that several monopole modes are observed at 1.4 GHz and 3.2 GHz. The resonance at 1.4 GHz is caused by the outer coaxial feed that connects the bottom ground plane to one of the dipole blades. Monopole modes are not desirable modes of operation in this case.
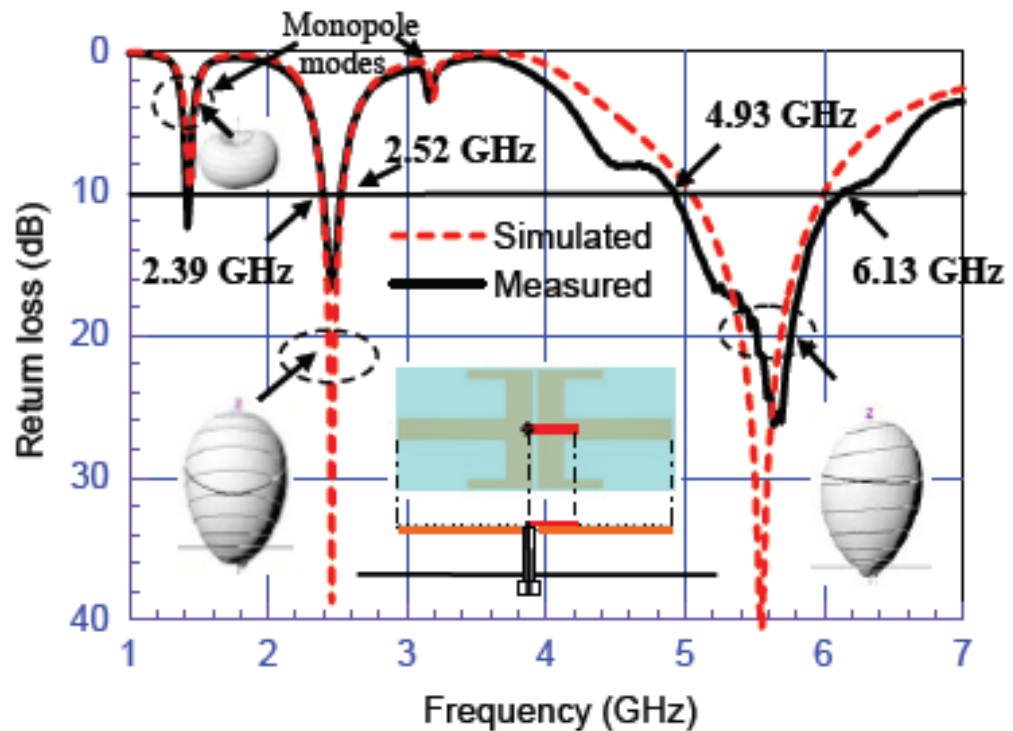
Figure 2.3 Return loss and radiation pattern of dual-band antenna.

2.2.2. Compact Dual-band Antenna

Reducing the overall size is desirable for the dual-band design. This is achieved by using top-loading at the end of the center dipole. In a sense, the low frequency dipole is folded equally along the width direction to create the needed 0.5λ resonance length. The folding reduces the length dimension of the structure.

The dipole and the microstrip feed line is created on a RT/Duroid 5880 20 mils substrate. The antenna dimensions are listed in Figure 2.4. Similar to the original dual band antenna, the structure is simulated with CST Microstripes. It is fabricated by feeding the antenna with a 0.085" semi-rigid coaxial cable through a copper ground plane (100 mm × 60 mm).

9
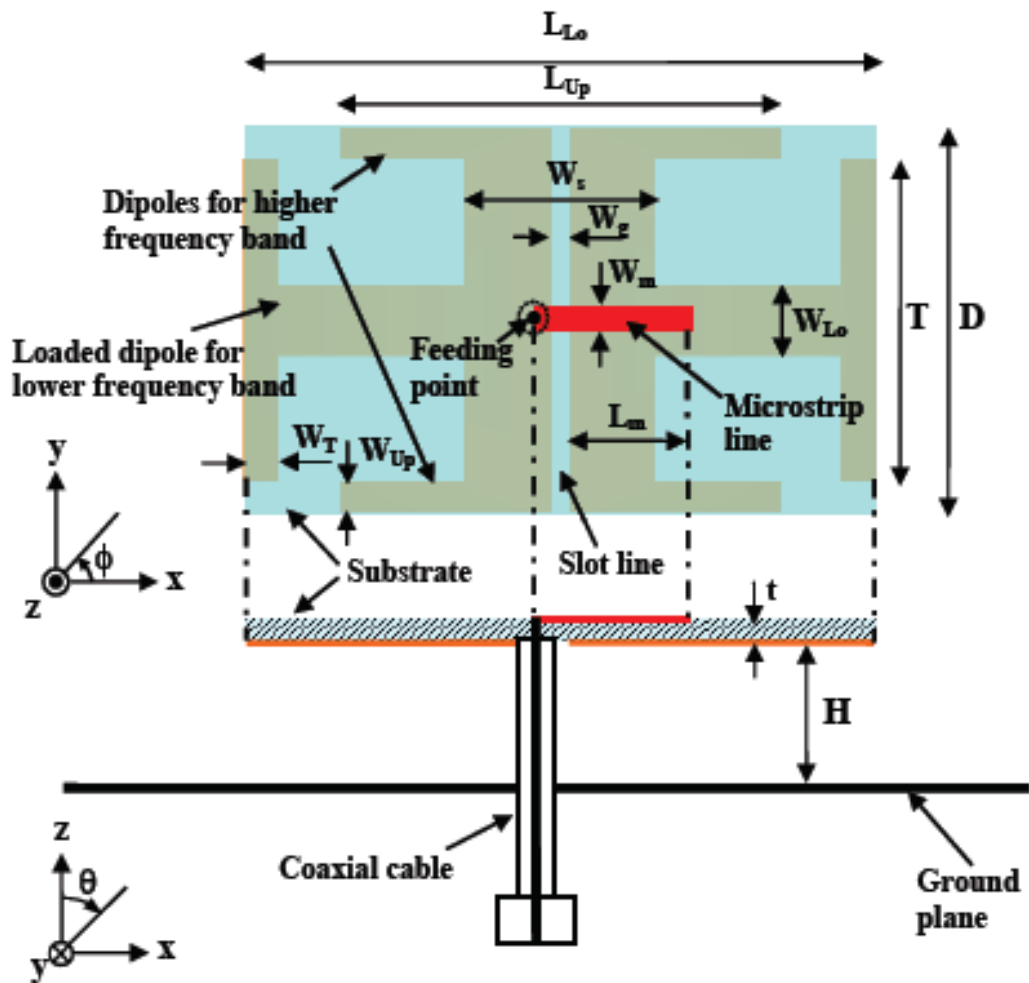
Figure 2.4 Compact Dual-band unidirectional antenna dimensions. L_{Up}=30mm, L_{Lo}=46mm, H=12mm, D=26mm, W_{Up}=2mm, W_{Lo}=5mm, W_T=2mm, W_g=1mm, W_s=13mm, W_m=1.5mm, L_m=11mm, t=0.5mm, T=20mm.

The simulated and measured return loss is shown in Figure 2.5. The compact design has a similar return loss and radiation performance as the original dual band antenna. Thus, top-loading reduced overall length of the antenna without much change in the resonance.
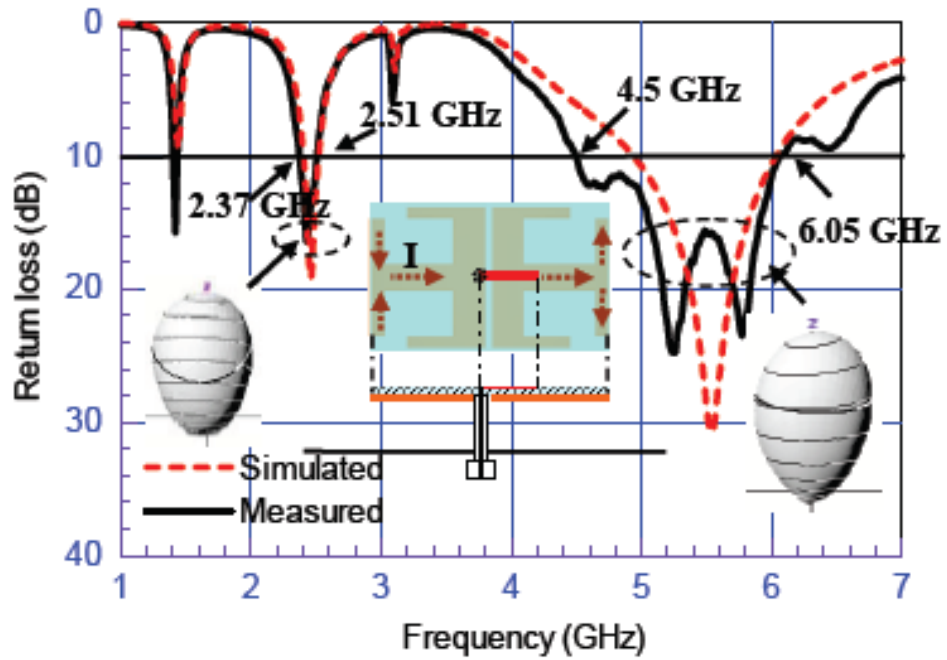
Figure 2.5 Return loss and radiation pattern at various frequencies for the compact dual-band antenna.

2.2.3. Compact Triple-band Antenna

The compact triple-band antenna is shown in Figure 2.6. Two 3.5 GHz dipole arms spaced 7 mm apart are added symmetrically around the center dipole. The length of the top-loading (T) and the dipole width (W_{Lo}) of the low-frequency dipole is reduced to fit the 3.5 GHz radiators. Since W_{Lo} determines the ground size of a microstrip line mode for the feed line, W_{Lo} is kept at 3 mm. The antenna construction is similar to the previous designs. The antenna and microstrip feed layers are constructed on a 20 mils Rogers 5880 substrate. The substrate is then fed by a 50 Ω semi-rigid coaxial cable 12 mm above a copper ground plane (100 mm × 60 mm). The antenna is simulated with CST Microstripes.

11
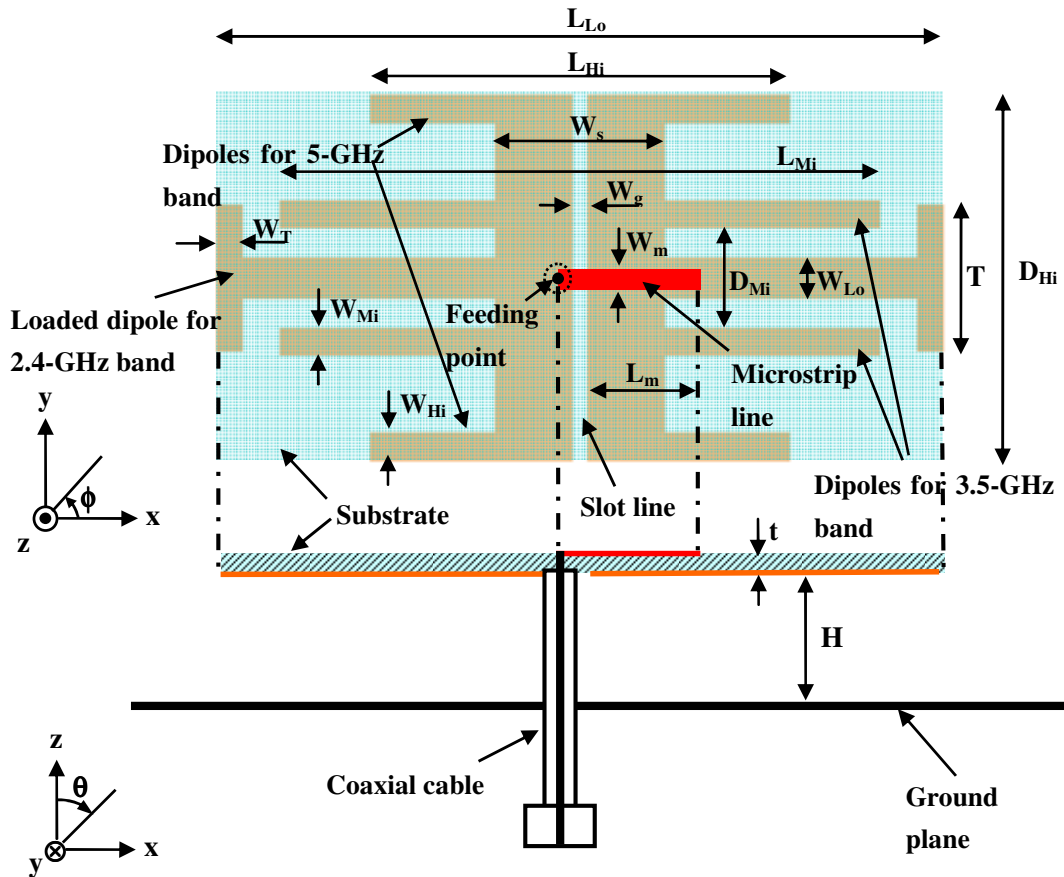
Figure 2.6 Configuration of a triple-band unidirectional planar antenna L_{Up}=30mm, L_{Lo}=52mm, H=12mm, D_{Mi}=7mm, D_{Hi}=26mm, W_{Up}=2mm, W_{Mi}=2mm, W_{Lo}=3mm, W_T=2mm, W_g=1mm, W_s=13mm, W_m=1.5mm, L_m=10mm, t=0.5mm, T=10mm.

The simulated and measured return loss results are shown in Figure 2.7. An additional resonance at 3.5 GHz is observed. The simulated radiation pattern shows that the antenna is unidirectional at each operating frequency. Return loss performance is very similar to the previous designs with an additional resonance at 3.5 GHz.
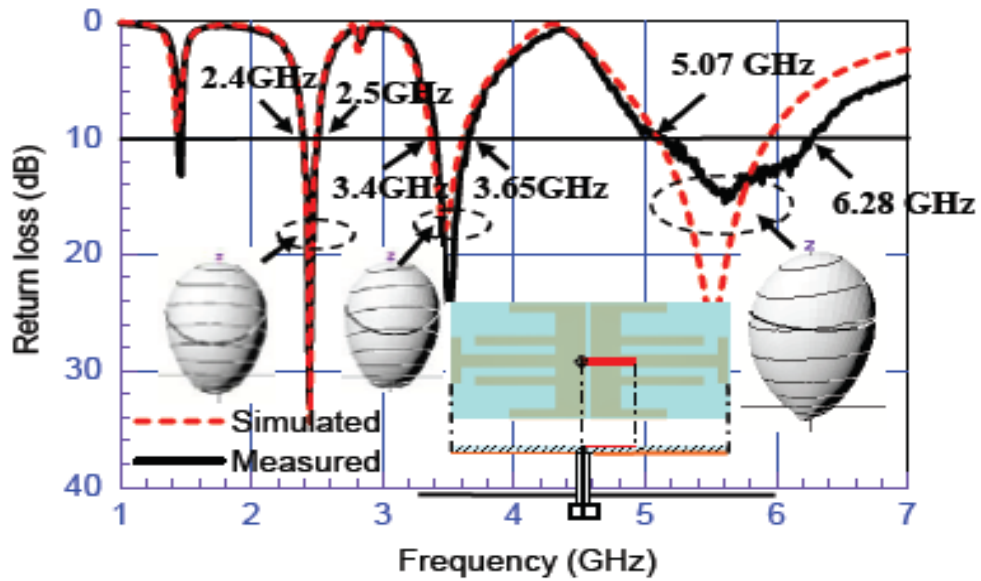
Figure 2.7 Return loss and radiation pattern for the compact triple-band antenna

The radiation pattern is measured in SATIMO's anechoic chamber with a setup shown in Figure 2.8. The gain measured at various frequencies matches with the CST Microstripes simulations as shown in Figure 2.9. Higher gain is expected for the high-frequency elements because the radiation comes from 2 radiators spaced further away. The radiation pattern at the center frequencies of band 1, 2, and 3 are shown in Figure 2.10, Figure 2.11, and Figure 2.12, respectively. Comparing the three figures, the 3 dB beamwidth of the antenna is narrower for the higher frequencies along the φ=90° direction. This is because the radiating arms are separated further apart for the higher frequency elements. As the separation approaches 0.5λ of the operating frequency, the radiating beamwidth reduces.

13
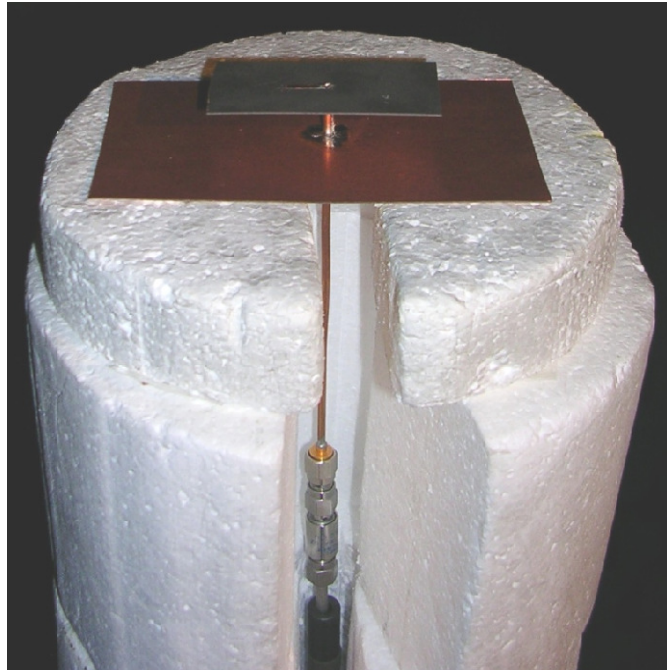
Figure 2.8 Fabricated antenna in anechoic chamber setup.
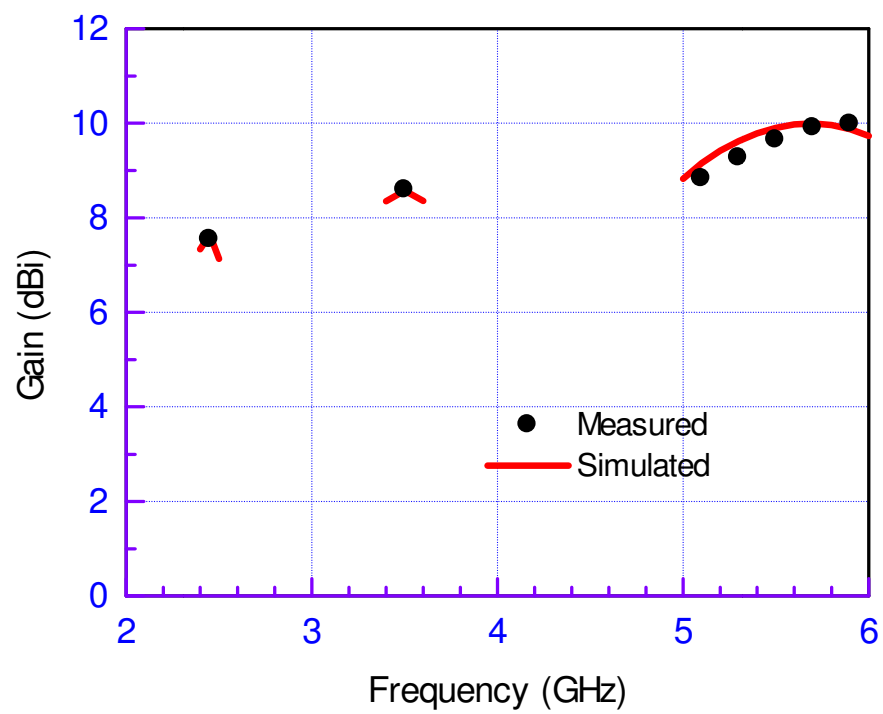
Figure 2.9 Antenna gain at the three operating frequencies
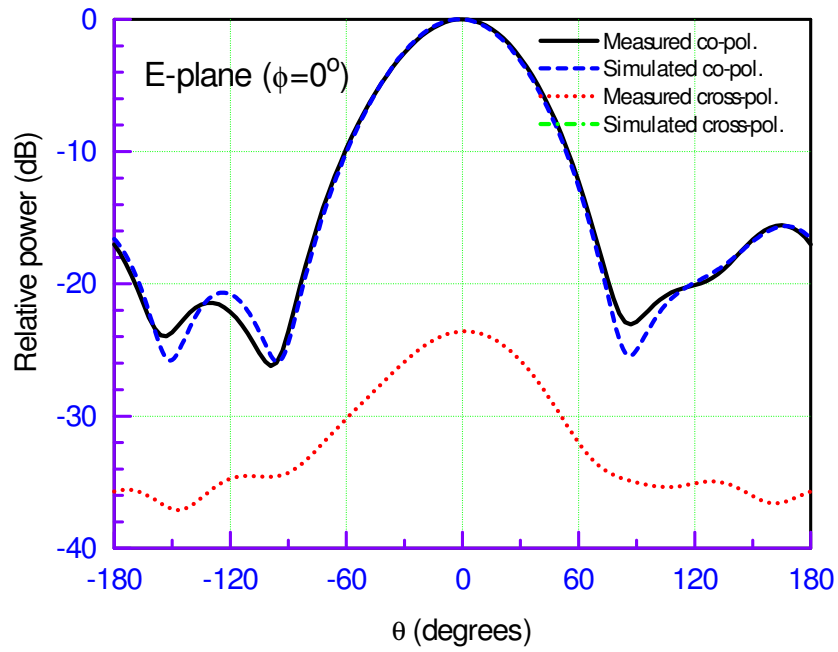
(a)
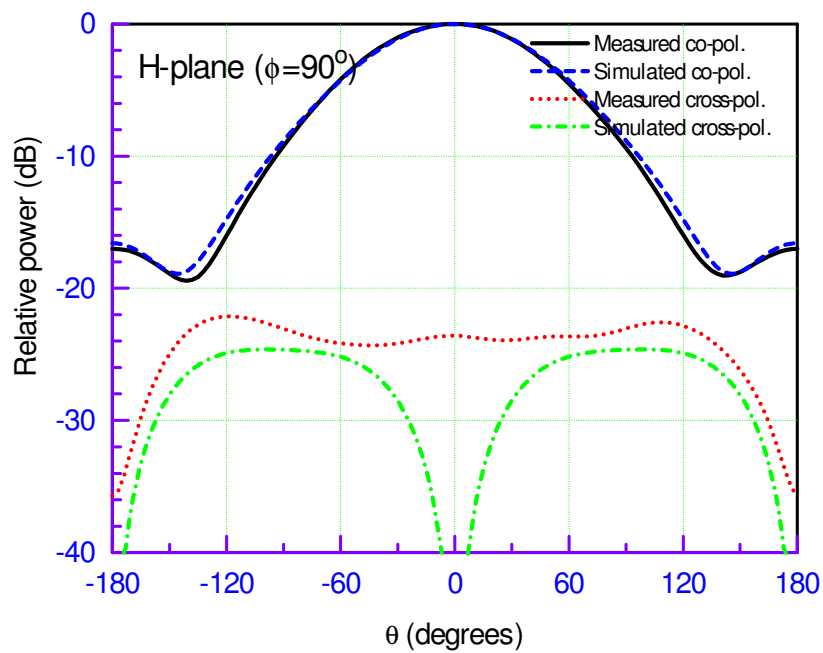
(b)

Figure 2.10 Normalized radiation pattern at 2.45 GHz (a) E-plane φ = 0° (b) H-plane φ = 90°
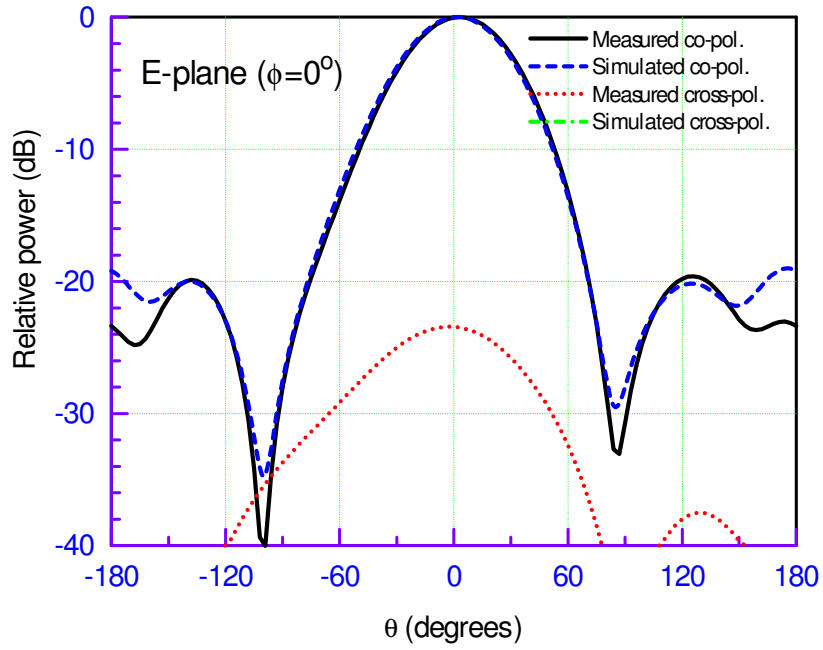
(a)
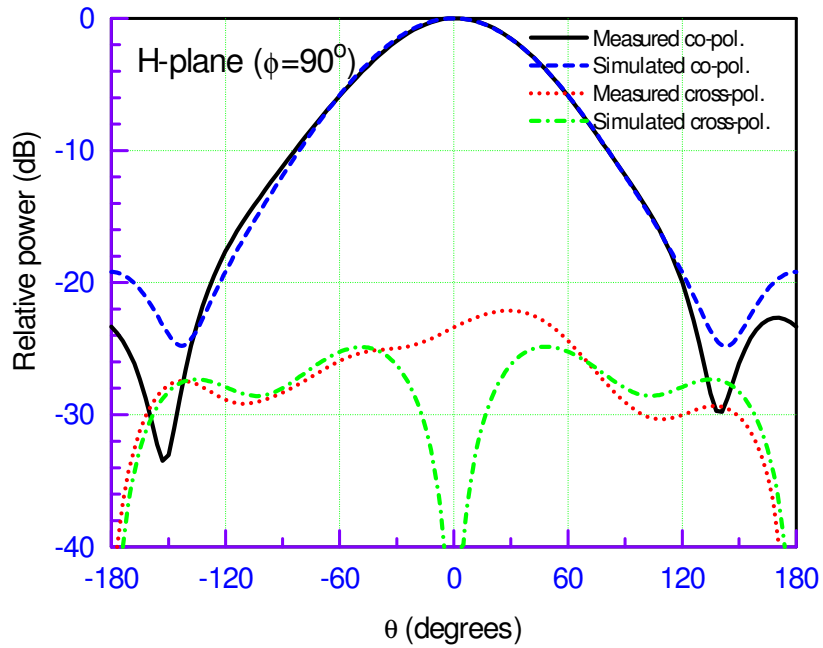
(b)

Figure 2.11 Normalized radiation pattern at 3.5 GHz (a) E-plane φ = 0° (b) H-plane φ = 90°
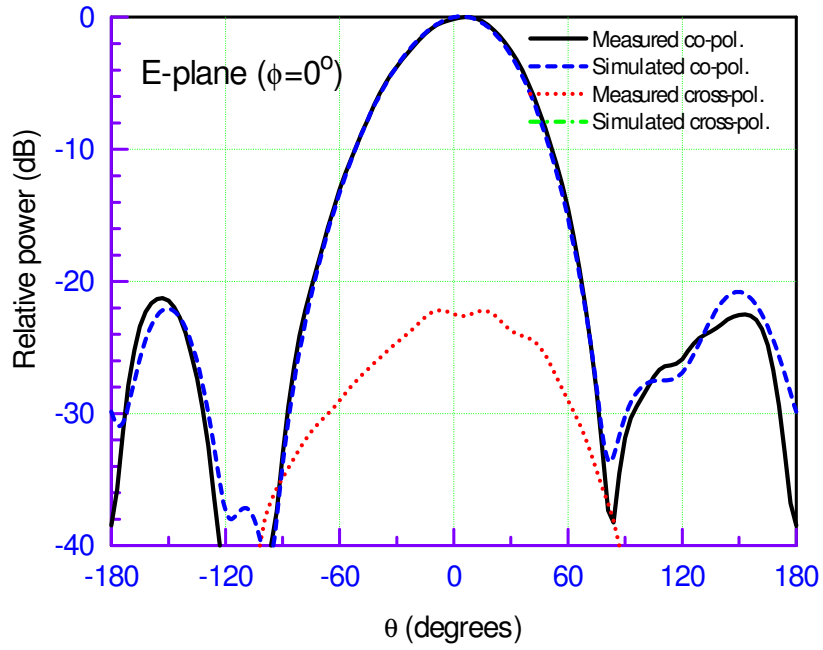
(a)
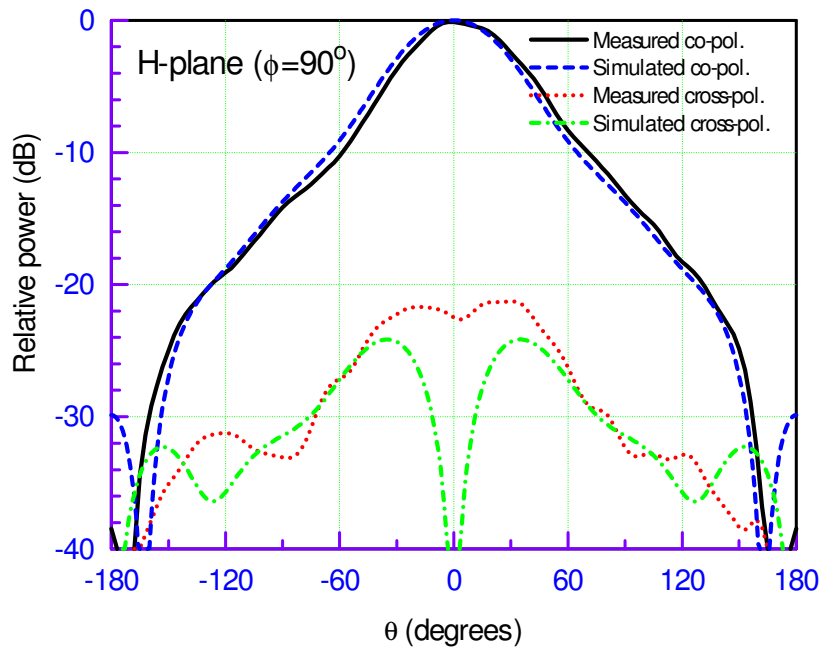
(b)

Figure 2.12 Normalized radiation pattern at 5.5 GHz (a) E-plane φ = 0° (b) H-plane φ = 90°

2.3. Conclusion

A triple-band compact unidirectional antenna is realized in this chapter. It achieves directionality by adding high-frequency wire-resonance paths symmetrically. The size reduction is achieved by top-loading the low frequency resonance path of the antenna symmetrically. This chapter shows that symmetry can be applied to achieve consistent directionality across different frequencies to overcome the pattern distortion experienced by the higher frequency elements.

Areas for future research would be to improve the lower frequency bandwidth by adding coupling elements to the low frequency structure. Alternative applications such as multiband phased arrays or a multi-port antenna can be investigated. The current design is not sufficient for a phased array because the 3 dB beamwidth of the antennas at high frequencies are narrower. Thus the scan angle for the array will be more limited at higher frequencies. A multi-port antenna system can be an alternative to a single-port, multi-band antenna. A multi-port system increases the performance of an overall design by allowing the antenna to be fed by an optimized transceiver for each frequency band.

Chapter 3

MULTI-FREQUENCY ANTENNAS FOR BASE STATAION

3.1.   Introduction: Cognitive Radio Base Station

With the increasing demand for wireless connectivity, the radio frequency spectrum is getting more and more crowded with applications satisfying communication needs for public, private, and government sectors. Spectrum congestion increases the cost of spectrum licensing, which ultimately leads to a higher cost per bit for each user. Cognitive radio aims to reduce spectrum congestion by sensing unused bandwidth in the existing communication standards and opportunistically maximizes the spectrum utilization for the end user [34]. In the public communication sector, several bands are allocated to existing standards, such as GSM, PCS, WCDMA, WiFi, and the recently adopted WiMax worldwide. It is advantageous to provide cognitive radio services that maximize the data delivery across those existing communication standards utilizing a single base station antenna system.

To support the comprehensive and intelligent communication offered by the cognitive radio architecture, a new paradigm of RF front end is needed [35]. Due to wide spectral bandwidth utilization, reducing interference between radios is critical for improving their signal-to-noise ratio and the overall spectrum usage. Thus, RF front ends need to limit their instantaneous dynamic range to avoid non-linear distortion in the desired channel [36]. Several authors have proposed antenna structures that would reduce antennas' dynamic range by the use of switches [37]-[44]. Switchable antennas can be realized using electronic switches, such as varactor diodes or MEMS switches. Three

types of switchable/reconfigurable antennas have been implemented in the literature: polarization [37]-[38], spectral [38]-[42], and spatial [41]-[44]. For base station antennas, spatial and spectral sensing are the two areas of interest.

In traditional base stations, several antenna techniques have been developed to enhance system capacity. 1) The antenna is positioned with its E-plane perpendicular to the earth surface to utilize ground reflections for increasing signal range. 2) To eliminate co-channel interference between adjacent towers and increase spectrum reuse, spatial sectoring is implemented in the antenna's H-plane. The horizontal beamwidth typically varies among 60°, 90°, 120°, 180°, and 360°, depending on the number of sectors deployed [45]. 3) To further reduce the co-channel interference between adjacent towers and enhance signal strength toward the mobile device, a narrow vertical beamwidth ranging from 7° to 20° with beam tilting is desired. Thus, an antenna array needs to be extended vertically along its E-plane. Such an array implementation is difficult to achieve in frequency-agile antenna designs since the electrical element spacing for each frequency band must be almost the same in wavelengths to avoid grating lobes. Grating lobe and side lobe formation results in large signal variation in the service area and should be reduced unless the system can spatially reconfigure the null position to its advantage. Due to grating lobe considerations, most existing directional multi-band antennas cannot be easily extended to array configurations along their E-plane, because these antennas share the same radiating element at different frequency bands [38],[42], [46]-[48]. A switchable multi-band two-radiator element and its expanded array are introduced to offer a sectored radiation pattern in four frequency bands: 800-900 MHz

20

(B1), 1.7-2.5 GHz (B2), 3.3-3.6 GHz (B3), and 5.1-5.9 GHz (B4), used for GSM, PCS, WCDMA, WiFi, and WiMAX systems.

3.2.   Switchable Quad-Band Antenna Array for Base Station

In this section, a switchable multi-band two-radiator element is introduced and optimized to offer a sectored radiation pattern in four frequency bands: 800-900 MHz (B1), 1.7-2.5 GHz (B2), 3.3-3.6 GHz (B3), and 5.1-5.9 GHz (B4), used for GSM, PCS, WCDMA, WiFi, and WiMAX systems. This quad-band two radiator architecture can be arrayed because the radiating elements for each frequency band can be readjusted along their E-plane. A two-element array will be presented to demonstrate the possibility of beamwidth narrowing and beam tilting along the E-plane, as desired by base stations. Furthermore, this quad-band antenna geometry has a compact form factor and high scalability to incorporate additional frequency bands in the future. Design and measurement results for the quad-band antenna element are first introduced, followed by a description of the system-level requirement and the design process of the quad-band array.

3.2.1. Quad-Band Element

The configuration of the proposed switchable quad-band antenna element is shown in Figure 3.1. For B1, B2, and B3, there is a pair of symmetrically positioned dipole arms in the y direction. The separation between the dipole arms is approximately 0.5λ with λ being the free-space wavelength at the center frequency for each frequency band. Only a single dipole is used for B4 because it is located exactly in the center of symmetry. The dipole arm selected was based on "the printed broadband dipole antenna with integrated balun" documented in [62]-[66]. It provides a simple broadband dipole structure with the capability to easily tune the impedance matching. With this structure, the radiation

21

pattern of the quad-band antenna can be easily controlled by the relative position of the dipole arms and the dipole length, while the impedance matching is individually controlled by the balun matching network.
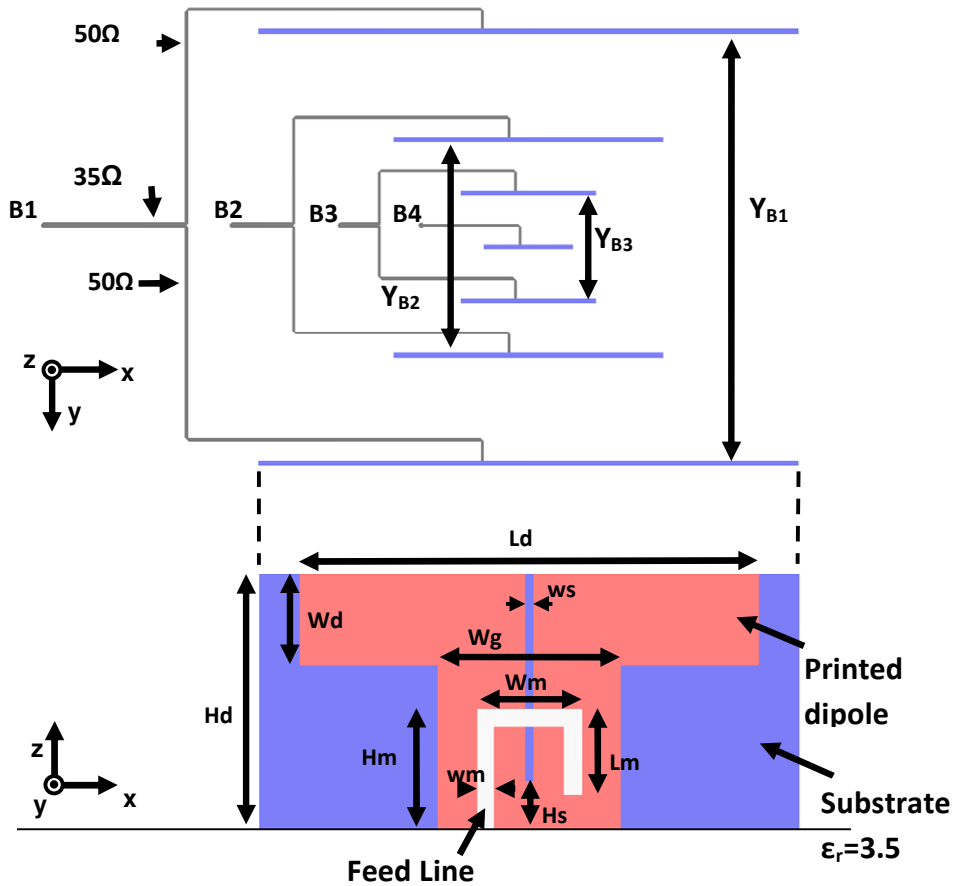
Figure 3.1 Configuration of a quad-band antenna element

The quad-band antenna has four ports, as indicated in Figure 3.1, and is designed to be controlled by a TeraVicta SP4T MEMS switch. A schematic of the MEMS switch system is shown in Figure 3.2, which includes a front-end amplifier (RFA), a digital controller, and a SP4T MEMS switch. The MEMS switch implementation is an active area of research because it offers the low loss, high isolation, and high linearity desired by the in RF front end [67]. In this chapter, the switch performance will not be covered and an ideal switch is assumed to be connected to the ports of the quad-band antenna

22
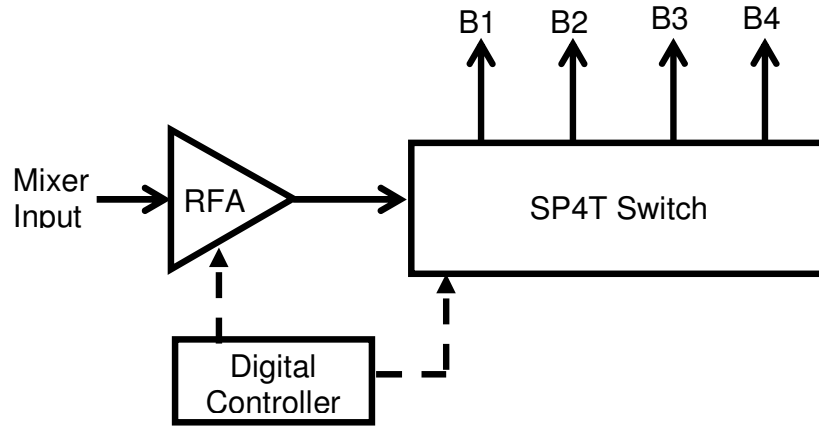
element.

Figure 3.2. A schematic of a switch system for the quad-band antenna element

The antenna is designed using Microstripes 7.5, a TLM based commercial solver, with a Taconic RF35 substrate having ε_r=3.5 and loss tangent=0.0018. The dipole arms are designed on a 30 mil (0.762 mm) substrate to provide better mechanical stability for standing perpendicular to the ground, while the base board is designed on a 20 mil (0.508 mm) substrate to allow narrower feeding lines on board. A feed network is designed for each frequency band, and 35 Ω quarter wavelength transformers are used to split the input power into two 50 Ω antenna loads. To mimic the behavior of the MEMS switch, non-active ports are left as open circuits in both simulations and measurements. A prototype of the quad-band antenna element is pictured in Figure 3.3. A 400 mm $\times$ 400 mm ground plane was used to support the quad-band antenna. The optimized dipole arm dimensions and dipole spacing are listed in Table 3.1. The optimization is done in a three stage process: (1) radiation pattern and matching of individual dipole arms are simulated in the four frequencies of interest, (2) the H-plane radiation pattern is optimized by adjusting the relative spacing of the dipoles, and (3) the balun transition of each dipole

23

arm is readjusted to tune the impedance after including the effects of radiator spacing and

feeding network.
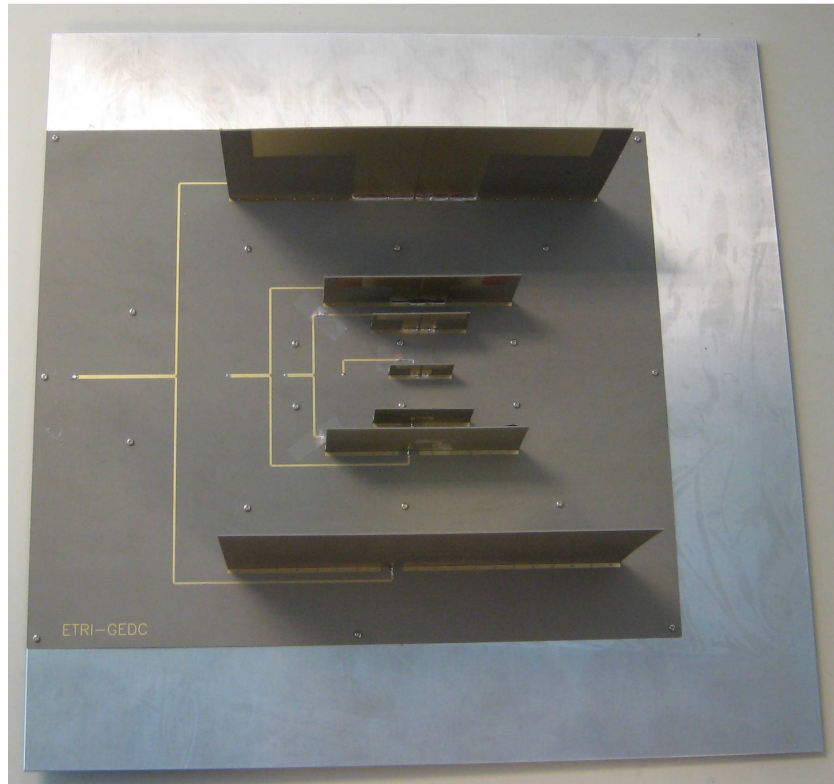
Figure 3.3. A prototype of the quad-band antenna element.

Table 3.1
Dimensions of the Quad-Band Antenna Element (mm)

	B1	B2	B3	B4
Hd	95	40	25.2	15
Ld	170	76	45.6	27
wd	34	15	9	5.5
wg	68	30	18	11
ws	1	1	1	1
Hs	0	0	0	0
Hm	39.7	19.7	9.7	5.5
wm	1.7	1.7	1.7	1.7
Wm	36	16	11.6	8
Lm	26.7	10.7	3.7	4.5
Y	200	80	50	0

To design the individual dipole arm, *Ld* of 0.5 λ is chosen for the printed dipole

24

length elevated 0.25 λ above the ground plane (*Hd*). The dipole width *Wd*, which is half of *Wg* for impedance matching, needs to be at least three times greater than *wm*, the feed line width. This allows a microstrip mode along the feed line and maintains a constant impedance between the ground to the radiating dipole ends. By selecting *Hs*=0, and mainly adjusting *Hm* and *Lm*, a wideband impedance match is obtained for a single-frequency band. Alternatively, the dimensions in [62], optimized for B2 operation, can be resized for the other three bands.

The goal of radiation optimization is to reduce drastic variations of the H-plane pattern within the 10dB beamwidth by changing the radiator spacing, *Y*. The sidelobe level at the higher-frequency H-plane and grating-lobe formation at the lower-frequency H-plane are the radiation performance trade-offs when adjusting this parameter. High-frequency sidelobes are caused by excessively decreasing the spacing between the adjacent lower-frequency elements, thus increasing the coupling between the dipoles and exciting more higher-order modes. To illustrate this effect, Figure 3.4(a) shows the increasing sidelobe level and null formation at B4 due to the decreasing spacing of Y_{B3}. By increasing the adjacent dipole spacing, the sidelobes can be reduced, but grating lobes may emerge for these adjacent dipoles if the H-plane spacing between the same frequency radiators well exceeds 0.5λ [68]. The grating lobe formation in Figure 3.4(b) shows an increasing grating lobe level in B2 as its dipole spacing, Y_{B2}, increases. Based on these analyses, a sidelobe level of less than 10 dB and a radiation ripple of less than 4 dB is obtained for all four frequency bands.
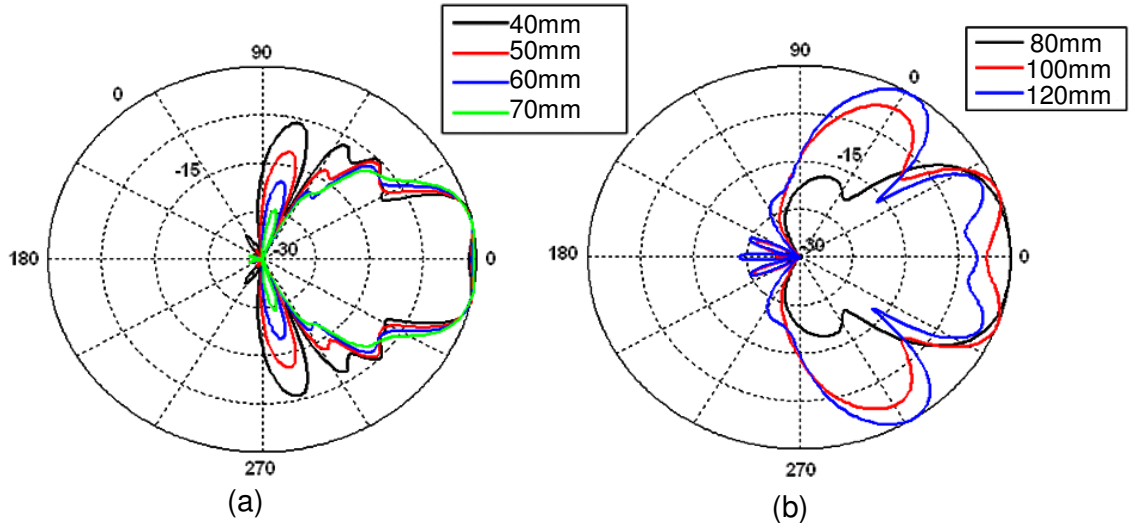
Figure 3.4. H-plane Radiation affected by (a) adjacent lower frequency dipoles, effect of YB3 on B4 at 5.5 GHz, (b) grating lobe, effect of YB2 on B2 at 2.4GHz.

After the optimized radiator spacing is obtained and the feeding network is included in the base board, the integrated balun dimensions are readjusted to accommodate the mutual coupling and power divider effects on the initial dipole impedance. *Hm*, *Hs*, and *Lm* are the three most significant dimensions when tuning the impedance bandwidth. In the equivalent circuit of the balun transition [62], *Hm-Hs* determines the shorted slot stub length, *Hd-Hm* determines the slot length, and *Lm* determines the microstrip stub length.

The measured and simulated results for return loss are shown in Figure 3.5 and Figure 3.6, featuring a value better than 10 dB in the frequency bands of interest. Passive antenna gains are measured at the SATIMO facility and plotted in Figure 3.5 and Figure 3.6. A value of ~7-9 dBi is observed at the center frequency for each frequency band. There is a maximum of 2 dB variation across a wide bandwidth. The measured radiation patterns are fairly constant across each frequency band, as shown in Figure 3.7. Less than 20 dB cross-polarization is achieved across all frequency bands to ensure the radiation

26

linearity needed for the base station. The simulated pattern matches that of the measurement. Due to the finite ground plane, significant back radiation is observed for the pattern of 850 MHz. The ripples appearing at the radiation pattern for the highest frequency band (i.e., B4) are due to the higher-order modes excited on the lower band dipoles.
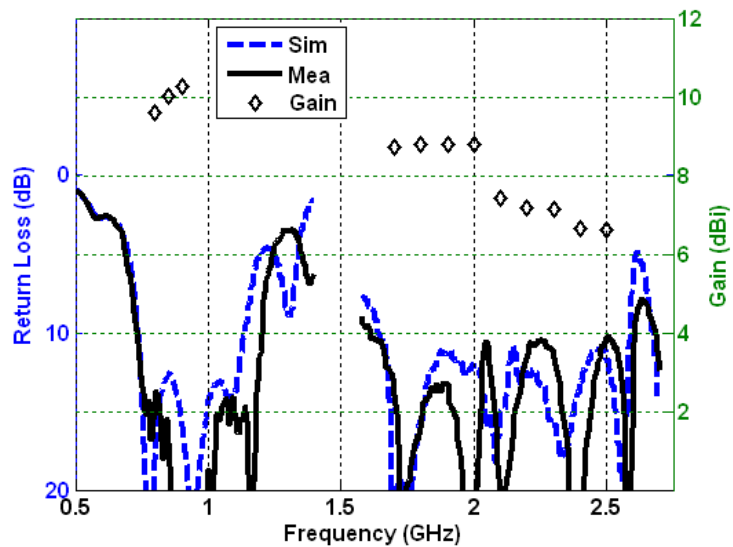
Figure 3.5. Simulated and measured return loss with measured gain of the quad-band antenna element in B1 and B2.
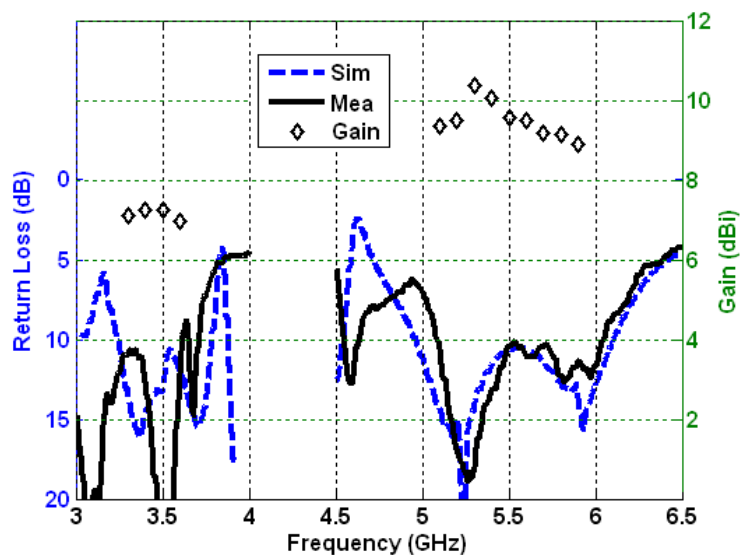
Figure 3.6. Simulated and measured return loss with measured gain of the quad-band antenna element in B3 and B4.

27
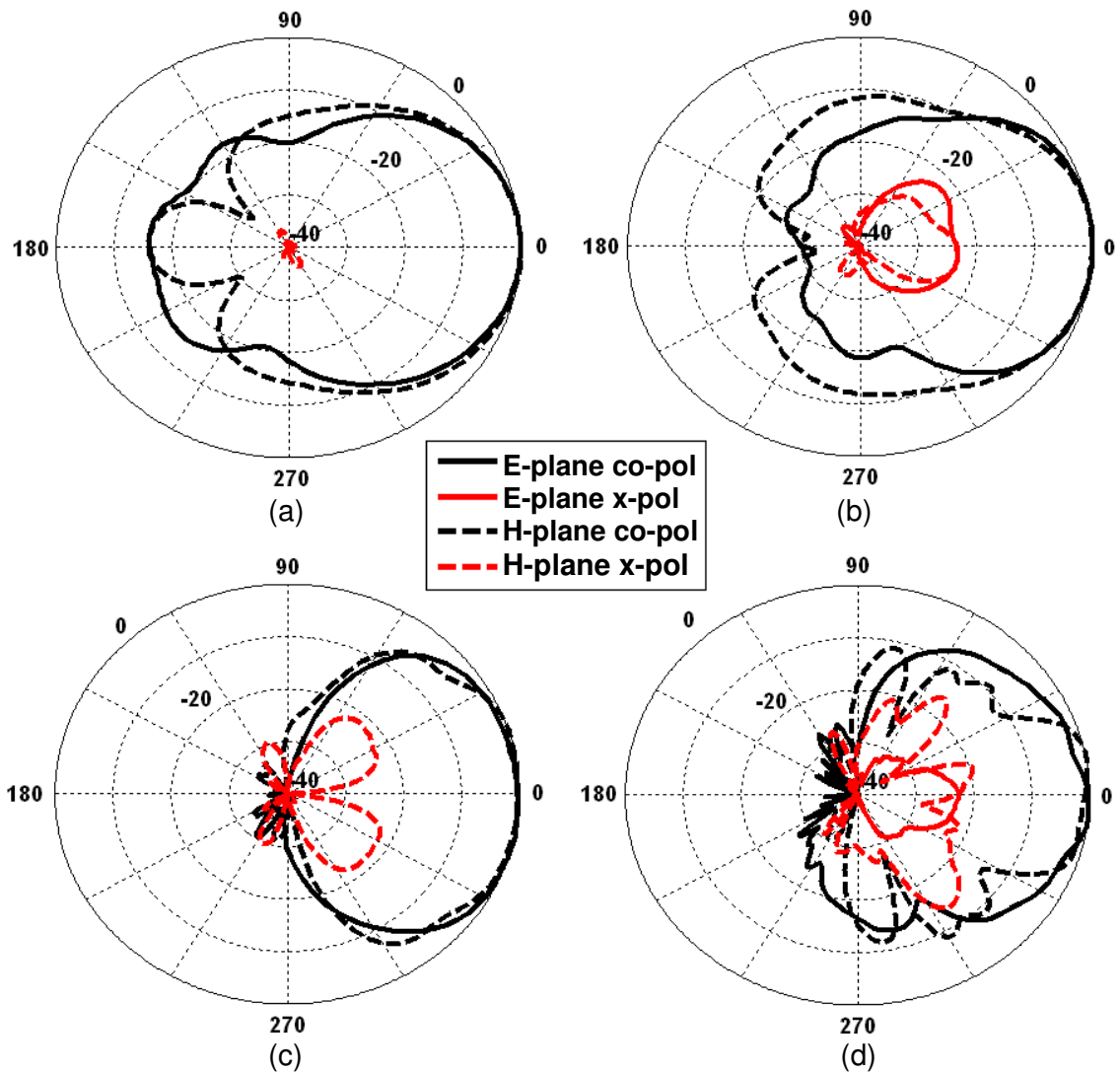
Figure 3.7. Measured E-plane (x-cut) and H-plane (y-cut) patterns (a) 850MHz (b) 2GHz, (c) 3.5GHz, (d) 5.5GHz of the RAE.

Although the two-radiator element is designed for switched frequency operations, investigation of its simultaneous frequency operation without the presence of the switch gives further insight into the element's performance. The isolation between the ports is critical in this case since one pair of radiators may increase the noise level received by other pairs due to higher-order resonance and coupling. The minimum insertion loss, characterizing the worst-case isolation, is summarized in Table 3.2 for each band of

28

interest. Poor isolation from B1 to B2, B3 to B2, B3 to B4, and from B4 to B2 indicates the need to isolate components such as switches or filters to reduce the noise formation.

Table 3.2
Measured Worse Case Insertion Loss Between Two-radiator elements

	B1 freq	B2 freq	B3 freq	B4 freq
B1 input	NA	24 dB	38 dB	31 dB
B2 input	33 dB	NA	34 dB	28 dB
B3 input	62 dB	17 dB	NA	15 dB
B4 input	48 dB	25 dB	36 dB	NA

3.2.2. Quad-Band Two-Element E-Plane Array

To demonstrate the capability of the quad-band two-radiator element to extend to an array, a two-element array aligned in the x direction is presented in Figure 3.8. For each frequency band, there are 2 x 2 dipoles; one dipole from each band is grouped in a quadrant to be fed by a switchable amplifier similar to an active integrated antenna toplogy. The novelty of the quad-band antenna array lies in the use of additional symmetry enforcement in the x direction to achieve good uniformity of radiation pattern along its E-plane. The array is not the conventional array implementation such as the one shown in Figure 3.9. If the original quad-band antenna element is replicated and placed 0.5λ (B1) from another element in the x direction, as in Figure 3.9, strong grating lobes will emerge at the higher frequency bands because the array separation at B1 is much larger than the free space wavelength of B3 and B4. The topology of Figure **3**.8 provides locality in the system-level implementation while satisfying the array spacing requirement. It can be further extended to n elements along the E-plane by symmetrically containing a pair of higher-frequency elements between the lower ones. Unlike the quad-band element, no power splitter network was designed for the array due to the crowded

base board spacing. For simplicity and without loss of generality, the design of the switchable amplifier will not be covered.
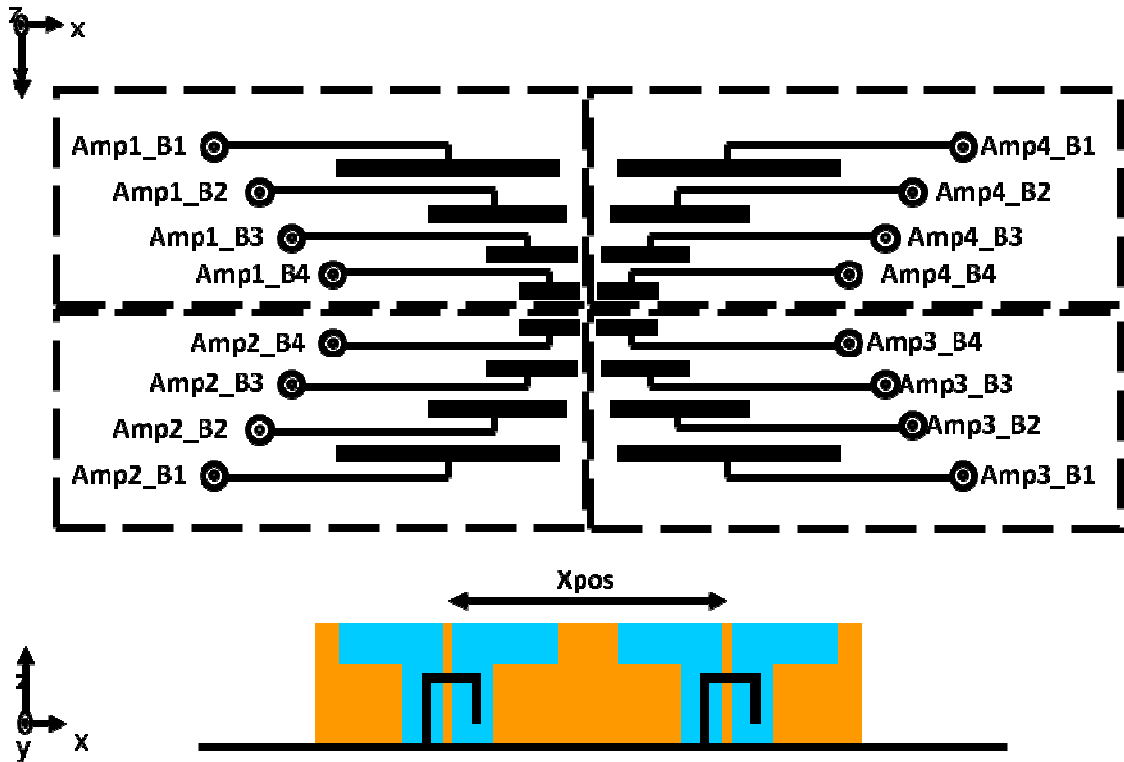
Figure 3.**8. Configuration of a quad-band antenna array.**
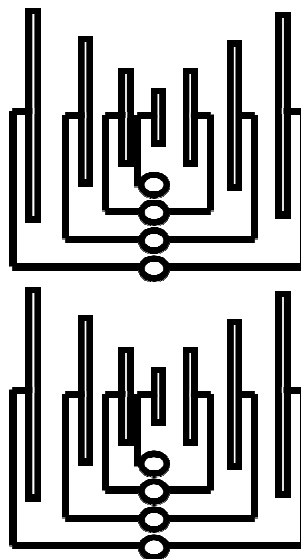
Figure 3.9. An array of quad-band anteanna element that would form grating lobes.

The quad-band antenna array is also built on the RF35 substrate. The dimensions of the quad-band antenna array are listed in Table 3.3
Dimensions of the Quad-band Antenna Array (mm)

	B1	B2	B3	B4
Hd	95	40	25.2	15
Ld	170	76	45.6	27
wd	34	15	9	5.5
wg	68	30	18	11
ws	1	1	1	1
Hs	0	0	0	0
Hm	39.7	17.7	9.7	5.7
wm	1.7	1.7	1.7	1.7
Wm	36	16	11.6	8
Lm	26.7	16.7	5.2	5.5
X	200	80	60	35
Y	200	80	50	24

. A prototype of the quad-band antenna array with a 600 mm × 400 mm ground plane

is displayed in Figure 3.10.

Table 3.3
Dimensions of the Quad-band Antenna Array (mm)

	B1	B2	B3	B4
Hd	95	40	25.2	15
Ld	170	76	45.6	27
wd	34	15	9	5.5
wg	68	30	18	11
ws	1	1	1	1
Hs	0	0	0	0
Hm	39.7	17.7	9.7	5.7
wm	1.7	1.7	1.7	1.7
Wm	36	16	11.6	8
Lm	26.7	16.7	5.2	5.5
X	200	80	60	35
Y	200	80	50	24
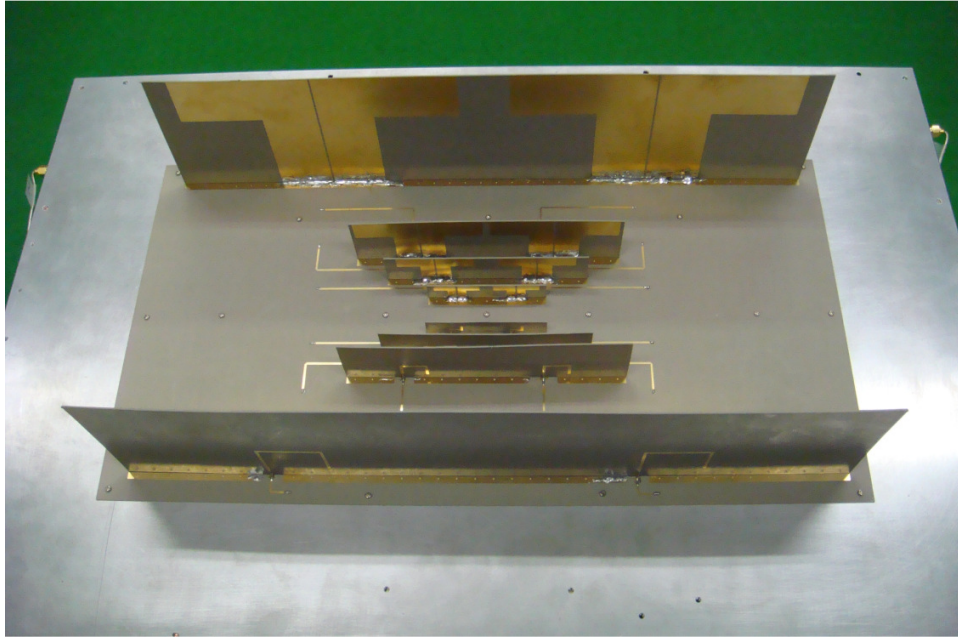
Figure 3.10. A prototype of the quad-band antenna array.

To characterize the impedance matching, the active driving impedance is measured to account for the mutual coupling between the four driven ports. In broadside operation where all ports are fed in-phase, the simulated and measured active driving impedance in Figure 3.11 and Figure 3.12 achieves 10 dB across the four frequency bands of interest. A Narda 4436-4 power divider is used to create in-phase feeding for the passive radiation pattern measurement in at SATIMO. From the radiation patterns shown in Figure 3.13, a more directive pattern is obtained in the E-plane compared to Figure 3.7, with no significant grating lobe formation. High linearity is achieved by having less than -20dB of cross polarization. The antenna gains of the array shown in Figure 3.11 and Figure 3.12 are 9-11 dBi, about 2 dB higher than the individual antenna element. Note that the antenna gain is obtained by subtracting the power divider insertion loss.
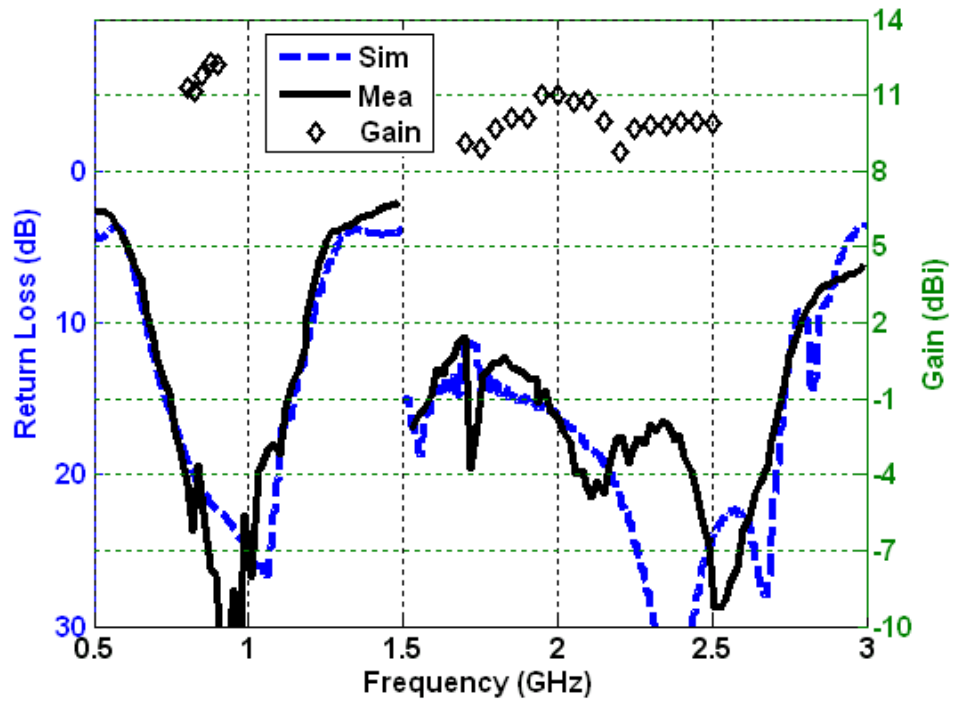
Figure 3.11. Measure and simulated return loss with measured gain (passive) of the quad-band antenan array in B1 and B2.
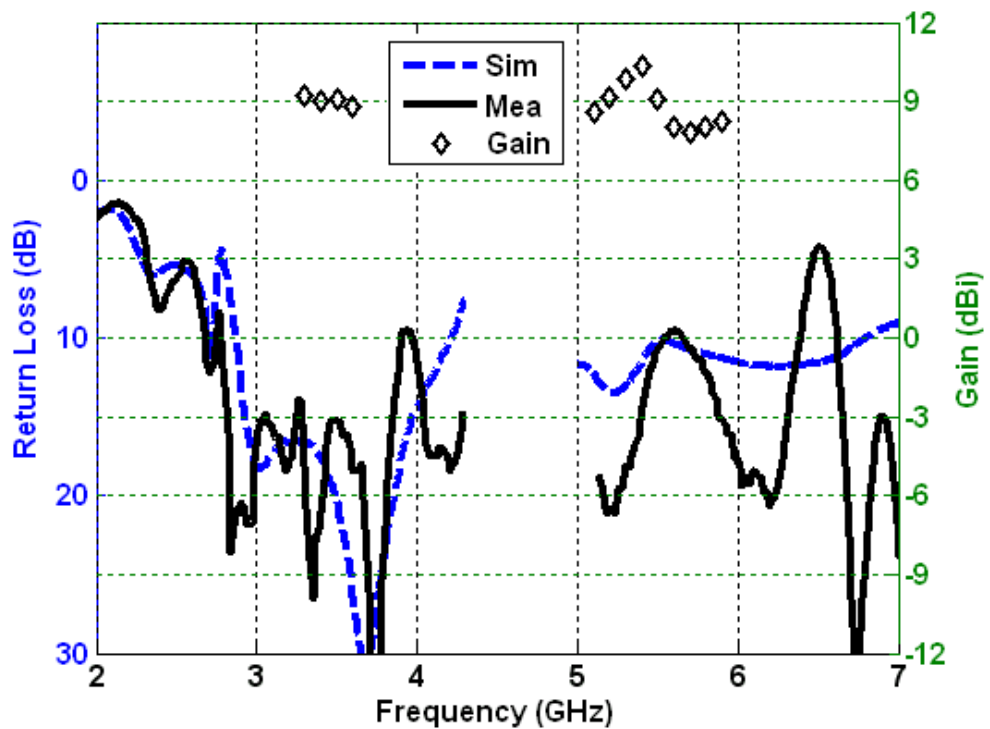
Figure 3.12. Measured and simulated return loss with measured gain (passive) of the quad-band antenna array in B3 and B4.
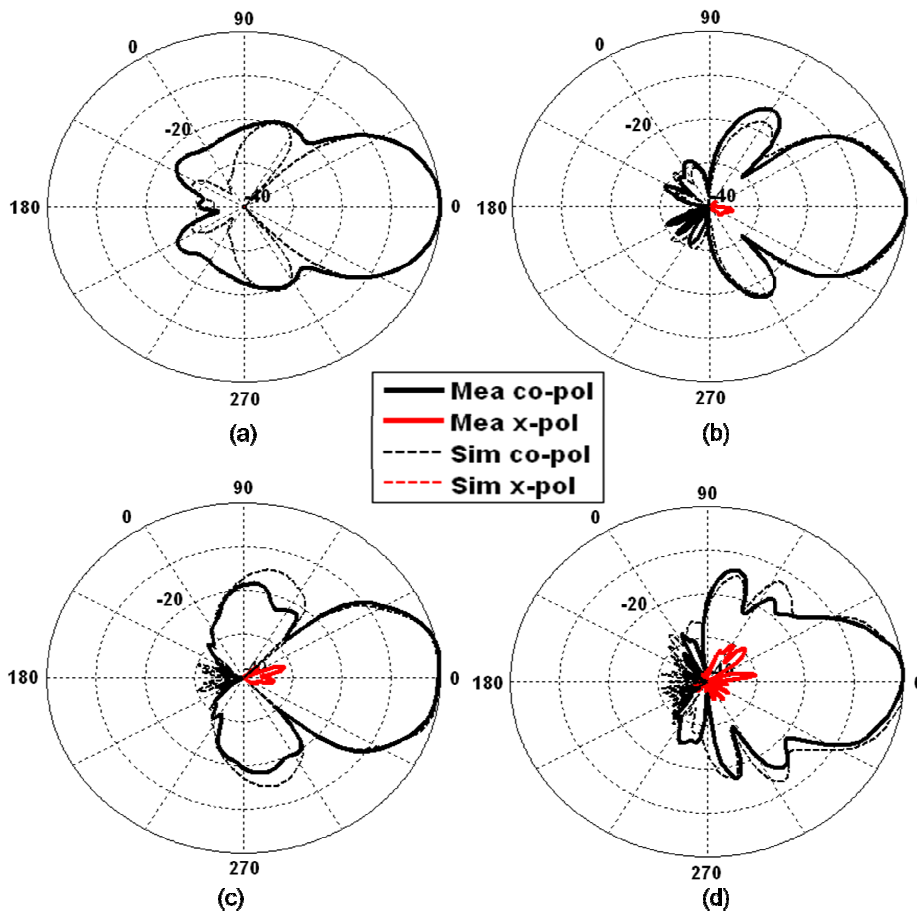
Figure 3.13. Measured and simulated E-plane (x-z plane) radiation patterns of the quad-band antenna array. (a) 1GHz. (b) 2GHz. (c) 3.5GHz. (d) 5.5GHz.

The elements in the quad-band array have a different alignment in the x direction from the original element; thus, the mutual coupling between the radiators is different in the E-plane array configuration and needs to be revisited. In the array case, the highest coupling occurs within elements belonging to the same quadrant. With a minimum insertion loss of 11 dB, the measured worst case isolation summarized in Table 3.4 also indicates the need for isolators.

Table 3.4
Measured Worst Case Insertion Loss Between 4 Elements in the Same Amplifier Quadrant

	B1 freq	B2 freq	B3 freq	B4 freq
B1 input	NA	25 dB	26 dB	37 dB
B2 input	24 dB	NA	19 dB	28 dB
B3 input	45 dB	11 dB	NA	28 dB
B4 input	44 dB	31 dB	12 dB	NA

3.3. Conclusion

Novel configurations of a switchable quad-band two radiator element and its extended array are described. Their operating frequencies cover all spectrums for existing wireless applications, such as GSM, PCS, WCDMA, WiFi, and WiMax. A consistent H-plane pattern suitable for sectoring is achieved by the two radiator element across the four bands. The two element array demonstrates narrowing of E-plane beamwidth for reducing the co-channel interference between adjacent base stations. The quad-band array topology can be further extended along its E-plane to reduce its vertical beamwidth, making the extension of this topology a suitable candidate for cognitive radio base station antenna.

Chapter 4

MULTI-FREQUENCY PAPER-BASED ARRAY (AEROSPACE)

4.1. Introduction: Aerospace Applications

To make aerospace vehicles more aerodynamic and fuel efficient, the antennas on these vehicles need to be thin, compact, lightweight, and high efficiency. For applications that require point to point communications or radar detection, a high-gain antenna with large aperture area is needed. To maximize the limited area on a given vehicle, it is desirable to have phased arrays of different frequencies sharing the same aperture area.

Several authors use wideband or multi-band elements with a single feed to achieve a multi-band array [49]-[51]. However, these antennas often require additional duplexers at the feed to isolate the frequencies. For large arrays, these designs would create additional weight and cost to the system. A multi-band array formed by various single frequency antenna elements is needed to eliminate the duplexer in the system.

A few authors have achieved multi-band arrays by combining different resonance methods into one aperture [52]-[55]. A combination of slot and patch had achieved a 1:2 operating frequency ratio (FR) in [53], while patch elements combined with perforated patch elements have demonstrated 1:3, 1:4, 1:4, and 1:8 frequency ratios in [52], [54], [55] and [54], respectively. In this chapter, a nested dual-band antenna element and its array is presented as a low-cost alternative to support two communication bands on a given aperture. The element was realized on low-cost flexible material [56]-[58] and foam to enable aerodynamic and lightweight integration with space vehicles.

4.2. Inkjet-Printed Dual-Band Nested Element

In this section, a planar dual-band nested element with a 1:2 frequency ratio is introduced on paper substrate. The nested element design was introduced by Ronglin Li in [59]. Similar to the switchable quad-band antenna mentioned in section 3.2, the nested element uses symmetry to maintain the radiation pattern at both frequencies. Unlike the switchable antenna design, this achieves a lower profile design more suitable for aerospace vehicles, and the ability to be arrayed in both directions.

The nested element is shown in Figure 4.1 and Figure 4.2. The antenna is designed using CST Microstripes, a transmission line matrix based solver. Double-sided photographic paper substrate (ε_r=3.1) of 0.52 mm thickness is chosen because of its low-cost and conformal characteristics [56]. With a 39 mm thick foam layer, the elements are elevated above a ground reflector at around $\lambda/8$ of the 1 GHz element and $\lambda/4$ of the 2GHz element. The elements are folded to create a small element size capable of fitting into a 0.5 by 0.5 λ unit cell. To reduce the tilting of radiation pattern for 2 GHz elements, 1 GHz dipole arms surround the high frequency elements symmetrically. The overall dimensions are listed in Table 4.1. The feeding line width is designed as a 50 Ω microstrip line. To maintain the microstrip mode of the feed, the width in the center of each element is kept around 3 times the microstrip line width.
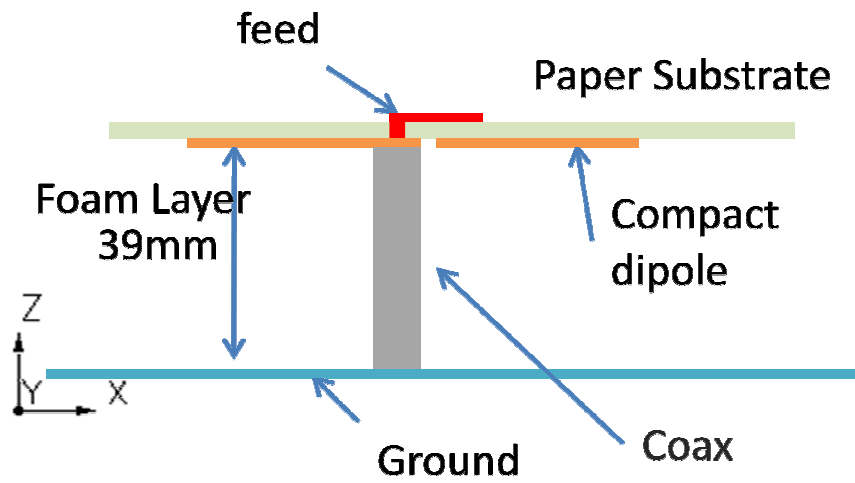
Figure 4.1. Stackup of the Newsted Array.
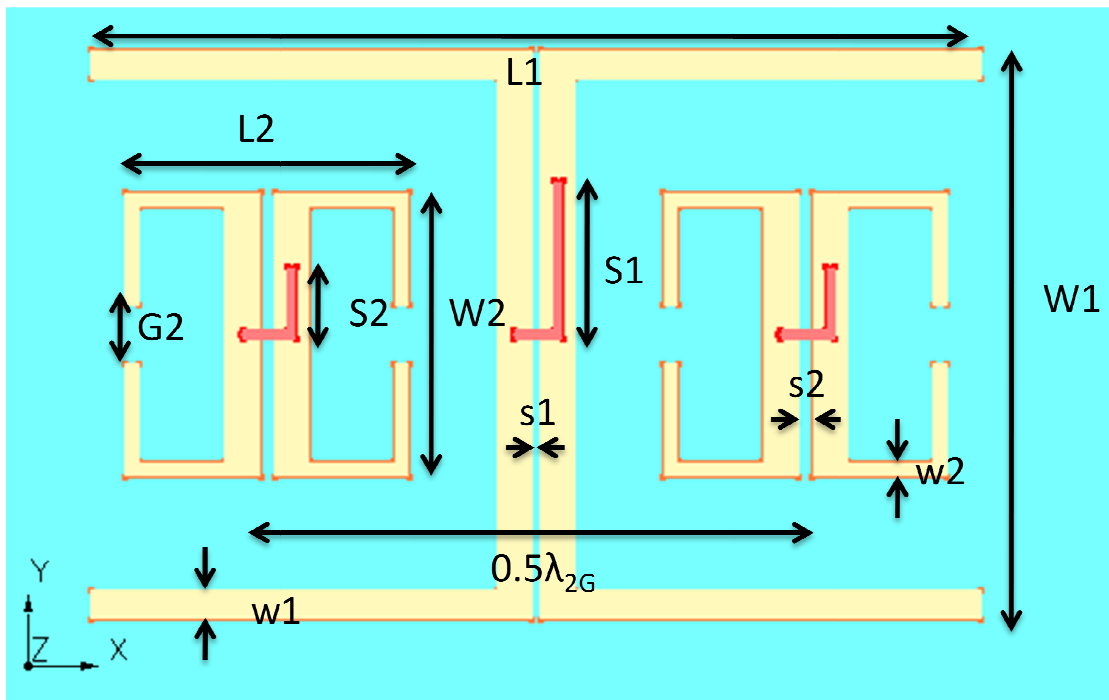
Figure 4.2. Layout of the dual-band nested element

Table 4.1
Dimensions of the Nested Element (mm)

Parameters	1G	2G
L	124	39.5
W	79	39.5
S	22	10
G	NA	8
s	1	2
w	4	2

The antenna is fabricated by inkjet printing with silver ink on both sides of the paper. The fabricated antenna elements are shown in Figure 4.3 with their port definition. The coaxial contacts at the ports are enforced with silver epoxy instead of solder because the soldering temperature will damage the supporting foam as well as the cured ink.
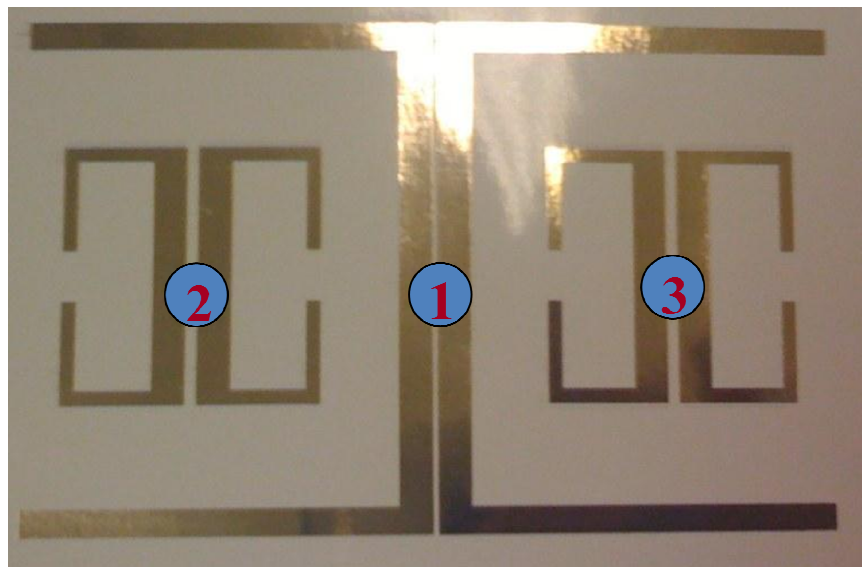
Figure 4.3. Back side of the fabricated antenna with port definition

The measured and simulated S-parameters in Figure 4.4 show good agreement between measurement and simulation. The lower bandwidth at the low-frequency element is caused by the lower antenna profile with respect to wavelength. The coupling between the low and high frequency bands are less than -12 dB at the frequencies of

interest. The radiation pattern of the 1GHz element is shown in Figure 4.5 and Figure 4.6. The measured peak gain is 7 dBi with E-plane beamwidth narrower than the H-plane, as expected of a dipole.
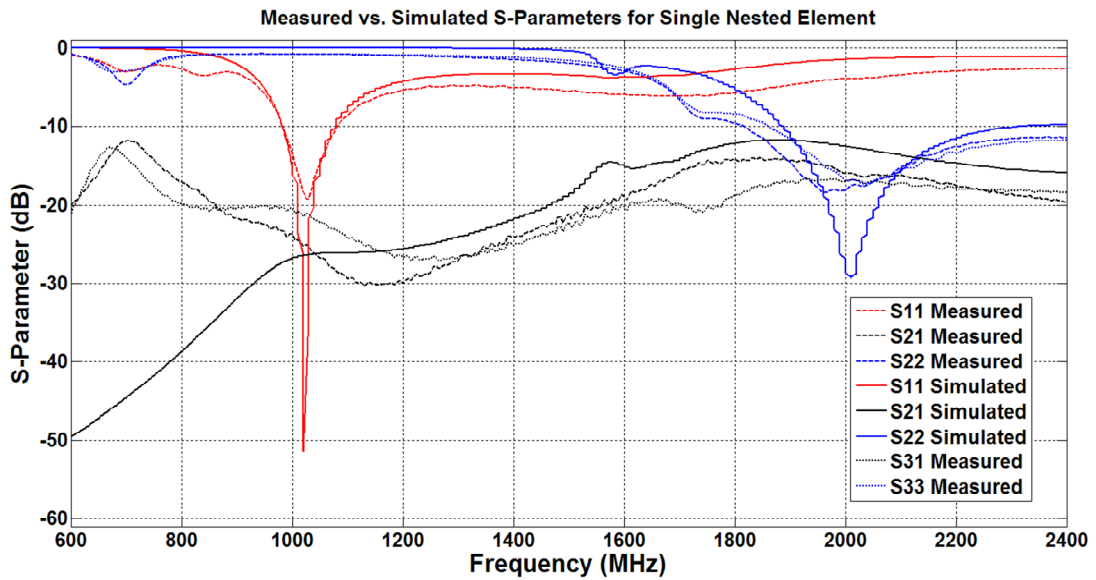
Figure 4.4. Measured and simulated S-parameter for the dual-band elements.
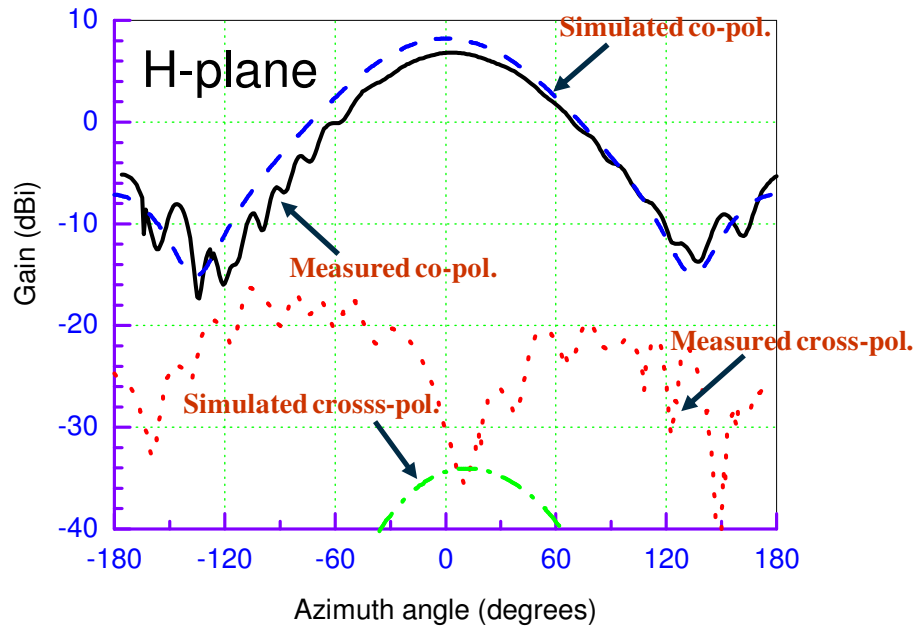
Figure 4.5. Comparison of simulated and measured H-plane patterns at 1 GHz.
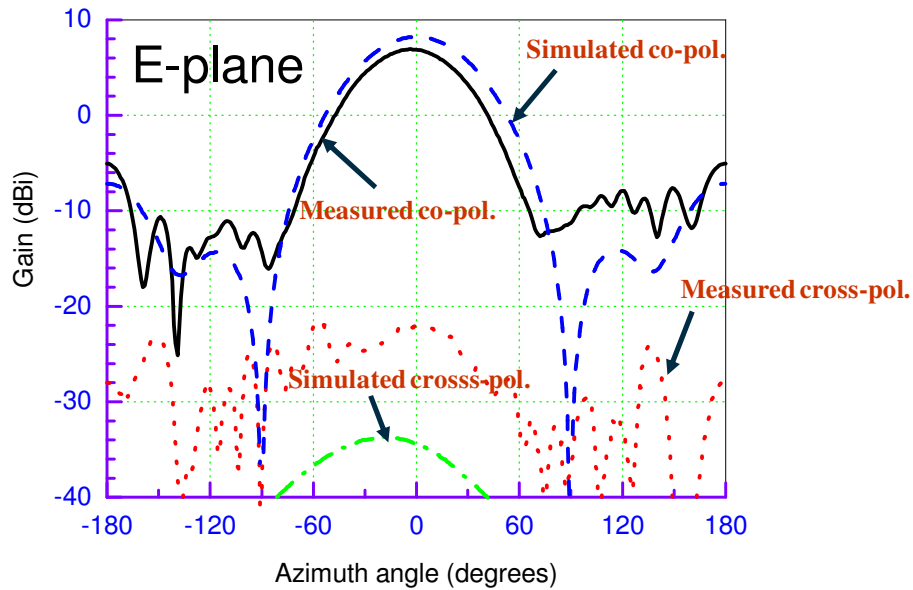
Figure 4.6. Comparison of simulated and measured E-plane patterns at 1 GHz.

For the 2 GHz element excited at port 2, a measured gain of 6 dBi is observed. The symmetric H-plane pattern, shown in Figure 4.7, is due to the equal coupling from two sides of a low-frequency dipole arm. On the other hand, the E-plane pattern in Figure 4.8 is slightly tilted due to the asymmetric coupling to the 1 GHz element in that direction. Element 3 exhibits similar radiation characteristics as element 2, except the beam is tilted towards the positive azimuth angle on the E-plane.

Some of the discrepancies between the simulated and measured pattern are caused by the loss introduced by the silver epoxy and the silver ink. Those losses vary during fabrication and are not accurately modeled in the simulated gain. The agreement in the S-parameter and radiation pattern shows that the loss from the metallization is around 1 to 2 dB.
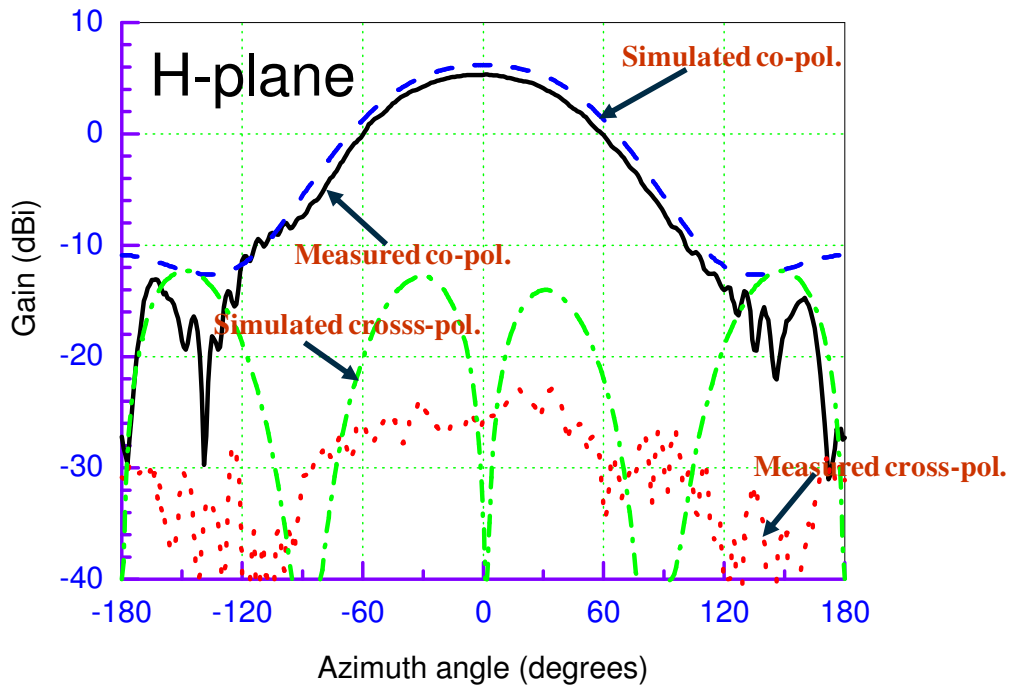
Figure 4.7. Comparison of simulated and measured H-plane patterns at 2 GHz.
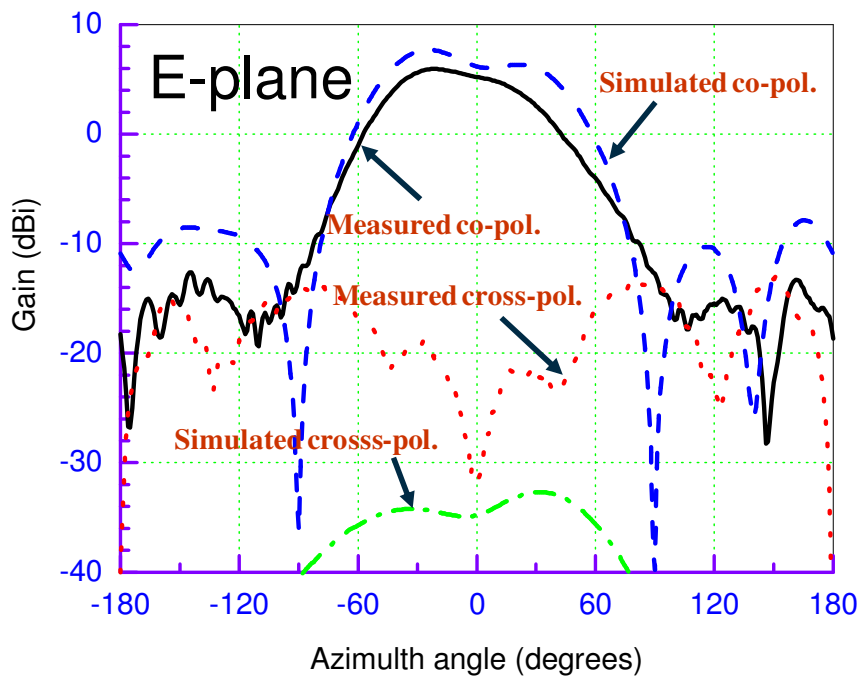
Figure 4.8. Comparison of simulated and measured E-plane patterns at 2 GHz.

4.3. Inkjet-Printed Dual-Band Nested Array

The dual band array is shown in Figure 4.9. The nested element is combined with additional 2 GHz elements to form a unit cell. The array consists of 3×3 1 GHz elements and 6×5 2 GHz elements. Because of the asymmetry of the unit cell, half cells are needed at the edge to keep the overall symmetry of the array.

The 2 GHz elements not surrounded by the 1 GHz element cell are slightly different from the ones nested inside that element. This is because the 2 GHz element inside a nested configuration experiences additional capacitive loading from the surrounding 1 GHz element. The different variables are shorter gap (G= 2 mm) in the dipole ends and shorter stub length (S=6 mm) in the feed termination.
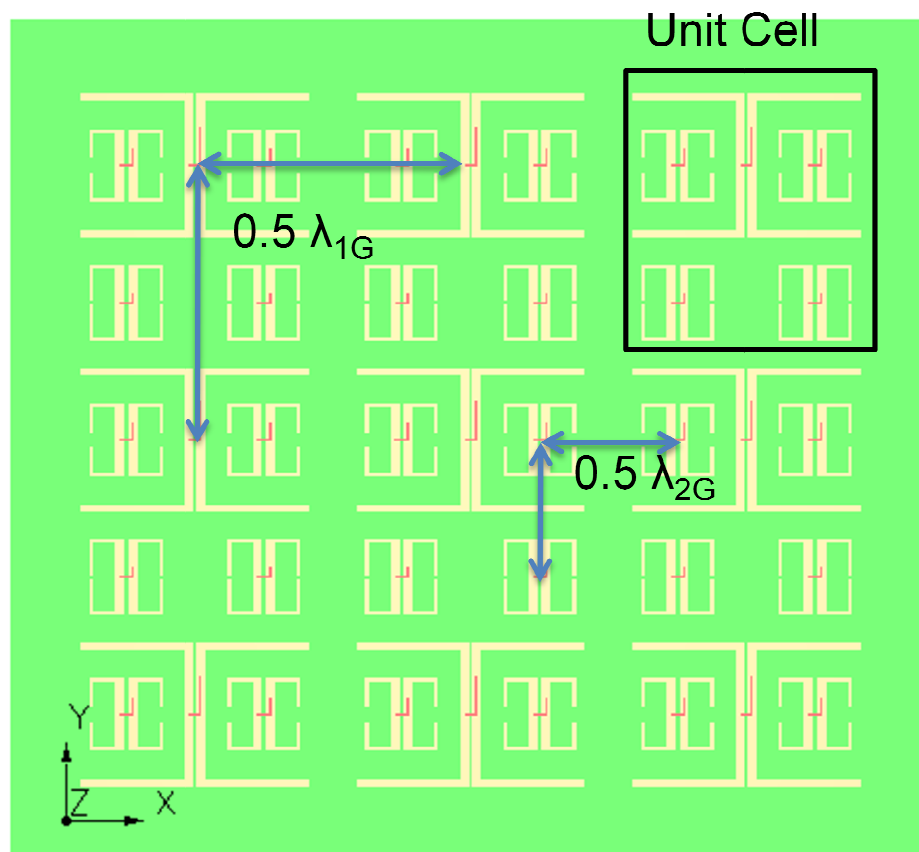
Figure 4.9 Dual-band paper-based array.

The array is fabricated by taping 6 unit cells and 3 half unit cells as shown in Figure 4.10. Each unit cell is made by double-sided inkjet printing on a 15×15 cm photo paper. A 0.085" rigid coax cable is used to feed the antenna at the top through the foam and paper. Because printed silver ink reflows at the required temperature for soldering, silver epoxy is used in order to connect the coax leads to the inkjet patterns. Figure 4.11 shows the side view of the fabricated array and the individual ports feeding into the antenna. In the figure, an additional wooden frame is needed below the array to structurally support its rotation in the anechoic chamber measurement. The presence of the wooden frame has little effect on the performance of the antenna.
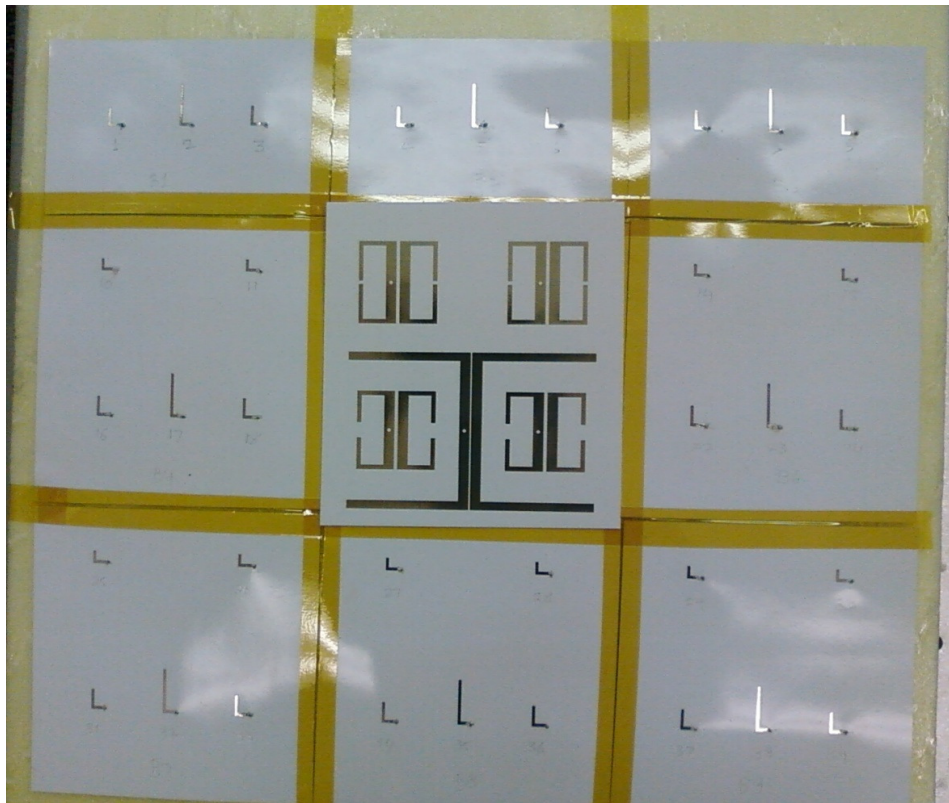
Figure 4.10 Top view of the fabricated dual-band array. It is formed by taping nine antenna unit cells together. The microstrip feed is on the top of the structure. The back of a unit cell is overlaid in the center to show the radiator circuit.

Figure 4.11 Side view of the fabricated dual-band array showing the foam layer, the SMA ports and the wooden frame.

The array is simulated by CST Microstripes. Figure 4.12 to Figure 4.15 show the return loss comparison of the antenna element at the center and the corner. The measured resonance frequency is close to the simulation. The slight difference is caused by the curing of silver epoxy that added additional resistance (1-5 Ω) to the signal line that was not accounted for in the initial simulation. The added resistance also reduces the measured realized gain of the array from the simulated gain. The broadside gain shown in Figure 4.16 and Figure 4.17 shows that the pattern is similar to simulation but the gain is reduced. 11 dB of gain and 35° 3 dB beamwidth is measured for the 1 GHz array, while 14.5 dB gain and 20 dB beamwidth is measured for the 2 GHz array. The radiation efficiency can be improved once the conductivity between the coaxial feed and the microstrip line increases.
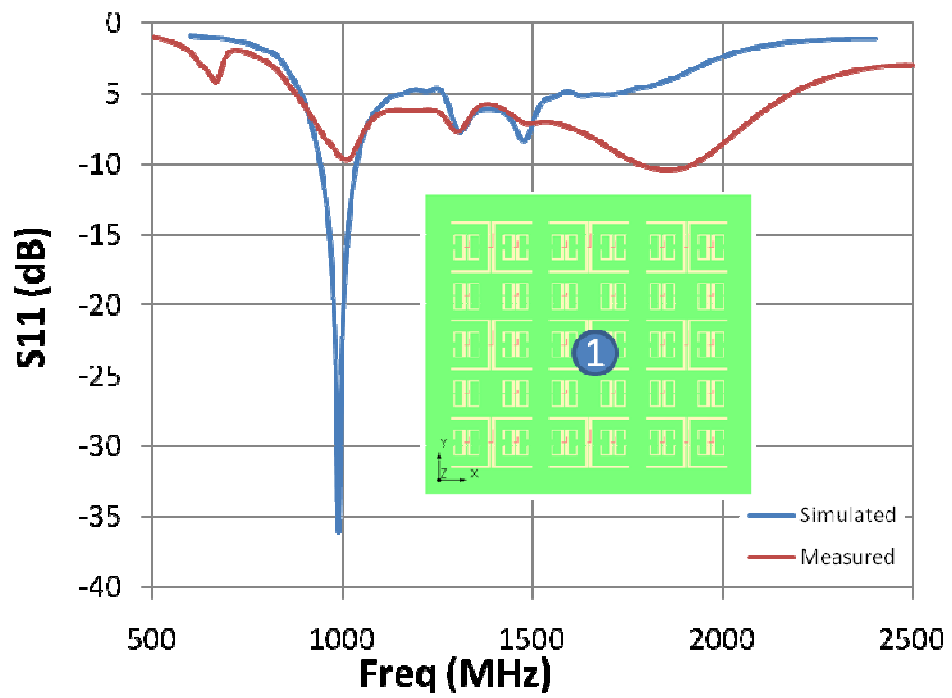
Figure 4.12 Return loss for a 1 GHz center antenna element.
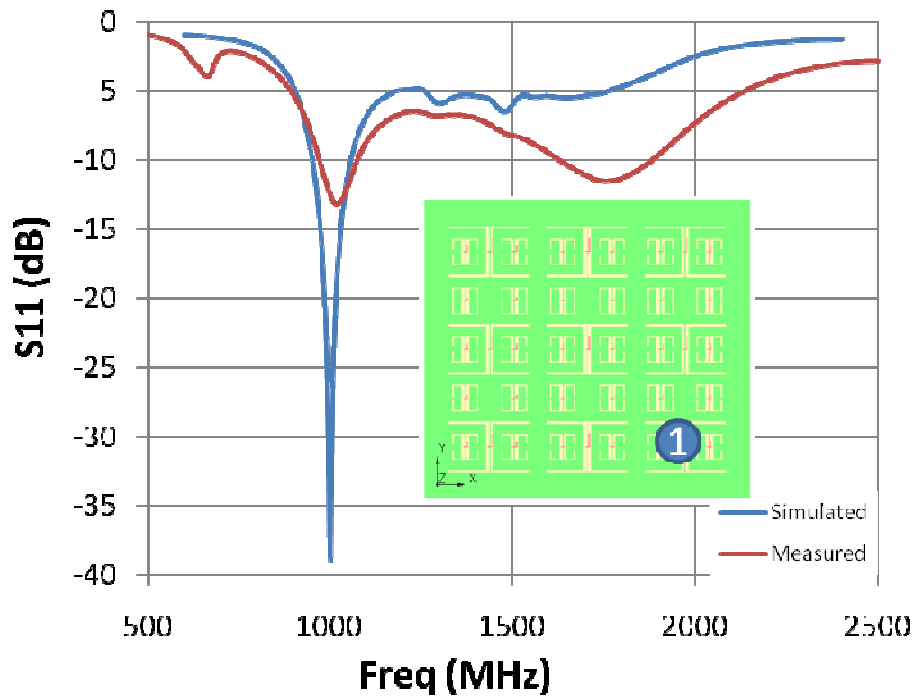
Figure 4.13 Return loss for a 1 GHz edge antenna element.
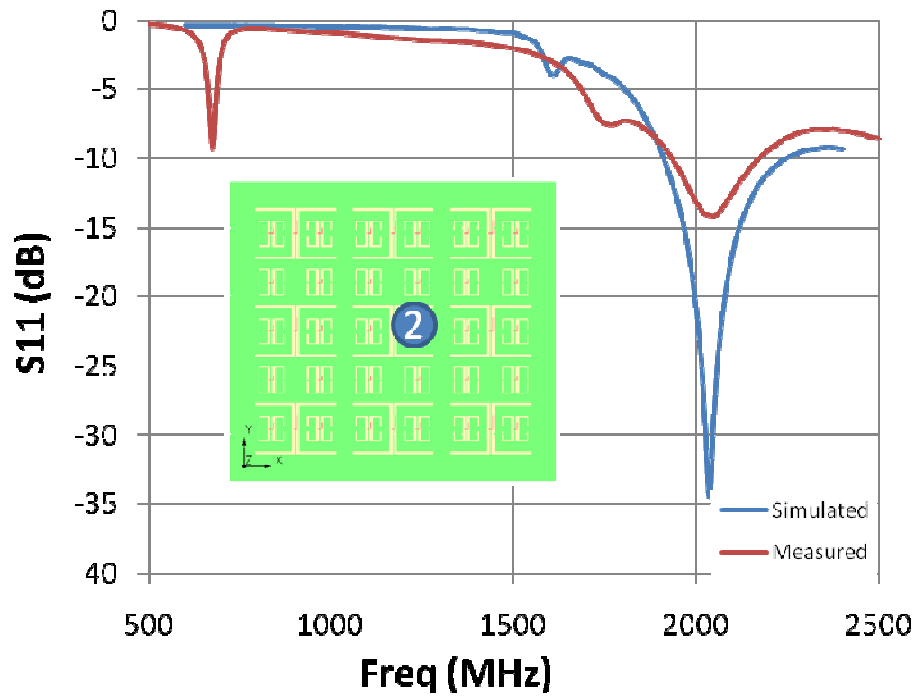
Figure 4.14 Return loss for 2GHz center element
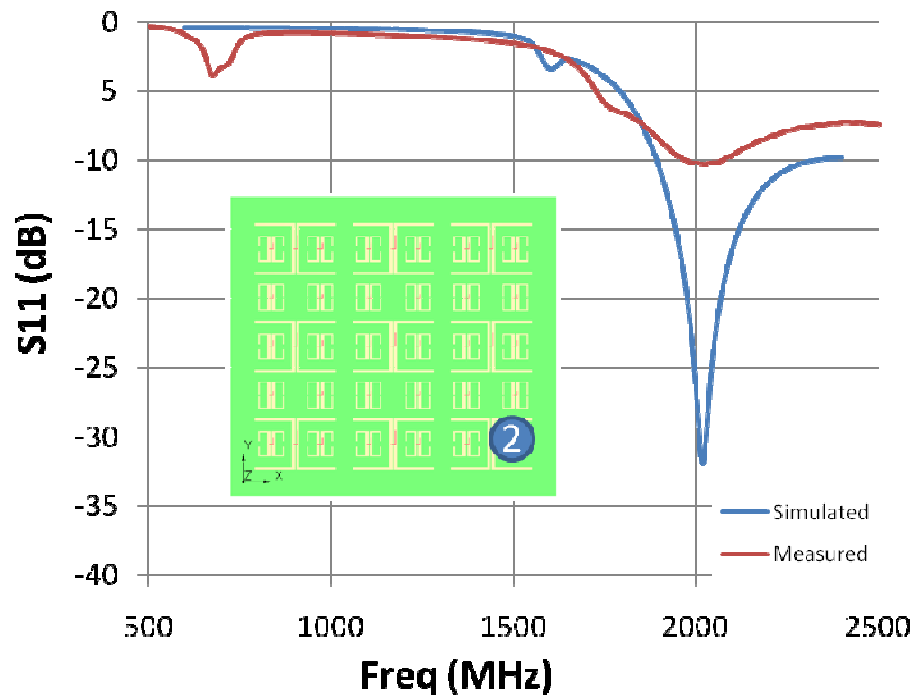
Figure 4.15 Return loss for 2GHz edge element
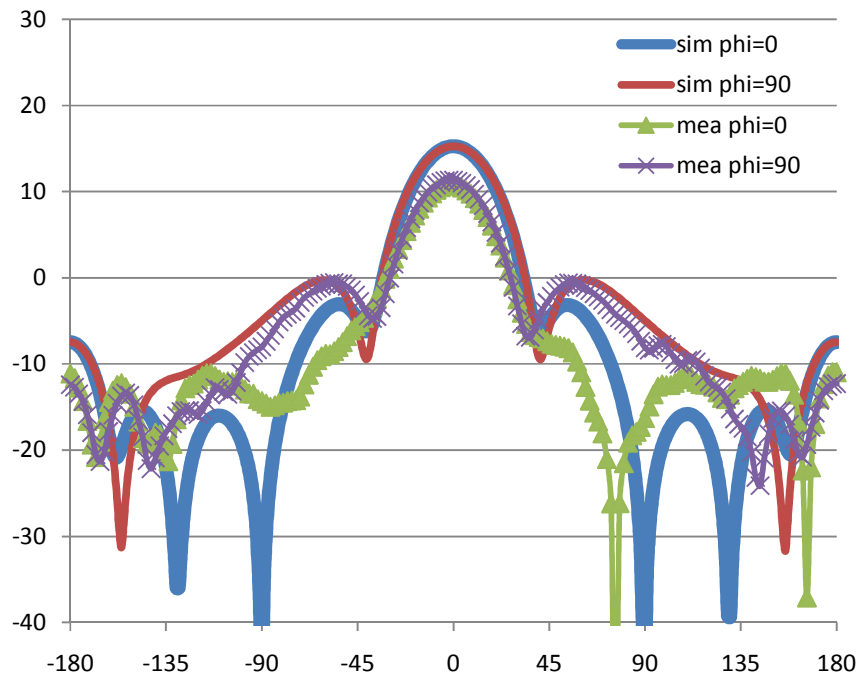
Figure 4.16 Co-pol array pattern at 1 GHz when the ports are fed in-phase (broadside operation).
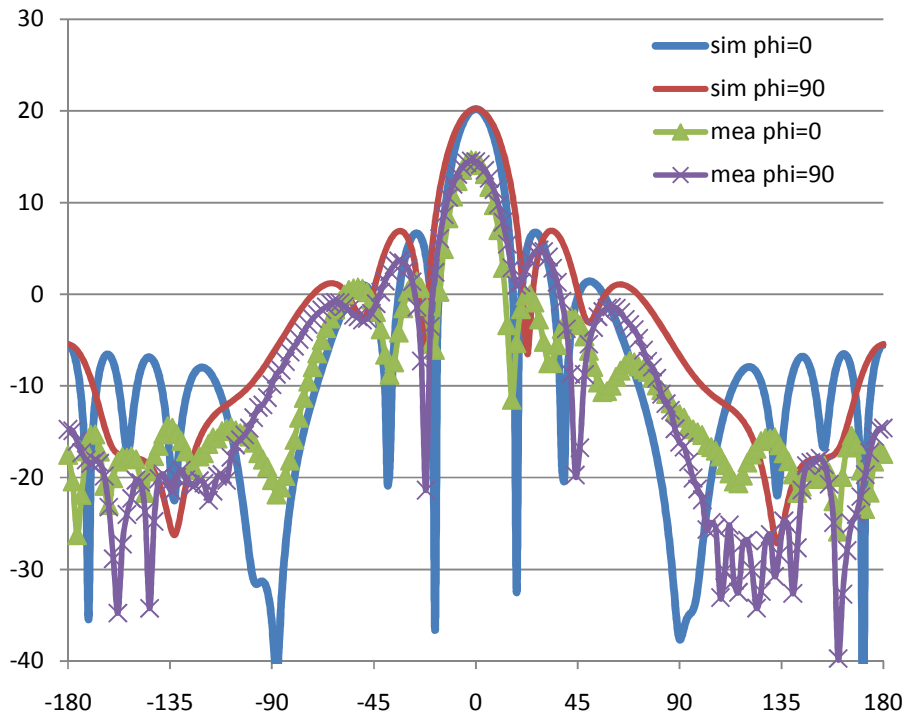
Figure 4.17 Co-pol array pattern at 2 GHz when the ports are fed in-phase (broadside operation).

4.4. Conclusion

A dual frequency paper-based element and its expanded array generates good performance at both operating frequencies. This further demonstrates the capability of inkjet-printing to fabricate large array structures on paper. This offers a new paradigm of realizing large flexible arrays on an eco-friendly, low-cost, lightweight substrate.

This design can be improved in several ways. To improve the efficiency and uniformity of the fabricated array, a more consistent curing technique is needed to reduce the conductor loss of the antenna. Polymer-based substrates, such as LCP and Kapton can be used instead of paper to allow the use of soldering while providing similar flexibility to a paper substrate. The overall thickness can also be improved. The current topology requires a 40 mm foam separation between the radiator and the reflector, making the paper array inflexible after being attached to the foam. Thus for flexible mounting, it is desirable to explore other antenna element topologies to reduce the overall thickness of the array.

Chapter 5

MULTI_FREQUENCY LOW-PROFILE ARRAY (AEROSPACE)

5.1. Introduction:

In the previous chapter, the foam layer supporting the paper substrate was relatively thick, making the overall structure impossible to bend. To eventually achieve a conformal phased array that can be mounted on the curved surfaces of an aerospace vehicle, it is essential to reduce the overall thickness of the antenna element. For comparison, the paper array in Chapter 4 achieved a thickness of $\lambda/8$. In the literature, array thicknesses of $\lambda/7.5$ [52], $\lambda/6.4$ [53], $\lambda/29$ [54], and $\lambda/27$ [55] relative to the lowest operating frequency have been documented. They achieved a frequency ratio (FR), the ratio between the upper and lower frequency bands, of 3:1 [52], 1.8:1 [53], 7.5:1 [54], and 4:1 [55].

In this chapter, a low-profile, triple-band phased array unit cell element that achieves an FR of 16:2:1 is presented. The total thickness of the antenna is $\lambda/36$ with respect to the lowest operating frequency. A 1GHz, 2GHz, and 16GHz antenna achieves compact form factor and low coupling with a standard PCB fabrication process.

5.2. Antenna Design:

Several radiator choices were considered to reduce the low-frequency element's effect on the high-frequency element. Pokuls and Pozar [53] mentioned that slots on a ground plane have lower coupling to patch antennas than other metallic dipole/patch elements. Thus, a configuration consisting of low-frequency slot elements and high-frequency patch elements can be analyzed separately like two conventional single frequency arrays. Also due to the lower coupling, the high frequency pattern distortion is

reduced. However, a slotted ground plane needs to be elevated to reduce the capacitive, parallel-plate coupling with any structural ground plane behind it. The overall thickness needs to be reduced from $\lambda/6.4$ as mentioned in [53]. The section will discuss the slotted design at low frequencies (1 GHz and 2 GHz) follow by the high-frequency design at 16 GHz.

5.2.1. Low Frequency Element Designs: 1 GHz, 2 GHz

A cavity backed slot antenna (CBSA), shown in Figure 5.1, can eliminate the parallel plate mode between two ground planes by shorting the grounds with walls $\lambda/4$ distance along the E-field of a slot opening. With the short, a standing-wave electric field is formed inside the cavity to reflect the energy outside the slot and eliminates the parallel plate mode between the top and bottom ground plane. The major drawback of a CBSA is that for a cavity to be effective, no other vertical feeding network can go through the cavity. With the cavity occupying $\lambda/2 \times \lambda/2$ of the surface area, it is difficult to feed high-frequency elements that are located above the cavity.
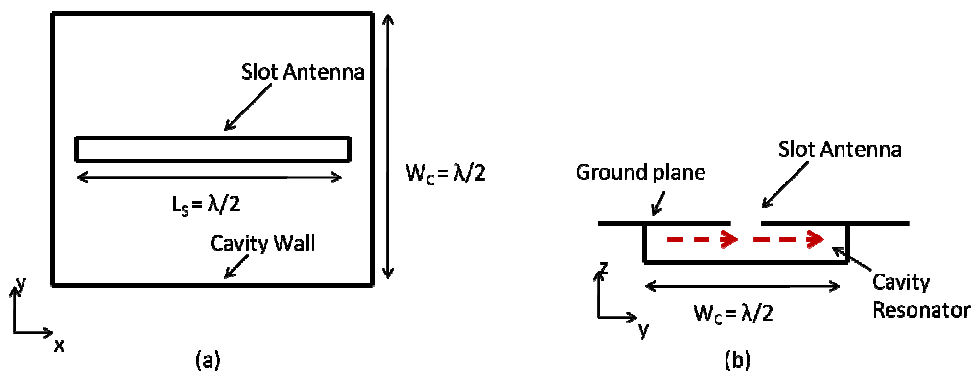
Figure 5.1 Cavity backed slot antenna. (a) top view, (b) side view. Red path indicates the direction of standing wave magnetic current.

Hong and Sarabandi introduced two methods of reducing the size a cavity. The first method cuts additional slot patterns into the top ground plane to reduce the overall size

51

[60]. This is not suitable to combine with the high-frequency patch elements since additional slots on the ground plane will interfere with microstrip patch mode on the surface. The second method, shielded parallel plate resonator, uses the meander cavity technique of bending the cavity with parallel plates and vias [61]. This method can reduce the width of the cavity without modifying the top ground plane. The second method is shown in Figure 5.2, where the width of the cavity, W_C, is reduced by a factor of 4 when a 4 layer cavity structure is used. However, the fabrication of this structure is difficult because the center conductor is realized using a hidden via wall. Also hidden vias require minimum width-to-substrate-thickness ratio for each layer, thus it will add to the overall width of the cavity.
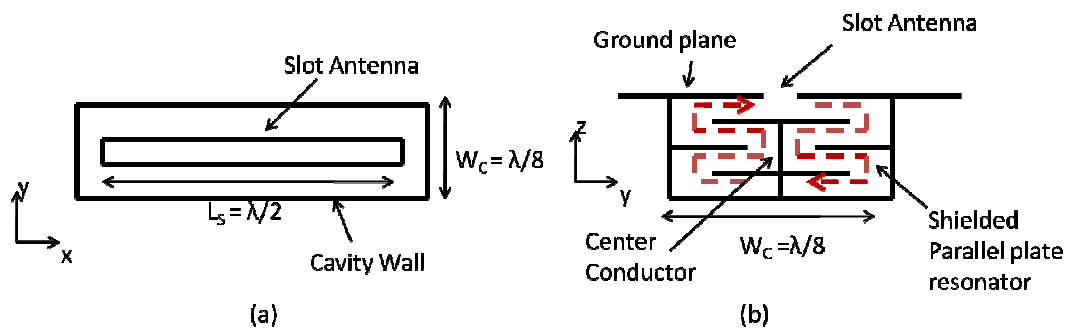
Figure 5.2 Shielded parallel plate resonator presented by Hong and Sarabandi [61]. (a) Top view, (b) side view with magnetic current in red shows the meander path in the cavity.

The parallel plate design can be further simplified by removing the center conductor as shown in Figure 5.3. This method offers similar performance without the construction of hidden vias. Because of the cavity symmetry, the electric field is cancelled to zero at the center of the lowest layer even without the presence of via wall. The simplified and the original parallel plate cavity allow additional space on the x-y plane for a coaxial feed to connect to the high-frequency patches on the surface.

52
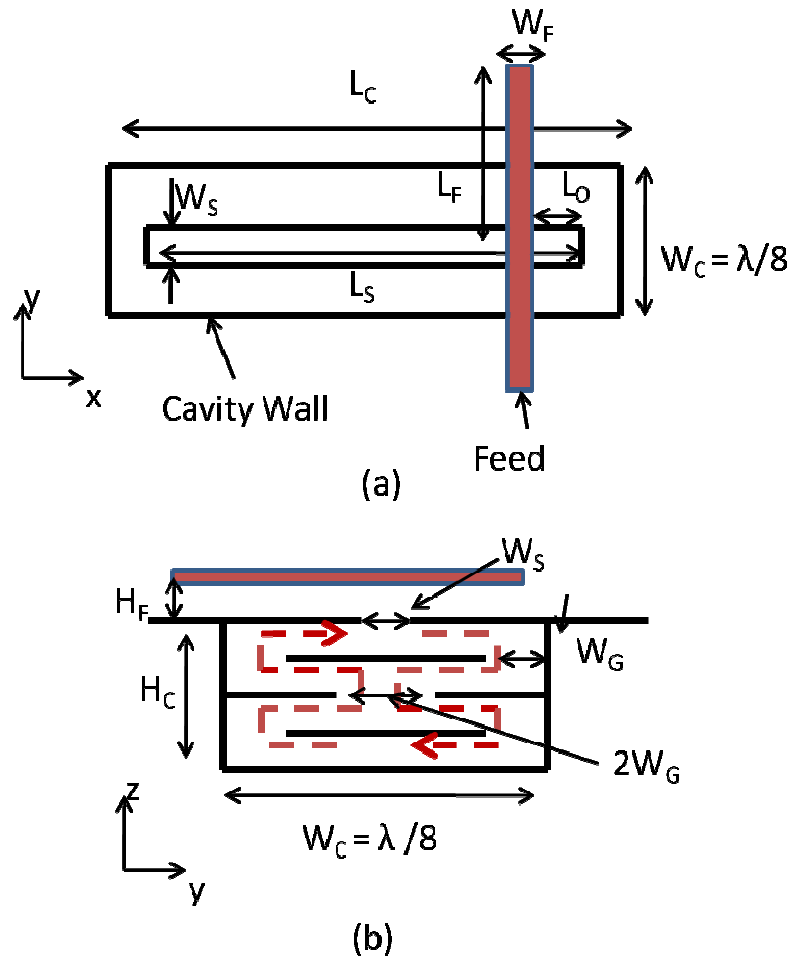
Figure 5.3 Proposed simplified parallel plate resonator that eliminates center conductor. (a) Top view showing cavity size with feed line, (b) side view with cavity dimensions.

The combined 1GHz and 2 GHz unit cell is shown in Figure 5.4. It consists of one 1 GHz slot antenna with four 2 GHz slots forming a unit cell. The dimensions are listed in Table 5.1 according to the symbols in Figure 5.3. The design consists of 2 boards: the cavity board and the feed board. The cavity board consist of four substrate layers of Rogers 3035 ($\varepsilon_r = 3.5$) each 1.5 mms thick and the feed board is made from one 0.75 mm-thick substrate layer of Rogers 3035. An additional 32 holes in the structure are used as the outer conductors for feeding coaxial ports for the 16 GHz elements.
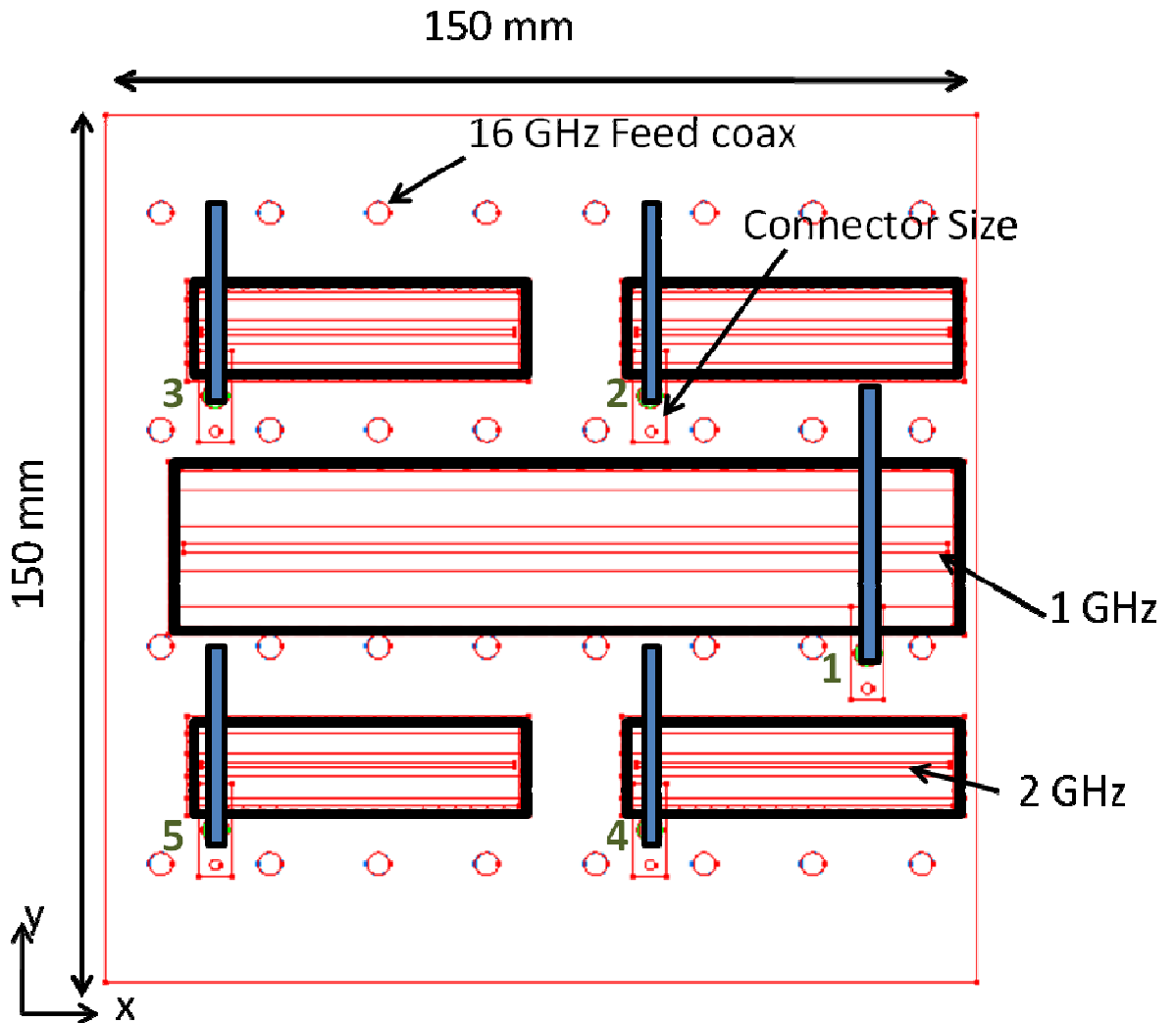
Figure 5.4 Low frequency array unit cell for 1 GHz and 2 GHz and the feeding positions for the 16 GHz elements. Port definition shown next to feed.

The cavity and feed boards are fabricated by Prototron Circuits with a standard PCB process. They are combined mechanically with 2.5 mm nylon screws. This design relies on the capacitance between the ground planes to conduct at RF frequencies, and may affect the resonance if the screws are loosened. Four-millimeter diameter flange SMAs are inserted through metalized vias to form a coax. An assembled low frequency prototype is shown in Figure 5.5.

Table 5.1
Dimensions of Low Frequency Antenna Elements (mm)

Frequency	1 GHz	2 GHz
W_S	1.5	1
L_S	132	54
W_C	28.4	15.5
L_C	135.4	57.4
H_C	6.1	6.1
W_G	4	2
L_F	28	20
W_F	1.72	1.72
L_O	14	2.4
H_F	0.75	0.75
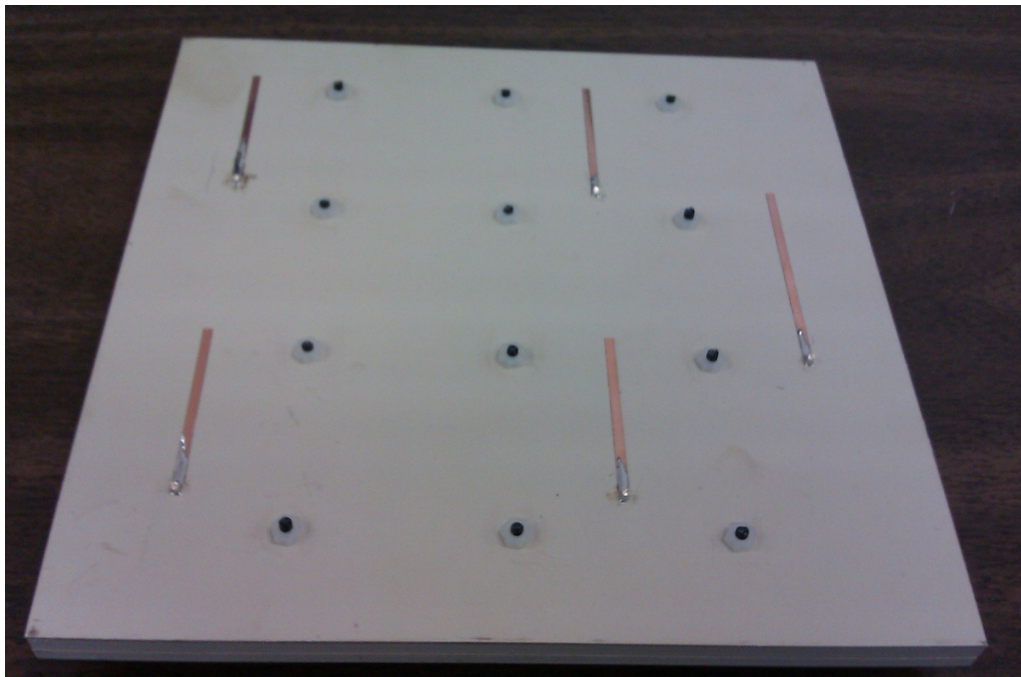
Figure 5.5 Fabricated low frequency unit cell for 1GHz and 2GHz.

The antenna is simulated using CST Microstripes, and measured using a VNA. The return loss of the 1 GHz and 2 GHz elements, shown in Figure 5.6 and Figure 5.7, demonstrates good agreement results between the simulation and measurement. Operating bandwidths of 15 MHz and 30 MHz are achieved at the 1 GHz and 2 GHz bands, respectively. The coupling between the 1 GHz and the 2 GHz element in Figure 5.8 shows good isolation between the two frequencies. In-band coupling is also

investigated by measuring the coupling between the 2 GHz elements as shown in Figure 5.9. Worst-case coupling of -15 dB is observed along the E-plane of the antenna between radiators 2 and 4. Low coupling allows the element impedance to be less affected by phase shifts from the neighboring elements, and is preferred for beam scanning.
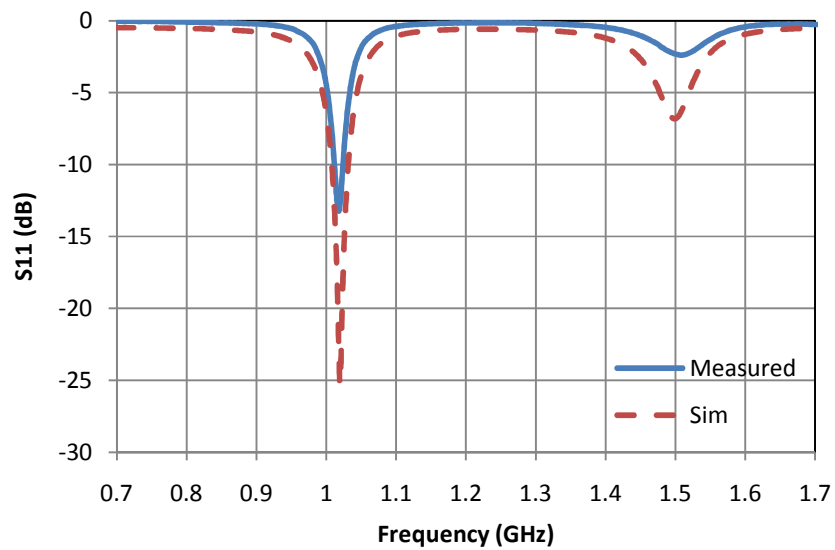
Figure 5.6 Simulated and measured 1 GHz return loss.
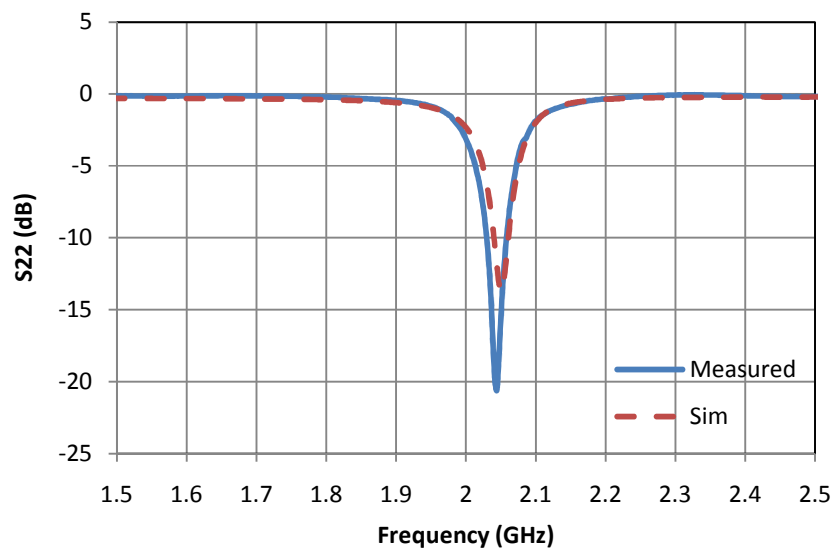
Figure 5.7 Simulated and measured 2 GHz return loss.
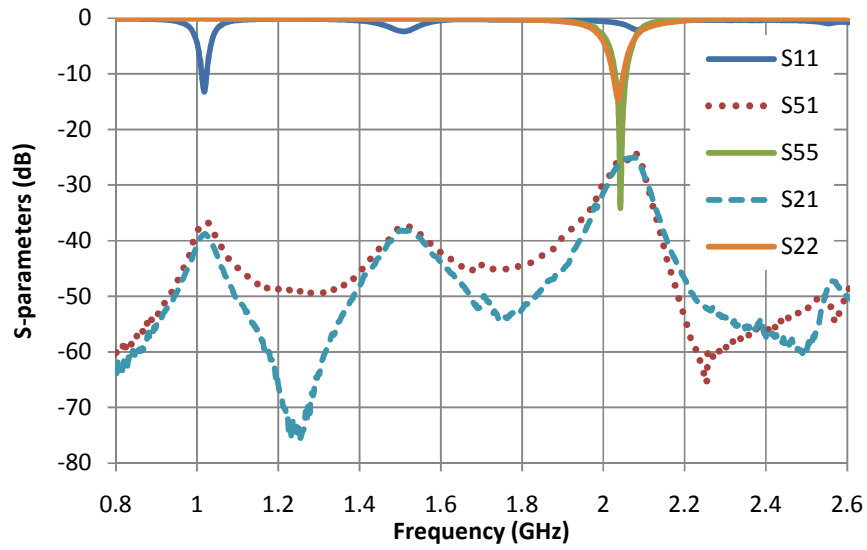
Figure 5.8 Measured coupling between the 1 GHz and 2 GHz elements.
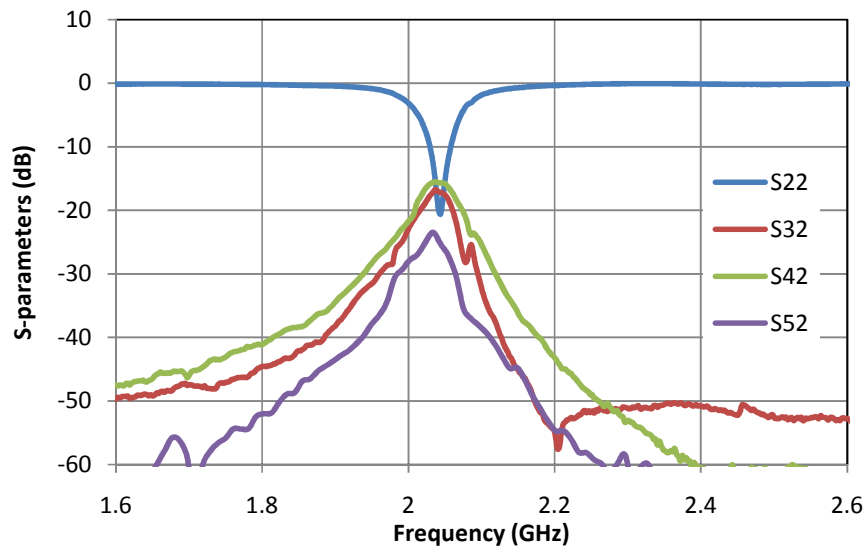
Figure 5.9 Measured coupling between the four 2 GHz elements.

The simulated radiation pattern of the unit cell in Figure 5.10 and Figure 5.11 shows good directivity. For a given unit cell, 6 dBi and 10.9 dBi dictivities are achieved for 1 GHz and 2 GHz, respectively. Note that the 2 GHz radiator consists of an array of four elements and naturally achieves 6 dBi more directivity than a single radiator. Also the

efficiency of the antenna will affect its realized gain, and can only be obtained through measurement.
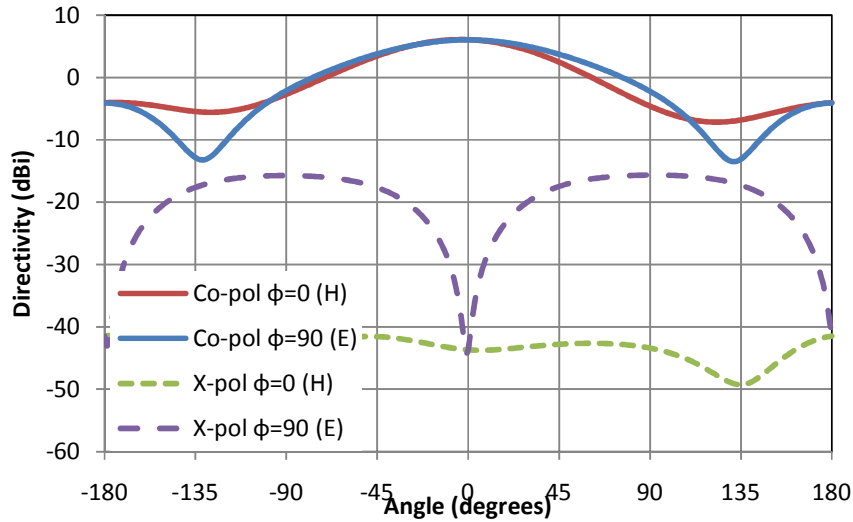
Figure 5.10 1 GHz radiation pattern.
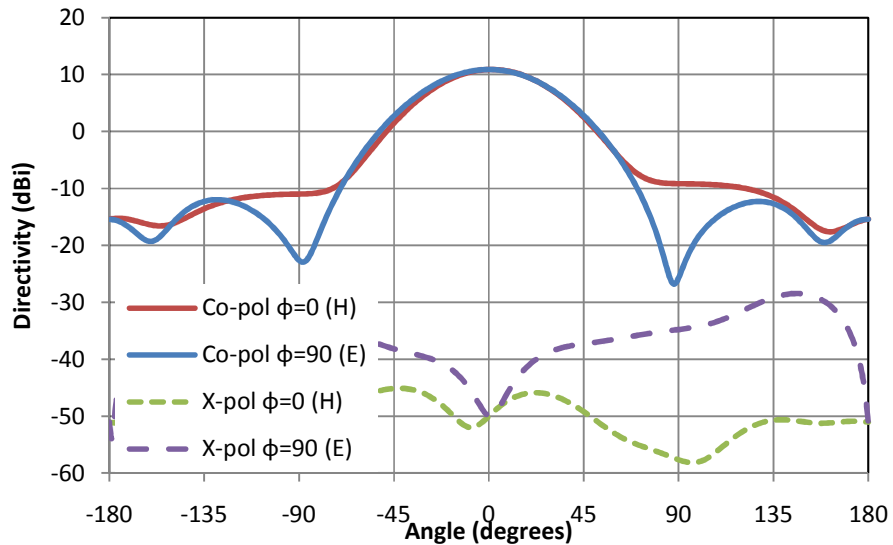
Figure 5.11 Unit cell 2 GHz radiation pattern when excited in phase.

5.2.2. High Frequency Element Design: 16 GHz

The unit cell also contains 256 16 GHz patch radiators above the 1 GHz, 2 GHz elements, which are difficult to feed. In the configuration shown in Figure 5.4, 32 SMA ports each feed a 2 × 4 sub-array. Physically, the size of the flange SMA connector

dictates the maximum number of high-frequency feeds in the unit cell. The physical limitation cannot be significantly improved unless another smaller-dimension measurement standard is used at the feed instead of SMA. As a result, a feeding network is needed for the 2×4 feed.

Two topologies were considered for the feeding network: microstrip and strip line configurations. First approach places microstrip feeding network on the same layer as the antenna requiring only one layer of substrate, and therefore is cheaper to manufacture. However, this approach is more susceptible to coupling as well as fabrication error. At 16 GHz, the protruding tip of the SMA center conductor and additional solder acts as an open circuit stub. Thus, the impedance matching can change greatly by process variation of the soldering from one 2×4 sub-array to another. Therefore, the second technique, a strip line feed, is used to provide better isolation and fabrication consistency.

The strip line feeding network is shown in Figure 5.12 for a 2×4 sub-array. It consists of 4 metal layers: patch, top ground, feeding network, and bottom ground. These metal layers are separated by three Rogers 3035 substrates with thickness of 0.75 mm. Since the SMA center conductor varies with soldering and wire cutting in the fabrication, the center conductor is shorted at the top ground layer instead. The short eliminates the open circuit stub variation and introduce a consistent short circuit stub that is fixed by the substrate thickness. The mismatch introduced is considered by modifying and tuning the original feeding network in ADS.
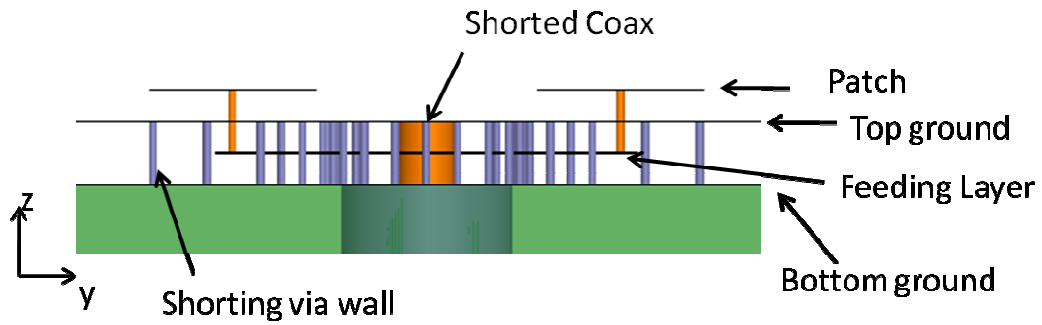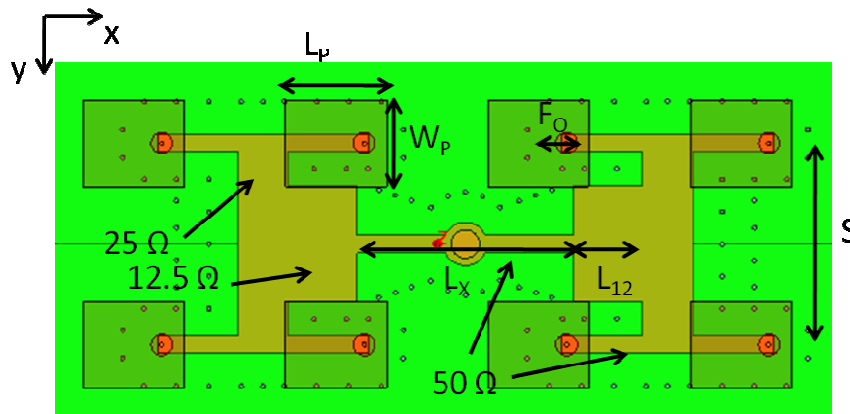
Figure 5.12 2-by-4 sub-array with feeding network at 16 GHz.

The impedance from each patch is first matched to 50 Ω at the center frequency by adjusting patch dimensions L_P, W_P, and F_O. The impedance is combined in parallel into 25 Ω and 12.5 Ω lines so that it will be closer to the impedance looking into the shorting stub. The widths of the lines are 0.82 mm, 2.34 mm, and 5.4 mm for the 50 Ω, 25 Ω, and 12.5 Ω lines respectively. The overall dimensions of the antenna are listed in Table 5.2.

Table 5.2
Dimensions of 2 × 4 High Frequency Sub-Array (mm)

Frequency	2 GHz
W_P	4
L_P	4.7
F_O	1.3
L_X	10
L_{12}	3.2
S	9.375

The overall unit cell combining the low frequency slot elements with the high frequency patches is shown in Figure 5.13. The design consists of a 6.1 mm cavity and a 2.25 mm high-frequency array board for a combined 8.35 mm overall thickness. This is λ/36 with respect to the 1 GHz operating frequency. Since the 16 GHz design has top and bottom ground layers, vias are drilled around the low-frequency slots so that no energy is leaked between the two grounds.
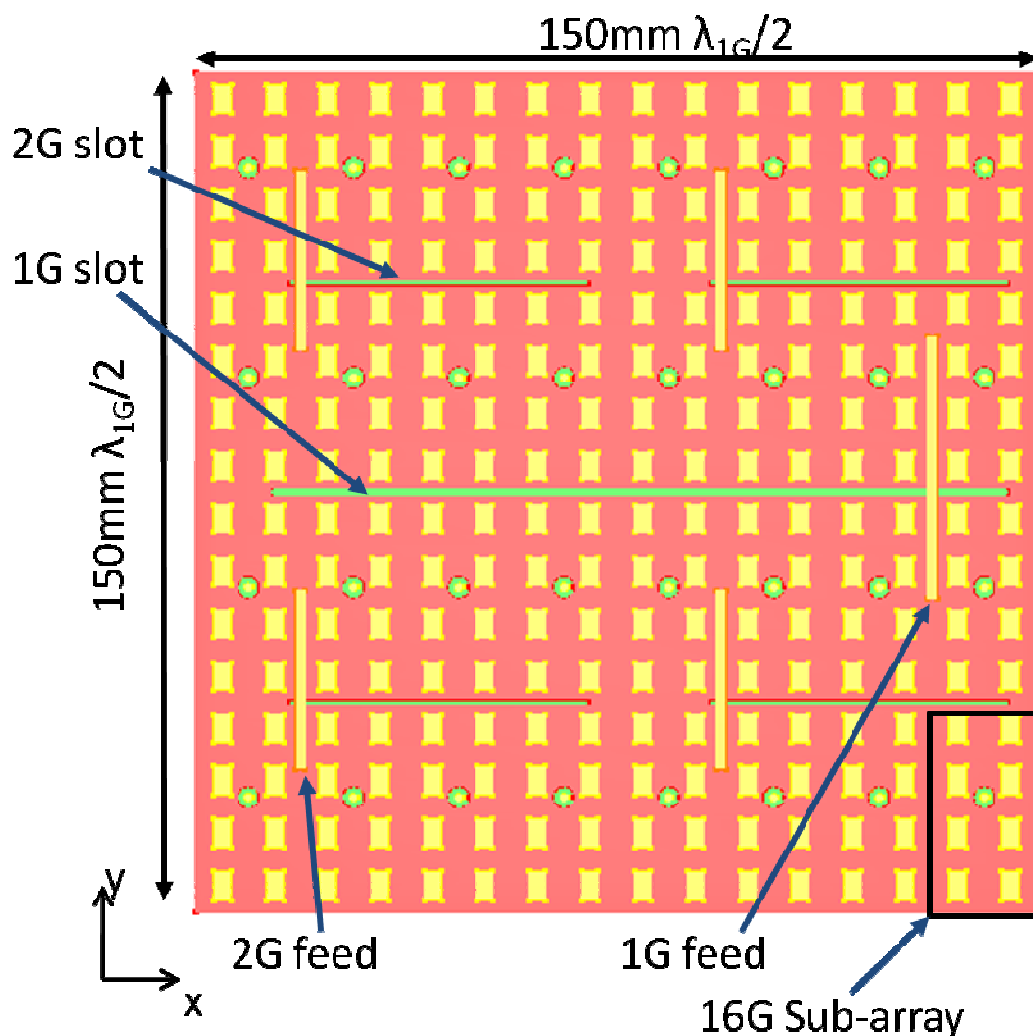
Figure 5.13 The complete top view of triple-band unit cell for the phased array.

The antenna is simulated with CST Microstripes to obtain the return loss and radiation pattern. The return loss of the 2 × 4 sub-array shown in Figure 5.14 exhibits a bandwidth of 500 MHz. The radiation pattern of the sub-array in Figure 5.15 achieved a directivity of 14 dBi and a side lobe level of 10 dB below the maximum. The radiation is similar to conventional uniform broadside patch arrays. To test the 16 GHz performance of the unit cell, 32 sub-arrays are excited in-phase at the same time to obtain the active driving impedance and broadside radiation as shown in Figure 5.16 and Figure 5.17, respectively. Active impedance bandwidth of 800 MHz is obtained, which is enhanced by the patch coupling with adjacent elements. A directivity of 28 dBi and side-lobe level of 13 dB is obtained for the unit cell at broadside.
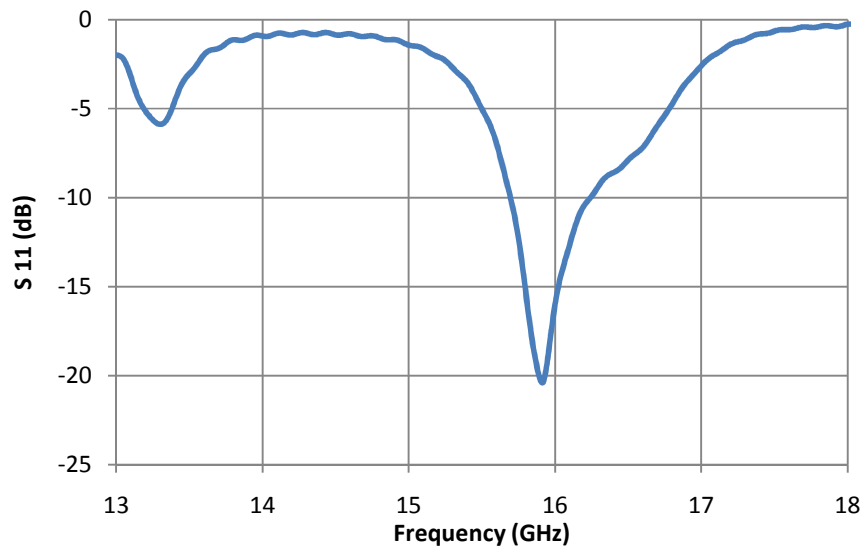
Figure 5.14 Return loss of the 2 × 4 sub-array.
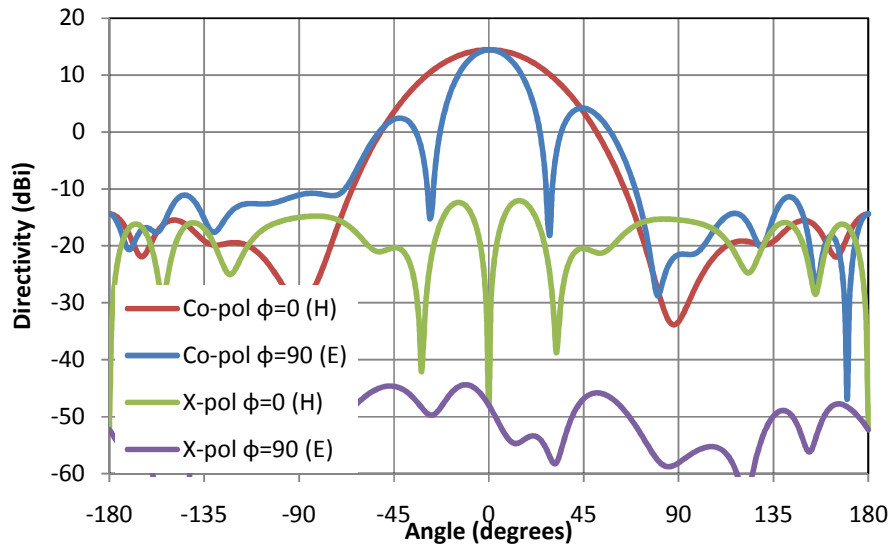
Figure 5.15 Radiation pattern of the 2 × 4 sub-array.
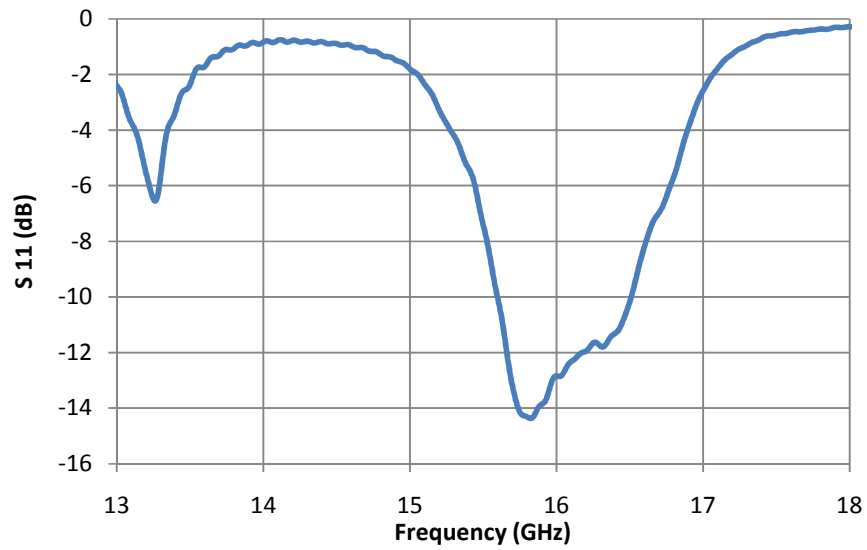
Figure 5.16 Return loss of the sub-array fed in-phase in the array unit cell.
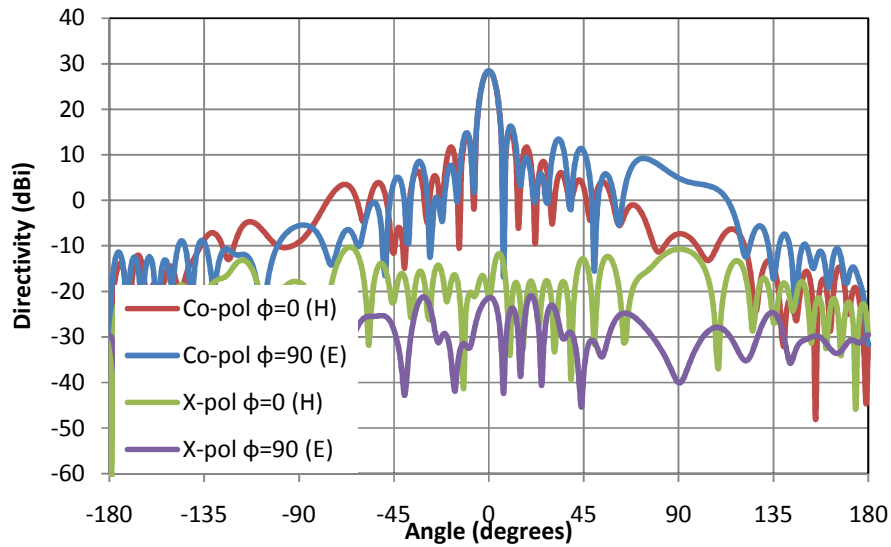
Figure 5.17 Radiation pattern of unit cell at 16 GHz when 32 sub-arrays are fed in-phase.

5.2.3. Conclusion

A triple-band phased array combining elements operating at frequency ratio of 16:2:1 is demonstrated in this chapter. Thus the same surface area for a 1 GHz unit cell is reutilized with higher frequencies to provide more functionality. Its low-profile thickness of λ/36 is similar to a conventional patch antenna. Thus, it has the potential to become a conformal array when fabricated on flexible substrates at higher frequencies. The array can be used in aerospace applications where the surface area is limited and the surface needs to be aerodynamic.

This design can be improved in several ways for eventual commercialization. The low frequency slot antenna bandwidth can be increased based on the needed application. Designing the array on flexible, multilayer substrates will present new challenges for feeding connectors through the substrate and adhesion between the layers. Additional analysis on the mechanical stability will be important for the design to identify the range of flexibility.

64

Chapter 6

OMNIDIRECTIONAL SOLAR ANTENNA FOR SENSORS

6.1. Introduction

Wireless sensor networks (WSN) are composed of a large number of sensor nodes densely deployed within a given area. Each of these sensor nodes has the capability of processing data and transmitting only the required information across the network [70]. These architectures provide better network reliability and easier deployment than traditional tethered sensor systems. The ease of deployment allows the implementation of cheap and pervasive networks that can impact a range of applications from medical monitoring, target/hazard detection to industrial/automotive control [71]-[73]. Existing deployments includes climate monitoring in the Huntington Botanical Gardens, structural monitoring of bridges, [74][75]. Furthermore, applications such as forest fire detection, wireless building security systems, and smart roads may be available in the years to come [76]-[78].

Node reliability is a major challenge for WSN quality of service that could drastically increase the cost of maintenance after deployment [79] Node malfunction can be caused by energy shortage, mechanical failure, sensor relocation, etc. To eliminate issues due to energy shortage, power harvesting mechanisms have been introduced to support the power consumption of every individual node [80]. Currently, solar panels harvest the largest reported amount of energy per area in outdoor environments and many designs have integrated them with sensor nodes' power management system [81].

Monopole antennas are currently used in the majority of WSN nodes because of their simplicity and quasi-isotropic radiation. However, monopoles positioned perpendicularly to ground are highly susceptible to mechanical damage such as being rolled over by a car or knocked over by an animal [82]. Such an event leads to wireless link failure of the node. This type of failures is currently reduced by avoiding the deployment of wireless sensor nodes in "hazardous" locations, where cars or animals can't move on top of them or extreme environmental conditions cannot displace them. Nevertheless, to realize truly ubiquitous and easy to deploy WSN, it is necessary to come up with a rugged antenna that offers structural durability and omnidirectional communication features. This antenna needs to be fully compatible with the solar panels that supply the sensors' power, while featuring a similar radiation performance to a monopole near grounding or shielding conductive planes.

Several authors have investigated designs and methods of integrating solar cells with antennas [83]-[86]. However, most of them are intended for ground-to-air satellite applications where most of the radiation is directed towards the zenith of antenna [83]-[85]. A study in [86] indicated that typical solar panels behave as imperfect conductors in the RF frequency range. Due to power circuitry connecting several solar cells together, solar panel becomes similar to a large RF ground that can potentially block or interfere with the transmitted RF signals of neighboring/underlying radiating elements.

Although numerous low-profile omnidirectional antennas have been introduced in the literature, such as the annular slot antenna (ASA) [87] and the monopolar patch [88]-[90], there has been no report on any integration with solar panels. An ASA, when placed underneath a solar panel, may have its radiation pattern distorted by solar cell's power

lines intersecting the slot because such configuration is similar to placing a short circuit across the slot [91][92]. Henze [86] introduced a omnidirectional solar antenna design by using an antenna topology similar to a monopolar patch as well as an ASA. However, the location of the power line intersecting the radiating solar cell was not addressed. Furthermore, in terms of design scalability, both the ASA and the monopolar patch are frequency dependent; their integration with different sizes of solar panels at different operating frequencies is a unique, specific design challenge of its own.

In this chapter, two omnidirectional solar antennas designs are presented: initial and scalable design. The two major advantages of these typologies are that they minimize the effect of solar cell on the antenna, and it is planar with nothing protruding the surface. Thus the antenna is easy to analyze and package. Section 6.2 describes the initial low-profile solar antenna design with its energy harvesting circuit. The design in section 6.3 further simplified the antenna by allowing solar panels of arbitrary size to be integrated with the antenna. The radiation patterns of these antennas are tested above a finite ground plane to demonstrate their radiation similarity with a standard monopole.

6.2. Omnidirectional Solar Antenna: Initial Design

In this section, the power and antenna backbone of a generic outdoor wireless senor node is designed. The power regulating circuit design of the sensor node is described in the first part. Based on the power circuit requirement, the design of a solar powered antenna is introduced in the second part.

6.2.1. Power Control Circuit

Several wireless sensor nodes exist on the market today. Most of them operate at 3 V and consume around 100-300 mW max during active wireless transfer [93][94]. In this

work, the power control circuit is designed for the TI CC2530 zigbee transceiver. A system-level diagram of the power regulating circuit is shown in Figure 6.1. The TI bq24031 chip is chosen to channel the solar cell energy between the sensor load and a lithium ion battery. A lithium ion battery has the advantage of low self-discharge and high energy storage density suitable for a compact wireless sensor node [95], but it is not the only battery option. A low self-discharge NiHM battery is also a good alternative for this application. To match the output voltage from the bq24031 chip to the 3 V sensor node input, a high efficiency buck converter, LTC1771, is used to step the 3.6-6 V variable output to 3 V. A complete schematic of the TI bq24031 with the LTC1771 is shown in Figure 6.2.
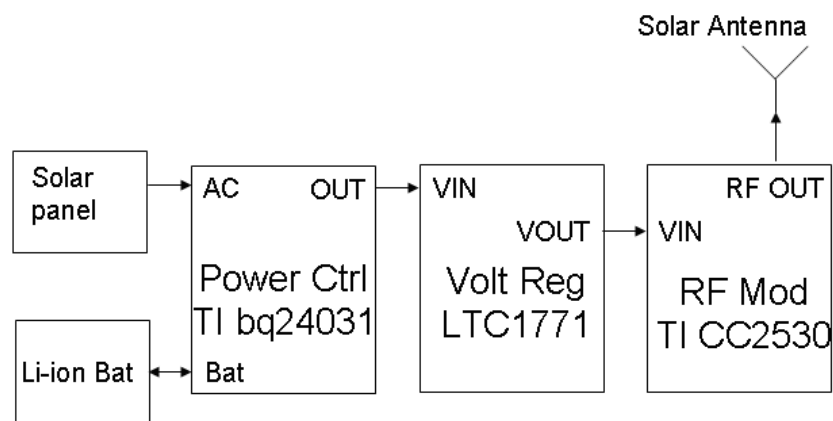
Figure 6.1. System diagram and device selectrion for power control circuit

Figure 6.2. Schematic of power regulating circuit

6.2.2. Planar Omnidirectional Antenna Design and Solar Circuit

The "solar-enabled" antenna consists of four metal layers, as shown in Figure 6.3. The top three layer thicknesses are given by PCBexpress's four-layer FR4 (ε_r=4.6~4.7) fabrication standard. The FR4 process is chosen because it is a cheap, industrialized process that is ready for immediate massive deployment.

70

Figure 6.3. Solar antenna layers. Metal layer deinition on left, substrate layer definition on right.

The slot antenna layer and the feeding network are shown in Figure 6.4. Slot radiators of approximately $\lambda/2$ in length are needed to excite the E-field perpendicular to the ground plane when the wave propagates along the ground. This is the same propagation orientation as the E-field generated by a monopole normal to the ground. Each opposing slot on an axis needs to be 180° degrees out of phase in order to generate an end fire pattern along its axis. The feeding network divides the input signal equally in the center of the slots and excites slots outward to generate the 180° degrees out-of-phase signal in the slots. The overall dimensions are shown in Table 6.1. The structure is simulated and optimized using HFSS. Figure 6.5 shows the simulated antenna return loss achieving a S11<-12 dB from 2.35 GHz to 2.5 GHz with/without the solar cell circuitry, for an elevation of 2cm above an infinite earth of $\sigma=0.01$ S/m and $\varepsilon_r=5$ [45]. The measured radiation is shown in Figure 6.6. These results show that the proposed antenna covers the 2.4 GHz to 2.5 GHz ISM band, and most of the energy is radiated away from the zenith.
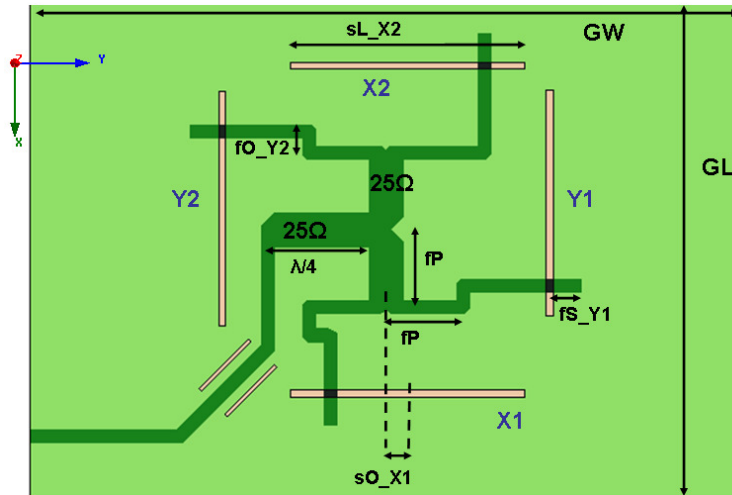
Figure 6.4. Slot antenna and feeding network layout (layers 2 and 3)

Table 6.1
Diomensions of solar anntena

h1	12 mils	fP	10.8	sL_X1,X2,Y2	32.9mm
h2	40 mils	fO (all)	3mm	sL_Y1	31.7mm
h3	5mm	fS (all)	4.5mm		
GL	150mm	sL_Y1	3.8mm		
GW	100mm	sL_X1,X2,Y2	3mm		
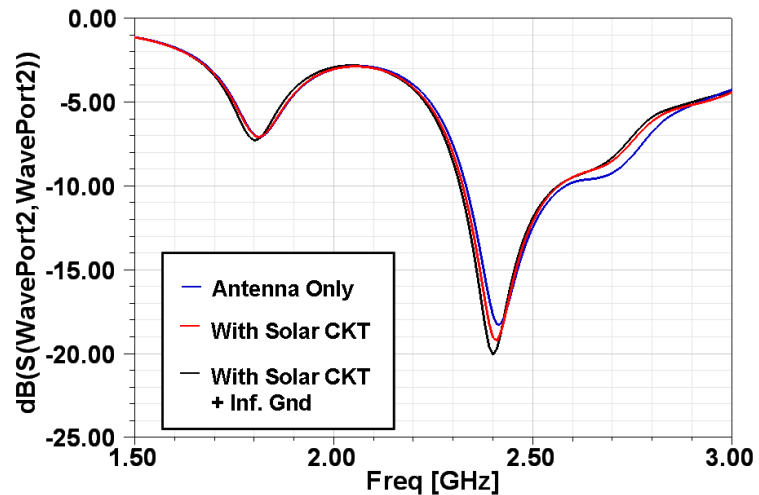
Figure 6.5. Simulated S parameter showing the effects of solar panel circuit to antenna matching.

72
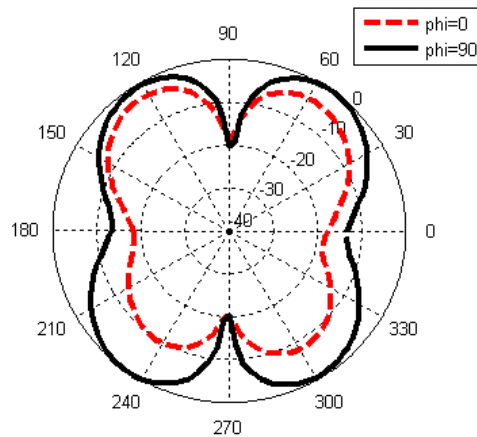
Figure 6.6. Measured radiation pattern with the antenna placed flat on the xy plane.

The bottom ground layer is critical for stabilizing the matching bandwidth of the slot antenna and providing ground isolation for the signal line. Figure 6.7 shows how the bandwidth of a single slot changes with the ground spacing h_3. The thickness of $h_3=5$ mm was chosen based on achieved bandwidth, compactness, and material availability. However, the presence of the bottom ground plane may also create a parallel plate resonance mode that distorts the slot radiation. The parallel plate mode ultimately makes the radiation similar to a patch antenna. In section 6.3, a cavity wall connecting the top and bottom ground plane is used to completely eliminate this parallel plate mode.
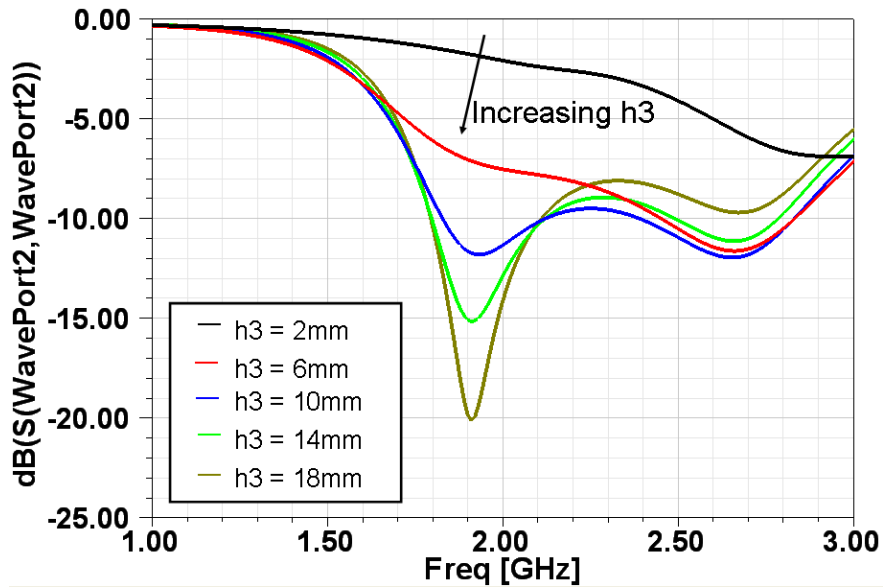
Figure 6.7. Return loss of a single slot due to h3.

The top solar cell circuitry shown in Figure 6.8 is positioned to avoid blocking the radiating slots from the second layer. The structure consists of 12 20 x40 cm, 0.6 Voc, monocrystalline silicon solar cells in series to generate a 7.2 V open circuit supply. The maximum power voltage of the structure would be 5.4 V assuming a worst case 25% voltage drop [96]. This is capable of charging lithium-ion battery at 4.2 V, along with supplying a wireless sensor node power at 3 V. The circuit mentioned in part 6.2.1 uses a voltage between 4.2 and 6 V to charge the battery at sleep mode, and discharge the battery to supply the wireless sensor node at low sunlight conditions. Combining these with the sleep and wakeup strategies mentioned in [80], compact autonomous nodes can be achieved.
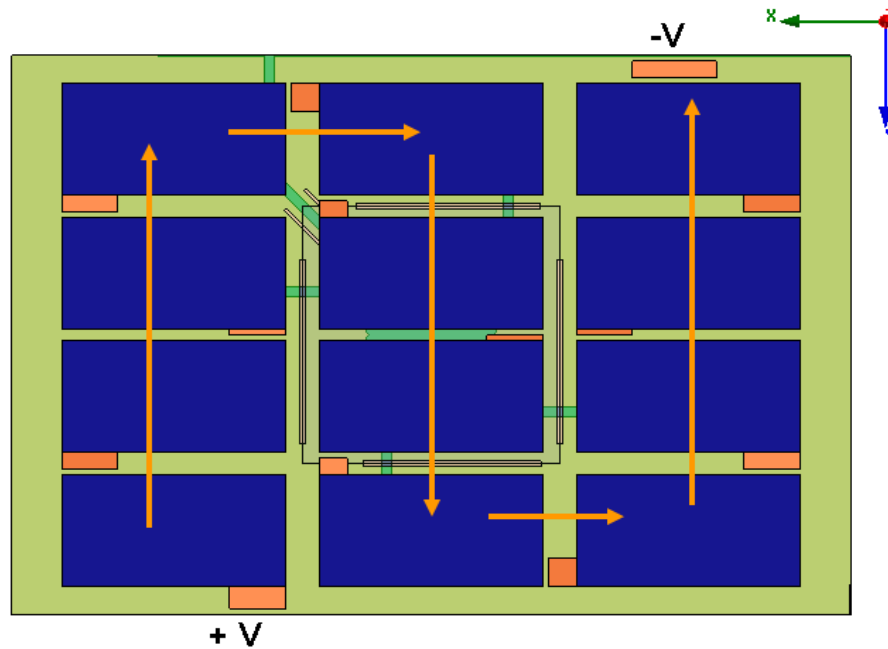
Figure 6.8. Layout of solar cell circuit

6.3. Omnidirectional Solar Antenna: Scalable Design

The disadvantage of the previous design is that solar panels are cut into pieces in order to fit with the location of the slots, adding to the fabrication cost. To further reduce cost, a scalable topology that allows integration of an arbitrary-sized solar panel with an omnidirectional antenna is presented in this section. As a proof of concept and without loss of generality, an antenna prototype hosting a 6×6 cm solar panel is designed for 2.4 GHz applications. The radiation performance of the antenna above a finite ground plane is studied to demonstrate its radiation similarity with a standard monopole.

The proposed 4-layer integrated solar cell - antenna stack-up is shown in Figure 6.9 and Figure 6.10. It consists of a 3-layer 62mils FR4 board ($\varepsilon r=4.65$, tan $\delta=0.018$) and an air cavity supported by 1 cm thick foam ($\varepsilon r=1$). The top metal layer represents the solar

panel. The second layer consists of a larger area RF ground plane that aims at isolating the solar cell from the underlying RF signal layers and providing radiating slot openings cut on all fours sides. The third layer carries the RF signal to be coupled and radiated through the slots. The stackup is backed up by a bottom (layer 4) solid copper ground plane. To provide a better ground isolation and eliminate the parallel plate mode in the structure, copper tape is applied around the board to connect the RF ground to the bottom copper plane forming a cavity of 4 slot openings.

Figure 6.11 gives the top view of the RF ground plane (magenta) and the RF signal pattern (brown) in layers 2 and 3 of the FR4 board. Layer 1 and 4 are not shown due to their simplicity. Layer 1 is one piece of solar cell placed in the center. Since the design isolates the effect of layer 1 of the antenna, it can have any shape or dimensions as long as it doesn't intersect/overlap with a slot on layer 2. The design dimensions of our preliminary prototype operating around 2.4 GHz are listed in Table 1. To host a 60×60 mm solar panel, an overall board dimension of 72×72 mm is chosen. Ideally, a smaller board dimension of 66×66 mm can be used without overlapping the 3 mm slot width, *Wa*, on each side, but additional space is added to leave room for fabrication error.
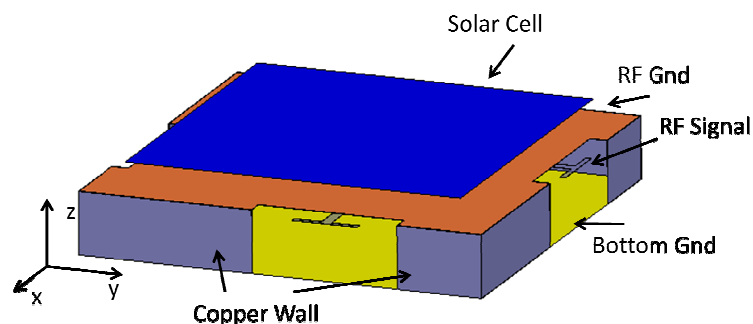
Figure 6.9 Angular view of the structure showing the solar cell and the conductor layers.

76

Figure 6.10 Layer stack-up of the solar antenna.

Figure 6.11 RF signal and ground layer of the design.

Table 6.2
Design Dimensions

Symbol	VALUE (MM)	Symbol	Value (mm)
H1	0.33	*WL*	1.85
H2	1.09	*Ws*	1
H3	10	*Ls*	11.65
Wq	5	*Wa*	3
Lq	18.5	*La*	26
Ld	16		

The RF power is divided equally among each of the radiating slots that are located symmetrically across the center of the design. The four lines that branch out to feed the slots have 50 Ω intrinsic impedance for *WL*=1.85mm. Two of them are combined into a

25 Ω line, which then combine at the center of the structure for a total intrinsic impedance of 12.5 Ω. By connecting the center to a 25 Ω quarter wave impedance transformer, the other end of the impedance transformer is converted back to 50 Ω and be fed by a standard SMA. High impedance lines are not used because they are too narrow for accurate fabrication. This feeding network allows the slots to be fed with same phase and power.

A slot is chosen as the radiator because the electric fields generated are vertical to any ground underneath the structure. In image theory, vertically polarized electric field is less affected by the ground reflection in comparison to horizontally polarized ones. Most wired antennas have poor performance when placed near and parallel to a ground plane because the ground image effectively cancels their horizontally polarized electric field. Each slot is excited by a T-shaped stub fed from the center. The slot length of 26 mm is slightly less than half-wave slot antenna on the FR4 substrate due to the T-shaped feed. Since the slot is located at the edge of the RF ground plane, it is difficult to terminate the feed line in a microstrip stub mode when no ground plane is present on the other side of the slot. Thus, the T-shaped stub eliminates the need for the signal line to re-enter into a microstrip mode after crossing the slot. Similar stub feeding can be found on some wideband slot antennas in the literature [97][98]. However, the presented structure is not wideband because the copper-taped cavity eliminates additional ground plane resonances in the structure. Other slot and feeding designs can also be considered to further improve the bandwidth.

The symmetrically placed slots dictate the radiation pattern of the antenna. Since each slot is fed in phase, the symmetry allows each slot to launch a wave front towards all four

directions along the xy plane at the same time. Thus the radiation pattern is close to omnidirectional.

The fabricated solar antenna prototype is shown in Figure 6.12. A solar panel of 6×6 cm is placed at the center of the structure without affecting the edge radiating elements. The percentage of solar cell utilization per overall area is 69%. The DC power can reach inside the cavity with minimal RF interference by wiring along the cavity wall. This design can be easily scaled up to fit larger solar panels to provide more power to the wireless sensor node as long as the substrate loss is low enough for the feeding network to be effective.
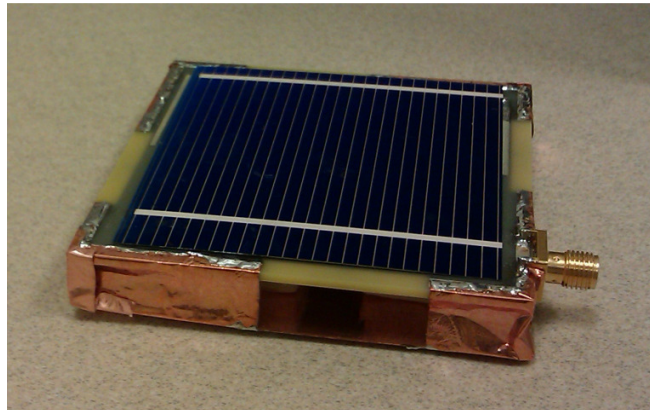
Figure 6.12 Fabricated solar antenna prototype.

The antenna is simulated and tuned using CST Microstripes 2010 in free space conditions. The solar cell is modeled as a 60×60 mm copper plate, and it has little effect on the performance due to the presence of the 72×72 mm RF ground plane. For the measurement, the antenna radiation and S11 is measured with and without the presence of a 50 cm diameter ground plane in SATIMO's anechoic chamber as shown in Figure 6.13. The measured and simulated S11 in Figure 6.14 shows good agreement between the predicted and measured result.
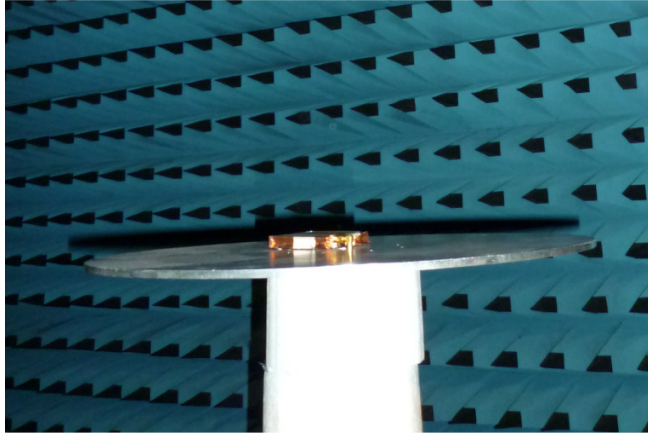
Figure 6.13 Measurement Setup of the antenna above a 50 cm diameter ground plane.
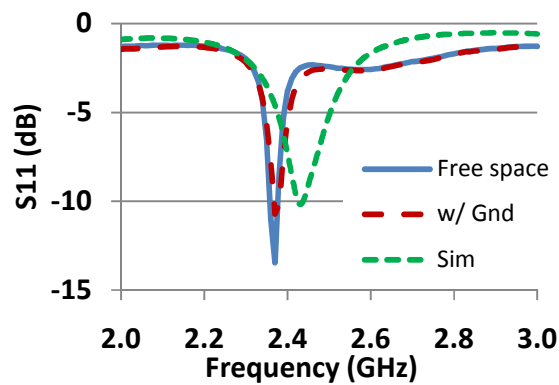
Figure 6.14 Simulated and measured S11.

The radiation pattern at 2380 MHz with and without a finite ground plane is shown in Figure 6.15. The measurement results demonstrate that the antenna has omnidirectional-behavior comparable to a standard monopole [45] even in the presence of a ground plane. The measured radiation efficiency is 49% in free space and 52% with the ground plane at the operating frequency. The loss is mainly due to the substrate loss in the FR4 at the feeding network and the stub termination. Simulated efficiency improved from 50% to 99% when FR4 loss is set to zero. The use of low loss substrate between the RF signal and ground can significantly improve the radiation efficiency.
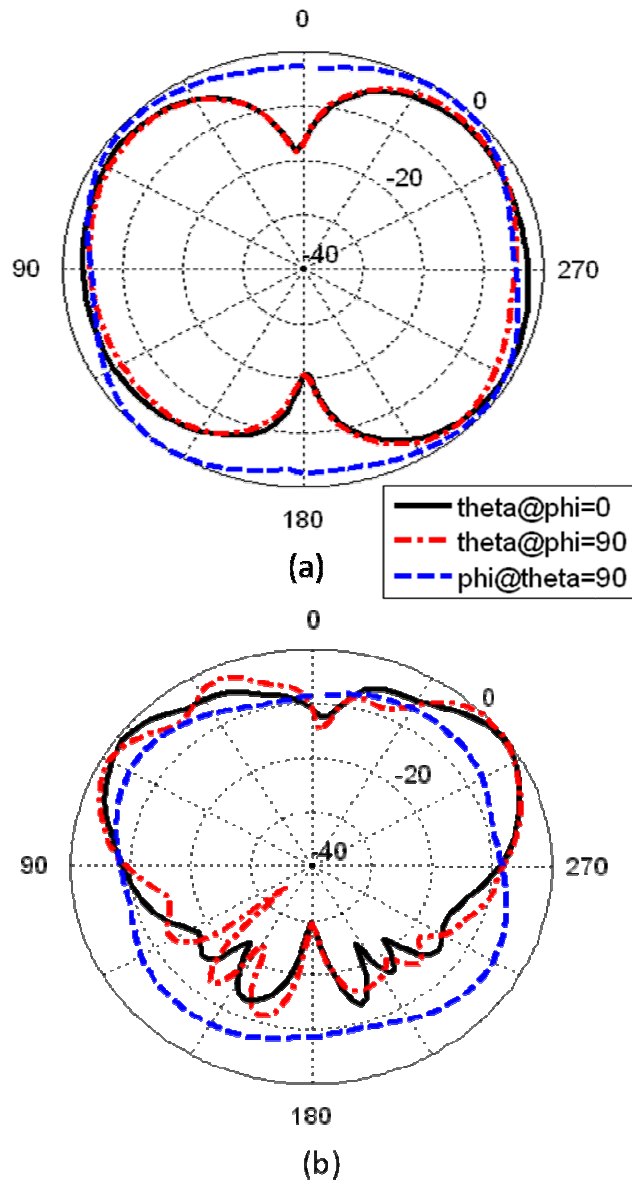
Figure 6.15 Measured radiation pattern normalized (a) in free space (b) placed above a 50 cm diameter ground plane.

6.4. Conclusion

A scalable low-profile omnidirectional antenna capable of integrating with a solar panel is presented. The antenna performance is comparable to a monopole antenna currently used in wireless sensor nodes. The antenna size can be easily modified to suit various solar panel sizes based on a sensor's power requirement. This work can enable

self-sustainable ubiquitous sensors to be placed in hazardous environments, such as roads, railways, rooftops and vehicles.

Some improvements in the design are needed before commercialization. Increasing the bandwidth and efficiency of the antenna can improve the communication range and increase the amount of frequency hopping channels. This can be achieved by experimenting with other radiating elements. Further study on the packaging of this solar antenna is needed to protect the brittle solar cells placed on the surface. These packaging materials will likely modify the resonance of the antenna, and will need to be addressed in the design.

Chapter 7

RFID WIRELESS STRAIN SENSOR

7.1.   Introduction

Structural health monitoring (SHM) systems utilize sensing technologies to monitor the condition of a structure (e.g. a mechanical, civil, or aerospace structure) in order to facilitate maintainance decisions, such as structural retrofitting [99], and enhance public safety. Among the various topics involved in SHM, the early detection of cracks for metallic structures (e.g. steel bridges or aluminum ships) has long been an important and challenging issue.

In a SHM system, stress/strain concentration is usually monitored as a premonition for fatigue or crack formation. Most of the current strain sensing techniques (e.g. metal foil strain gages or fiber optic sensors) require the wired installation of the sensor to a data acquisition system so that the analog sensor signal can be quantified [100]-[101]. To eliminate the high cabling cost for large structures, wireless sensing devices have been developed for digitizing and transmitting sensor data [102]-[103]. These devices usually require batteries or energy harvesters to supply power. For example, a number of energy harvesting techniques have been proposed [104]-[106]. In particular, the WISP (Wireless Identification and Sensing Platform) system offers a wireless power harvesting platform for strain measurements [107]. Nevertheless, the addition of power harvesting components and the built-in analog-to-digital converter (ADC) increases the cost and size factor of the sensing devices.

Other researchers have proposed passive wireless strain sensing through analog mechanisms to reduce the required onboard power [108]-[111]. By firmly attaching an electrical resonator to a structure and allowing its shape to change with the strain in the structure, the resonance frequency of the antenna shifts accordingly. This enables wireless reading of analog information without the use of onboard ADC circuits and RF amplifiers, thus greatly reducing the overall system power. In [108] and [109], the authors introduced wireless measurement with an inductive loop. However, inductive loops have limited communication range, which can be even shorter near metallic structural surfaces. The cylindrical cavity method proposed in [110] offers high Q response for detection, but can be costly to implement and difficult to attach to the surface of a flat metallic structure. Deshmukh and Huang [111] introduced a patch antenna that achieved 1 meter of read range on metallic objects with the use of a photodiode circuitry. The patch antenna concept is extended in this work to further improve read range by at least a factor of 2-3, reduce cost, enhance manufacturability, and effectively introduce individual sensor identities through the utilization of RFID tags [112]. RFID could tremendously enhance the applicability and scalability for large-area wireless sensor networks.

In this chapter, a low-cost RFID-enabled passive strain sensor has been developed based on a patch antenna design. Laboratory experiments show that the resonant frequency of the proposed antenna shifts accordingly with a small amount of strain/deformation, thus featuring a very good sensitivity. For the benchmarking prototype, the read range reached up to 2.5 meters, while a strain sensitivity of 0.76 kHz/$\mu\epsilon$ (microstrain) has been demonstrated. Furthermore, a novel theoretical derivation

of the sensor's strain sensitivity is presented, and corroborated by measurements of multiple sensor prototypes.

7.2. RFID Sensor Design

The measurement setup for wireless strain sensing is shown in Figure 7.1. The system consists of an RFID reader for wireless interrogation, as well as an RFID tag attached to an aluminum specimen under strain (introduced by a tensile testing machine). When a reader emits an interrogation electromagnetic wave to a completely-passive resonator, both the resonator and the surrounding environment reflect back to the reader antenna. The large reflection from the environment acts as a noise covering the resonator's response. To differentiate the sensor's reflection from the environmental reflections, time-gating techniques [110] or the combination of an open-and-short circuit response is needed to control the tag reflection [111]. In this study, a technique similar to the open-and-short circuit response is used. An RFID IC is used to generate a modulated backscattered signal to differentiate the tag reflection from the non-modulated environmental/background/ambient reflections [113]. Furthermore, RFID IC's are priced less than ten cents, making this approach particularly attractive for mass production. The SL3ICS1002 chip (manufactured by NXP Semiconductors) was chosen as the RFID IC chip; the small footprint of the chip causes minimal hindrance to the mechanical strain transfer from the aluminum specimen to the patch antenna.
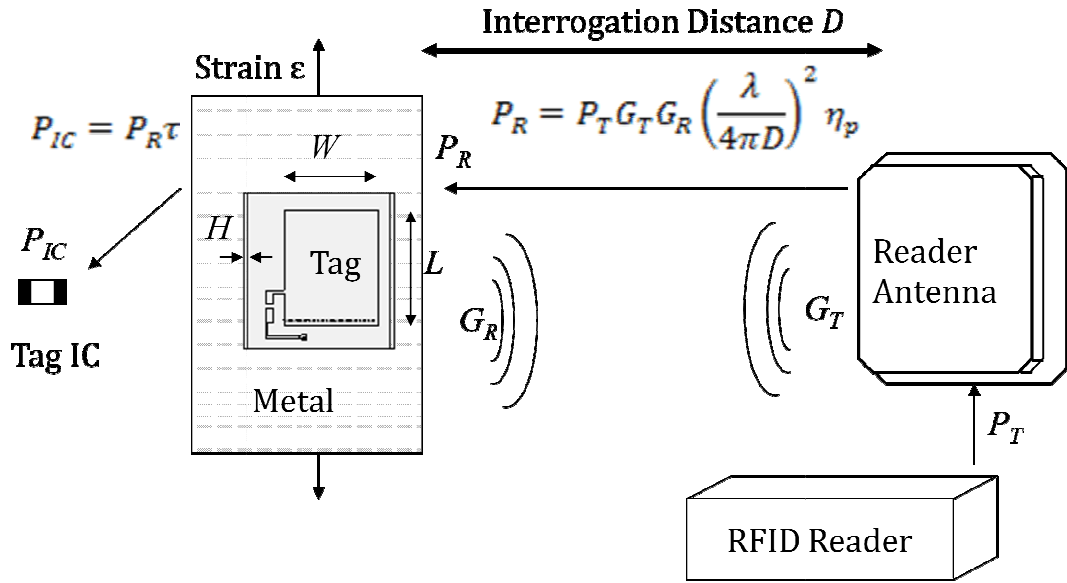
Figure 7.1 The measurement setup of RFID tag (i.e. strain sensor) with Friis transmission formula quantifying the forward path of the RFID interrogation. η_p is the polarization mismatch, τ is the power transmission coefficient between the RFID antenna and IC[113]-[114].

One pin (antenna connector) of the RFID IC chip was attached to a quarter-wave folded patch antenna while the other was connected to a matching inductor, as shown in Figure 7.2. The patch antenna of the tag operates in a "dual-mode" as both the communication component as well as the strain sensing element. The tag is built by standard PCB fabrication using Rogers 5880 substrate (a glass microfiber reinforced poly-tetra-fluoro-ethylene (PTFE) composite) with substrate thickness of H=1.5 mm and copper thickness of 17 μm. The dimensions of the copper antenna are $L \times W$ = 5.6×5 cm. The quarter-wave folded patch antenna topology is selected because it achieves smaller L and W dimensions than a regular half-wave patch antenna making it more suitable for measuring local strain. It should be noted that the size reduction also comes at the cost of additional via connections and reduced radiation directivity [115]. For maximum power

transfer to the IC, conjugate matching to the chip impedance is required to maximize the transmission coefficient τ. In this design, the conjugate matching is achieved by the utilization of a matching inductance generated by the 24 mm short circuit stub connected to the other pin (ground connector) of the chip.
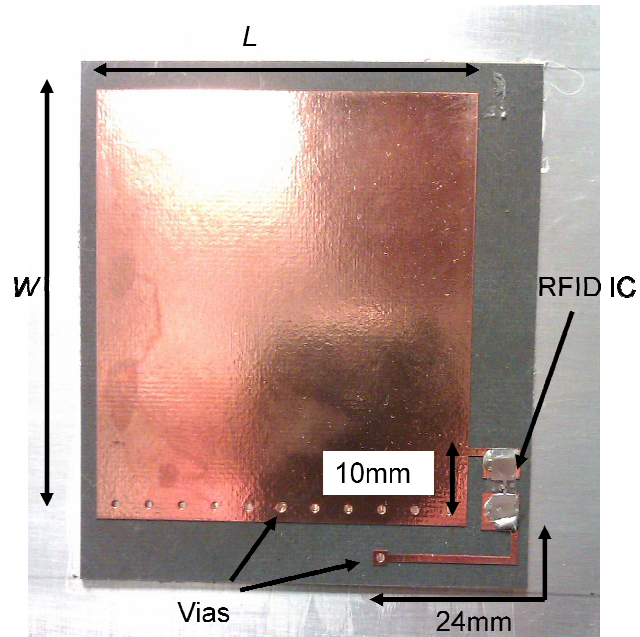
Figure 7.2 The design of the quarter wave patch antenna. The thickness *H* is 1.575 mm

For a quarter-wave folded patch antenna, the resonance frequency due to strain, ε, can be approximated with (7.1) assuming that only the metallic expansion of the patch affects the resonance.

$$f_{TM10} = \frac{c}{4\left[L(1+\varepsilon) + \Delta L\right]\sqrt{k_r}} \tag{7.1}$$

In the above equation, c is the free-space speed of light, L is the patch length, k_r (also referred as ε_r in the literature) is the dielectric constant of the substrate, and ΔL is the compensating additional length due to edge-fringe field defined in (7.2):

$$\Delta L = 0.412\, H\, \frac{[k_{r,eff} + 0.3]\left(\frac{W}{H} + 0.264\right)}{[k_{r,eff} - 0.258]\left(\frac{W}{H} + 0.813\right)} \tag{7.2}$$

$k_{r,eff}$ represents the effective dielectric constant of the microstrip patch [115]. The two equations show that when a patch is strained with 1000 με to the longitudinal (L) direction, L would increase by 0.1%, thus reducing the resonance frequency by ~0.1%.

A Voyantic Tagformance RFID reader was used to measure the turn-on power of the tag. To guarantee reading at different tag orientations, a circular polarized antenna was used at the reader side to interrogate the linearly polarized tag as shown in the measurement setup in Figure 7.3. The interrogation process measures the minimum transmitted power required from the reader to turn on the tag at various frequencies. The resonant frequency of the tag is identified as the interrogation frequency at which the least amount of power is required to be transmitted by the reader to activate the tag/sensor. Since this is analog data, the resolution and accuracy is dependent on the reader to act as a wireless ADC. The reader is capable of adjusting the transmitted power with 0.1 dBm of accuracy while sweeping the frequency in 0.1 MHz resolution. To further improve the measurement precision and reduce ambient noise, 10 samples are averaged and applied with 4th order curve fitting. The turn-on power transmitted by the reader for different strain levels is shown in Figure 7.4, when the sensor was interrogated from a distance of 30 cm.
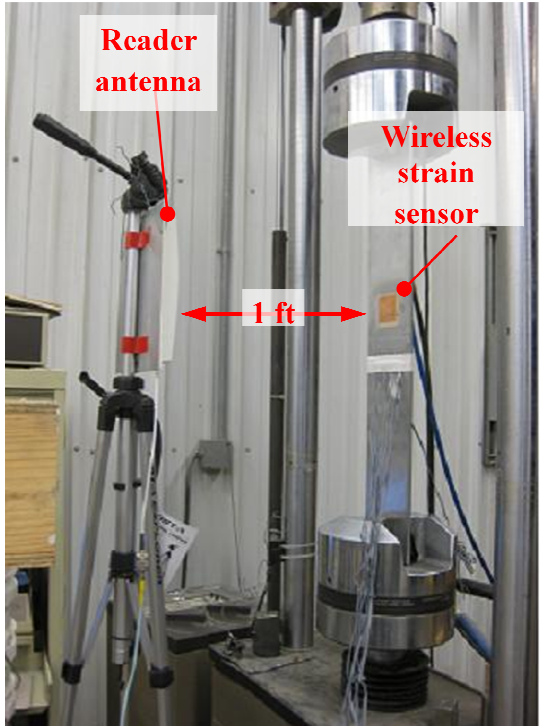
Figure 7.3 Measurement setup of the strain sensor.
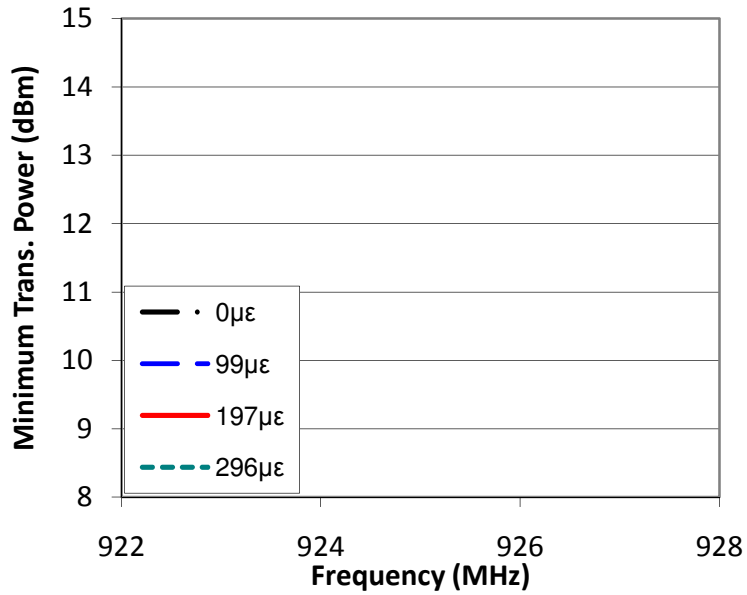
Figure 7.4 Transmitted power of the reader required to turn-on the RFID at four different strain levels.

Since the transmitted power level is relatively flat around the resonant frequency, the 3 dB bandwidth is used to determine the center frequency. Figure 7.5 plots the center frequencies against the strain levels. The sensor's strain sensitivity (0.76 kHz/με) is obtained as the slope of the linear regression. The difference between the measured and the predicted data is caused by the substrate expansion in the measurement not accounted for in the prediction model. A thorough analysis of the substrate effect is addressed in section 7.3.
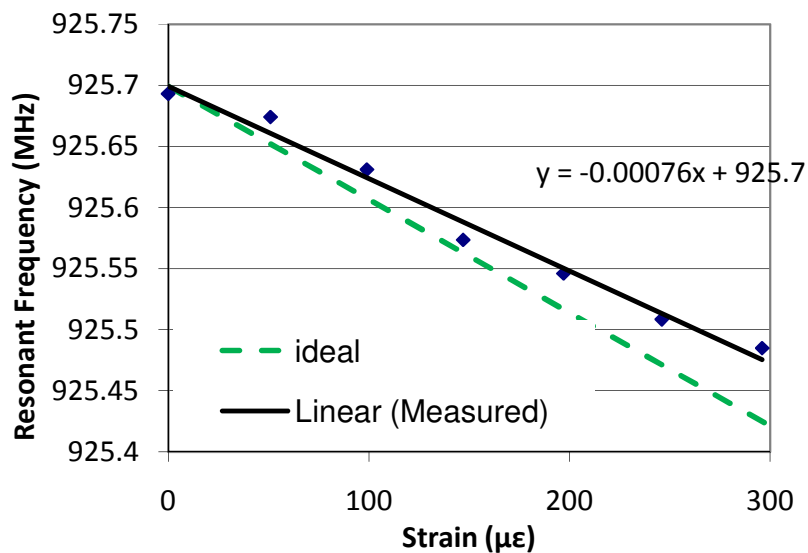
Figure 7.5 Measured strain sensitivity.

Because the sensor data is analog, a larger number of measured samples taken by the reader can yield higher strain resolution at the expense of measurement time. Resolution is the square root of the total samples taken. Thus, a 10 sample curve fitted data has a frequency resolution of 31.6 kHz which correlates to 41.8 με of detectable strain resolution with respect to the achieved strain sensitivity.

To test the strain interrogation range, the sensor (under zero strain) is moved away from the reader until the power at the center frequency is 3 dB less than the maximum

transmitted power of the reader. In Figure 7.6, the transmitted power of the reader recorded at various tag distances shows that the RFID sensor is capable of communicating up to 2.5 meters. The sensor range is ultimately bounded by the 4 W EIRP allowed in the United States.
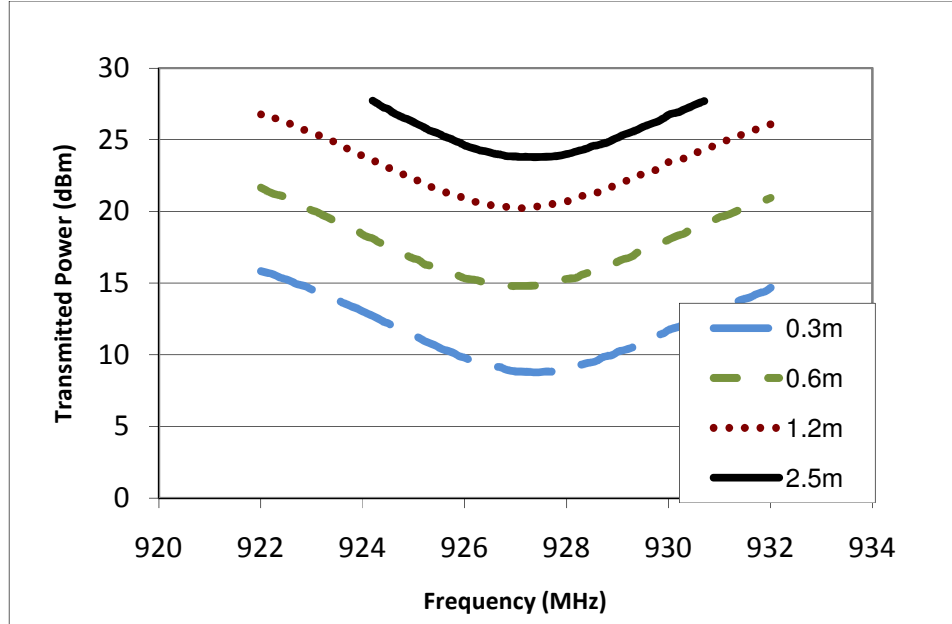
Figure 7.6 Transmitted power measured at various interrogation distances.

7.3. Theoretical Derivation of Strain Sensitivity

Strain sensitivity, the change in resonance frequency over change in strain, is theoretically bounded by (7.1). By taking the equation and normalizing it to an initial frequency f_0 at zero strain level, the direct idealized relationship between the resonance frequency and strain transfer can be derived as (7.3). For small strains, the relationship is approximately linear with a negative correlation of 1. A normalized sensitivity of f_0/Strain was provided by Tata and Huang [116].

$$f = \frac{f_0}{(1 + \varepsilon)} \approx f_0 - f_0\varepsilon \qquad (7.3)$$

91

The above equation assumes that only the antenna metal dimension changes with strain while other parameters in (1) remain constant. To improve the model accuracy, three factors affecting the measured sensitivity in (7.3) are proposed: i) the efficiency of mechanical strain transfer from the aluminum specimen to the top surface of the RFID tag, ii) the change in dielectric constant in the substrate due to strain, and iii) the change in the fringing field due to strain. Their effects are generalized by introducing the efficiencies η_M, η_k, and η_f in (7.4).

$$f = \frac{f_0}{\left(1 + \frac{L}{\Delta L + L}\eta_M \varepsilon + \frac{\Delta L}{\Delta L + L}\eta_f \varepsilon\right)(1 + \eta_k \varepsilon)}$$

$$\approx f_0 - f_0(\eta_M + \eta_k)\varepsilon$$

(7.4)

where η_M, η_k, η_f represent the efficiency of mechanical strain transfer, the dielectric constant change with respect to strain, and the fringing field change factor with respect to strain, respectively. Both η_k and η_f have a negative value for reasons that will be discussed below. In the case of thin substrate thickness (more suitable for strain transfer) where $L >> \Delta L$, η_f can be ignored. The derivation of these factors will be discussed in detail.

The efficiency in mechanical strain transfer η_M is quantified through both simulations and experiments, as summarized in Figure 7.7. A commercial mechanical simulation package, ANSYS, is used to calculate the percentage of strain transferred from the aluminum specimen to the copper antenna. Different thicknesses of substrates are simulated, using the same material properties of Rogers 5880. To validate the simulation results through experiments, strain gauges are mounted on top of the copper layer built on two different thicknesses (0.75 mm and 1.5 mm) of Rogers 5880 substrates. The

measured average η_M is 88% for the 0.75 mm substrate, and 82.5% for the 1.5 mm substrate. The results show that thinner substrates have a higher percentage of strain transfer and are thus more desirable for an RFID strain sensors. Compared with simulation results, the lower measured strain transfer is likely caused by the glue used to attach the substrate to the aluminum specimen. The copper thickness is 17 μm in both simulations and experiments. Note that increasing copper thickness also reduces the strain transfer percentage, as shown by simulation. Since increasing copper thickness offers no significant advantage to the electrical properties, the thinnest copper available should be used as long as it is greater than the conductor's skin depth. At 915 MHz, the skin depth of copper is 2.1 μm.

The strain sensitivity in (7.3) assumes that the dielectric constant of the substrate is unchanged due to strain, although in practice, increasing strain may deform micro-sized pores in the substrate and ultimately reduce the dielectric constant k_r. This reduction increases the sensor's resonance frequency and acts against the (decreasing) frequency shift caused by the increasing antenna length. Thus, it is desirable to quantify the reduction of k_r with respect to strain and minimize such reduction by selecting suitable substrates. The term η_k in (7.4) is used to characterize this effect, which is determined by substrate's dielectric properties and its volumetric expansion due to strain. The overall dielectric constant of a material, k_r, changes due to the ratio of pores to mass in the material, which is quantified by porosity, φ described by (5) [117][118].
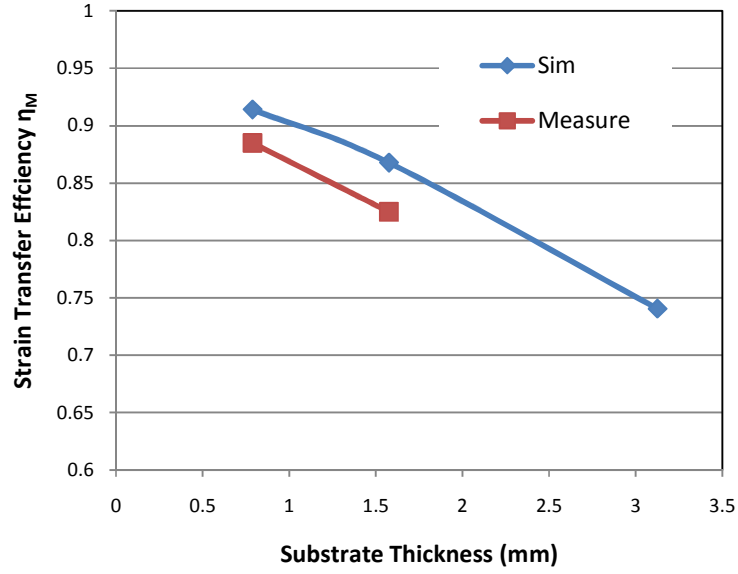
Figure 7.7 Average percentage of strain transferred to the top copper layer of the RFID tag for the common substrate thicknesses of Rogers 5880.

$$\frac{k_r - 1}{k_r + 2} = \varphi \frac{k_1 - 1}{k_1 + 2} + (1 - \varphi) \frac{k_s - 1}{k_s + 2} \tag{7.5}$$

In this equation, k_s is the dielectric constant of the film skeleton mass supporting the dielectric without any pores, and k_1 is the dielectric constant of the material inside the pores. In air, k_1 is 1, making the first term go to 0. Porosity is defined by the volume of void space over total volume [119]. By taking the derivative of porosity over total volume, (7.6) can be used to associate the change in porosity with the change in volume. V_M represents the volume of the dense film skeleton mass, which is used in the derivation.

$$d\varphi = \frac{dV}{V} \frac{V_M}{V} = \frac{dV}{V} (1 - \varphi) \tag{7.6}$$

The change in volume over strain is obtained from the linear model of Poisson's ratio of isotropic materials, v, as shown in (7.7).

$$\frac{dV}{V} \approx (1 - 2v)\frac{dL}{L} = (1 - 2v)\varepsilon \tag{7.7}$$

Combining (7.6), (7.7), and taking the derivative of k_r with respect to porosity ϕ in (7.5), the derivative of k_r with respect to strain ε can be represented by (7.8) and (7.9). A constant C is introduced to simplify the notation, and it has a value between 0 and 1.

$$\frac{dk_r}{\varepsilon} = \frac{-3C}{\varphi^2 C^2 + 2(1 - C)C\varphi + (1 - C)^2}(1 - \varphi)(1 - 2v) \tag{7.8}$$

$$C = \frac{k_s - 1}{k_s + 2} \tag{7.9}$$

To account for the square root term around k_r in (7.1), the value of η_k is represented as (7.10).

$$\eta_k = \frac{1}{2k_r}\frac{dk_r}{\varepsilon} \tag{7.10}$$

To visualize the magnitude of η_k for different substrates, Figure 7.8 shows the value of η_k at various C and ϕ values for Poisson's ratio v=0.4. Both Figure 7.8 and (7.8) demonstrate that by using substrates with larger porosity, higher v and smaller k_s, the magnitude of η_k can be reduced, thus minimizing its detrimental effect and improving the overall sensitivity. The material used for the dielectric skeleton determines k_s and v. For example, a PTFE-based dielectric has lower k_s and higher v than a ceramic-based one [120][121]. Thus, it achieves lower magnitude of η_k than the ceramic substrates.
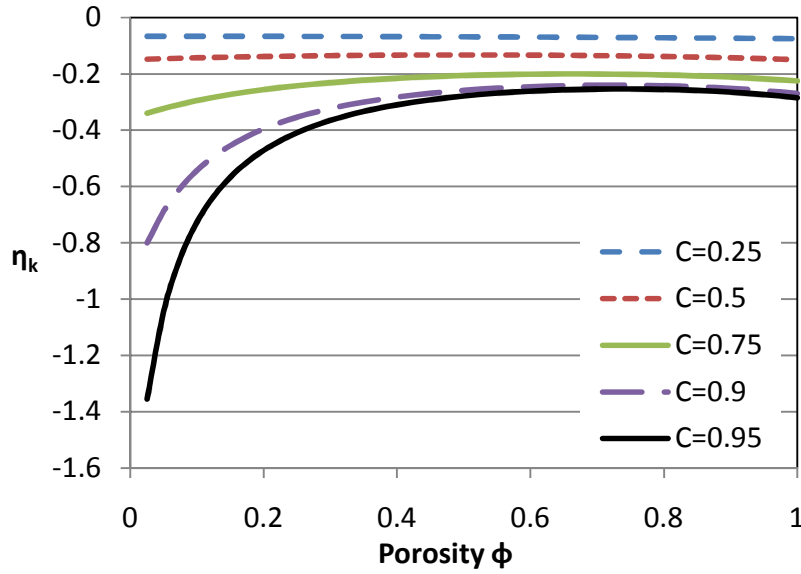
Figure 7.8 Change in η_k due to different porosity and C values. The Poisson's ratio v for this calculation is assumed to be 0.4 as an example, and it is linearly related to η_k.

Unlike η_M that has a maximum value of one (under perfect mechanical transfer), η_k must be a negative value that is substrate dependent. Figure 7.8 demonstrates the possibility of having a negative η_k with magnitude much greater than η_M in (7.4). In this case, a negative $(\eta_M + \eta_k)$ means that the resonance frequency increases due to experienced strain. By designing a sensor where the resonance is not affected by the copper length (such as exciting antenna modes orthogonal to strain), one can solely use the change in dielectric, η_k, to provide a positive correlation between applied strain and operating frequency. This is an interesting concept because the magnitude of η_k is not theoretically bounded, so the frequency shift in (7.4) can be more sensitive than the normalized f_0/Strain once the value of η_k becomes less than negative one.

The change in the compensating length of fringing field, η_f, due to strain is shown in (7.11). The equation, derived from the derivative of (7.2), assumes that W/H is much

greater than 1 and the contraction in *W* and *H* is the same. Most of the change is due to the contraction in height with respect to the Poisson's ratio, *v*. By using only the first term in (7.11) and assuming a Poisson's ratio of 0.3 to 0.4 yields a magnitude of 0.12 to 0.16 for η_f, This constitutes less than 1% loss after multiplying with $\Delta L/(L+\Delta L)$ in (7.4). The effect of η_f increases with substrate thickness and is negligible for thin substrates.

$$\eta_f \approx -0.412v\varepsilon - \frac{0.230}{(k_r - 0.258)^2} \frac{dk_r}{\varepsilon} \tag{7.11}$$

To verify equation (7.4), the strain sensitivities of patch antennas on different substrates, Rogers 5880 and Rogers 3003, are measured and compared in Figure 7.9. The value of $\eta_M + \eta_k$ can be derived from the slopes in the graph. Both substrates have a similar mechanical strain transfer efficiency of $\eta_M = 0.88$ for 30 mils (0.75 mm) substrates. This is due to similar Young's modulus and copper thickness of the two substrates. The measured η_k derived from Figure 7.9 is $\eta_k = 0.12$ for Rogers 5880 and $\eta_k = 0.52$ for Rogers 3003. This agrees with the predicted trend in Figure 7.8 and equations (7.8)-(7.10) that material with higher k_s and smaller v yields larger magnitude of η_k. By identifying the effects of η_k, higher strain sensitivity can be explored for future strain sensors based on patch antennas.
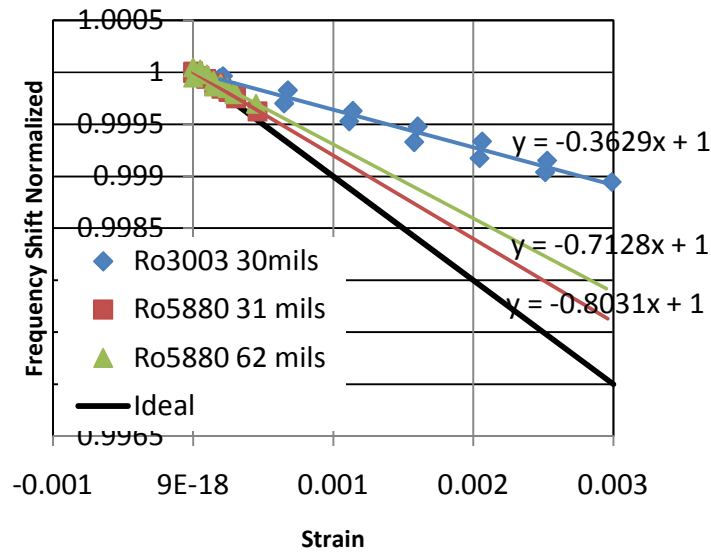
Figure 7.9 Normalized frequency shift of the sensor due to strain on the specimen.

7.4. Temperature Sensitivity

Temperature also changes the operating frequency of the sensor. As shown in (7.1), the resonance of a patch antenna is affected by the thermal expansion of copper as well as the thermal coefficient of dielectric constant of the material. For the Rogers 5880 material chosen, the thermal coefficient of -125 ppm/°C is given in the datasheet. The thermal coefficient greatly affects the temperature sensitivity, thus higher or lower temperature sensitivity can be achieved by the substrate selection.

To improve frequency resolution during testing, five samples were taken from Tagformance and curve fitted to obtain the sensor's center frequency. To reduce the temperature and environment variation during the measurement, the sensor was place in an anechoic chamber during the reading as shown in Figure 7.10. The measured result is summarized in Figure 7.11. The thermal coefficient of dielectric constant is high enough

that it dominates the resonance shift in sensor as predicted in the theory. A temperature sensitivity of 92 kHz/°C is obtained in the measurement.
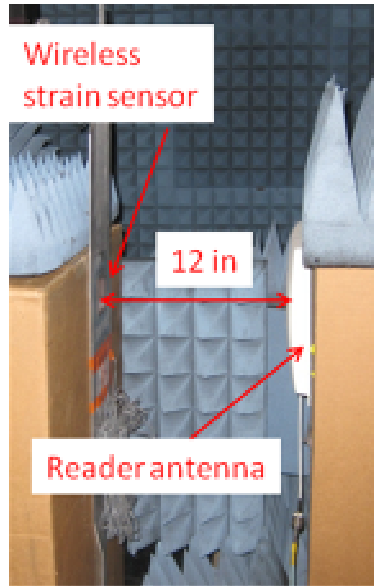
Figure 7.10 Temperature measurement setup in anechoic chamber.
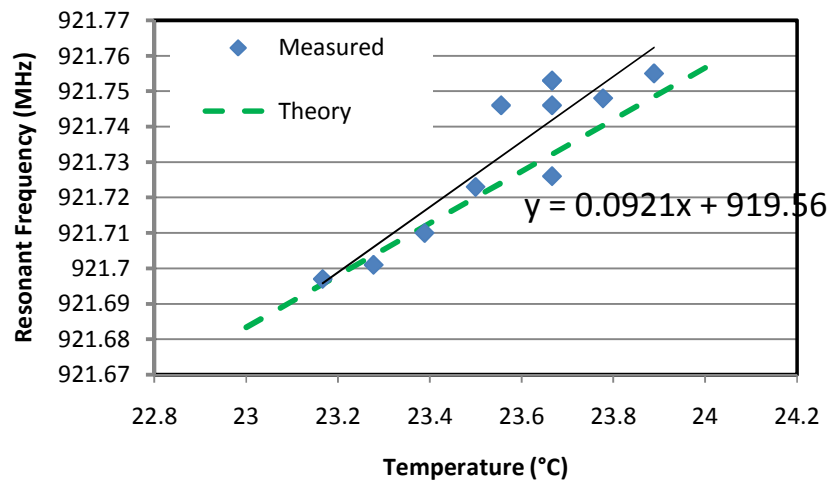
Figure 7.11 Measured temperature sensitivity compared to theory.

7.5. Moisture Sensitivity

Humidity also affects the sensitivity of the sensor. Since water is a high dielectric material (k_r = 80 @ 20 °C), water absorption in the substrate will greatly affect the overall dielectric constant. Moisture absorption quantifies the amount of water being absorbed by the substrate by measuring the weight increase in the structure after immersion. Hermetic substrates that minimize moisture absorption can be chosen to reduce the strain sensor's sensitivity to humidity and rain.

To quantify how much resonance change will occur in the sensor, the dielectric change will need to be quantified. Heinola [122] quantified the dielectric constant change in FR4 after being the substrate is submerged in water for 3 weeks. FR4 weight increased by 0.15% after the immersion process, and this added water resulted in a dielectric constant increase of 0.05 at 1 GHz. The results from this paper will be used to derive the moisture absorption of Rogers 5880 substrate used in this case. However, this analysis can be used on other substrates as well.

From the data sheet given for Rogers 5880 material, the moisture absorption is 0.015%, which is a figure much better than the FR4. The moisture absorption test was conducted by immersing a initially dried substrate in water for one day at 23 °C. Note that longer exposure to water may increase the water absorption in the substrate as demonstrated in [122]. The moisture absorption of Rogers 5880 is 10 times less than the FR4 in [122]. The volume of water inside the substrate has a direct correlation to the overall dielectric constant as noted in (7.5). The density of FR4 density is 1.86 g/cm^3, Rogers 5880 is 2.2 g/cm^3, and water is 1 g/cm^3. Thus, the volume of water in Roger 5880 is 8.5 times less than in FR4. Since the absorption is smaller than 1%, it is safe to linearly

add the dielectric constant of water to the initial dielectric constant of the substrate. Thus, a 0.015% water absorption results in additional 0.0058 added to the dielectric constant of the substrate.

To determine the sensor resonance, equation (7.1) is used. The resonance of the sensor is related to the square root of k_r. Thus the moisture sensitivity the sensor is depended on the square root of the dielectric change. The ratio between the square root of the wet and the dry dielectric constants of the substrate is found to be 1.0013. Multiply this ratio to k_r in equation (7.1), the sensor resonance shifts by 99.86% of the initial frequency. 0.9986 is the predicted normalized frequency change after a Rogers 5880 sensor is immersed in water for 1 day. Correlating that to the sensor's strain sensitivity of 0.76 kHz/με at 915 MHz, the immersion would create a shift equivalent of 1580 με experienced by the sensor. This is the worst case scenario of sensors being in direct contact with water. Thus a hermetic seal around the sensor is needed to achieve better humidity isolation in those environments.

In the case where the environment is humid, the resonance change due to water in the air is not as severe. At room temperature of 25 °C, water vapor is saturated at absolute humidity of 23 g/m^3 [123]. That humidity corresponds to 23 cm^3 of water in a cubic meter space. In a scenario where the substrate is 100% porous and is exposed to vapor in the air, the percent of water volume will raise the overall dielectric constant by 0.00184. This will result in a resonance shift equivalent to 550 με experienced by the sensor adding sources error in the strain measurement. The exact resonance shift will depend on the porosity, and the hydrophobic nature of each material. The maximum porosity material gives the worst case humidity sensitivity for a hydrophobic material.

7.6.   Conclusion

A low-cost passive wireless sensor that is based on a PCB-fabricated patch antenna used in UHF RFID frequencies has been developed for measuring strain on metallic surfaces. The resonance frequency of the antenna varies as the antenna elongates under stress. In addition, detailed theoretical formulations and experiments illustrates that the change in dielectric constant due to strain significantly affects the resonance frequency shift, and needs to be considered in wireless strain sensor designs to achieve higher sensitivity. The dielectric variation due to strain can also be used in the analysis of flexible optical and high frequency electronics. The temperature and moisture sensitivity of the sensor are also presented to quantify the possible noise in the system.

Future work can be done in the areas of improving the strain sensitivity, reducing temperature/moisture sensitivity, and deploying multiple sensors on the field. Higher strain sensitivity can be achieved by investigating high dielectric substrates that can shrink the size of the antenna and increase the normalized sensitivity beyond 1. 3D structures can also be considered in improving the strain sensitivity as long as they are mechanically stable and easy to mount. Exploring hermetic, low expansion materials can reduce the humidity and temperature noise seen by the sensor. When multiple sensors are deployed in proximity, the resonance shift due to coupling between the sensors needs to be considered as well.

Chapter 8

CONCLUSION

In this dissertation, antenna integration techniques for various applications are studied. The applications can be generalized by two groups: multi-frequency directive antennas and arrays for long range communication, and compact antennas integrated in sensors for low-cost wireless sensing. Contributions in these areas and future research directions are summarized in this final chapter.

8.1. Contributions

The dissertation has made contributions in the following areas:

- A novel base station antenna for cognitive radio is designed and tested to support commercial wireless standards from 800 MHz to 6 GHz. The design is similar to conventional base station antennas in many ways. Its radiation along the H-plane is consistent across all frequencies to allow sectoring of the network cells. It is also capable of being arrayed along the E-plane to provide wider coverage across the horizon.

- A dual-band nested element is designed and expanded into a phased array. This is the first array to be inkjet-printed on paper substrates. Paper offers low-cost, mechanical flexibility, and lightweight prototyping/fabrication.

- A novel triple-band unit cell of a phased array is developed by using a meander cavity. The overall thickness of $\lambda/36$ is currently the thinnest multi-frequency phased array. It also achieves a frequency ratio of up to 16 to 1.

This topology is constructed with a standard PCB fabrication, so it has the possibility to be fabricated on flexible substrates.

- A low-profile, omnidirectional antenna that can be scaled to fit an arbitrary-sized solar cell is designed and tested. This design is aimed for pervasive deployment of wireless sensor nodes, where node durability is important. The solar antenna is the first to offer energy harvesting and monopole-like radiation on a non-protruding platform.

- A novel RFID-based strain sensor capable of communicating up to 2.5 meters is designed and tested on metallic structures. This offers a low-cost alternative to existing microcontroller-based wireless sensors. The substrate-dependent strain, temperature, and humidity sensitivity of the RFID strain sensor are studied to calibrate out the possible environmental noise in the system.

8.2. Future Research

This thesis can be extended in a number of different directions, including:

- The multi-frequency phased array can be further developed on flexible substrates at higher frequencies. Mechanical simulations and measurements are needed to guarantee the durability of the array. Dual-polarized designs can also be investigated to see if a similar low profile topology can be achieved.

- For solar antennas, the impedance bandwidth and radiation efficiency can be improved by investigating other resonance structures and using low-loss substrates. Combining the solar antenna with existing wireless sensor nodes can be viable for commericial applications.

- RFID-based sensors can be improved in various ways. An array of sensors needs to be interrogated to check the feasibility of the massive wireless sensor deployment. A frequency doubler can be investigated to increase the operating frequency of the sensor and naturally reduce the antenna size. Embedding high dielectric constant material, like TiO_2, within the substrate can also reduce the antenna size. Based on the strain sensitivity derivation, high dielectric constant materials also have the potential to drastically improve the sensitivity beyond 1.0.

REFERENCES

[1]   A. Goldsmith, *Wireless Communications*, Cambridge University Press, 2005.

[2]   K.Lim, S.Pinel, M.F. Davis, A. Sutono, C. H. Lee, D. Heo, A. Obatoynbo, J. Laskar, E.M. Tentzeris, and R. Tummala, "RF-system-on-package (SOP) for wireless communications," *IEEE Microwave Magazine*, vol. 3, no. 1, pp. 88-99, March 2002.

[3]   R. Tummala, "Moore's law meets its match," IEEE Spectrum, vol. 43, no.6, pp. 44–49, Jun. 2006.

[4]   Chetan Sharma US wireless Data Market Update Q2 2009, Chetan Sharma Consulting. http://www.chetansharma.com/blog/2009/08/08/us-wireless-data-market-update-q2-2009/

[5]   Unmanned aerial vehicle, Wikipedia. http://en.wikipedia.org/wiki/Unmanned_aerial_vehicle

[6]   M. Horton, J. Suh, "A vision for wireless sensor networks," *IEEE MTT-S IMS Digest*, June 2005.

[7]   B. Warneke, M. Last, B. Liebowitz and K.S.J. Pister, "Smart Dust: communicating with a cubic-millimeter computer," *Computer*, vol. 34, no. 1 pp 44-51, Jan 2001.

[8]   RFID Tags, Alien Technology. http://www.alientechnology.com/tags/index.php

[9]   John Volakis, "Antennas & RF Sensors: Changing the Way We Live," EuCAP, March 2009.

[10] M.J. Brady, D-W. Duan and V.S.R. Kodukula, Radio frequency tag with miniaturized resonant antenna. US Patent # 6285342, Sep 2001.

[11] Scott Vance, "Multi-frequency band antenna device for radio communication terminal having wide high-band bandwidth" US Patent # 7388543, June 2008.

[12] S. Best, "On the resonant properties of the Koch fractal and other wire monopole antennas," *IEEE Antennas and Wireless Propagation Letters*, vol. 1, no. 1, pp74-76, 2002.

[13] L.J. Chu, "Physical limitations of omni-directional antennas", *Journal of Applied Physics*, Vol.19, pp. 1163-1175, 1948.

[14] R.C. Hansen, "Fundamental limitations in antennas," Proceedings of the IEEE, Vol.69, No.2, pp.170-182, 1981.

[15] Y.-W. Tseng, T.-W. Chiu, F.-R. Hsiao, S.-C. Lin, Y.-C. Chang, "Multi-Antenna Integration Module," US 2009/0066580 A1, US patent application, Aug 2008.

[16] M. Rotaru, Y.Y. Lim, H. Kuruveettil, R. Yang, A.P. Popov, and C.P. Chua, "Implementation of packaged integrated antenna with embedded front end for Bluetooth applications," *IEEE Transactions on Advanced Packaging*, vol. 31, no. 3, pp. 558-567 Aug 2008.

[17] J. Lin and T. Itoh, "Active integrated antennas," IEEE MTT Transactions, vol.42, no.12, part 1-2, Dec 1994.

[18] S.P. Kingsley, J.M. Ide, D. lellici and S.G. O'Keefe, "Radio and antenna integration for mobile platforms," The 9th European Conference on Wireless Technology, pp.79-82, Sep 2006.

[19] H.A. Wheeler, 'Fundamental Limitations of small antennas,' *Proceedings of the IRE*, pp 1479-1488, Dec1947.

[20] L.J. Chu, 'Physical limitations of omnidirectional antennas,' *Journal of Applied Physics*, Vol. 19, pp. 1163-1175, Dec 1948.

[21] R.F. Harrington, 'Effect of antenna size on gain, bandwidth and efficiency,' *Journal of Research of National Bureau of Standard*, Vol. 64-D, pp. 1-12, Jan/Feb 1960.

[22] R.E. Collin and S. Rothschild, 'Evaluation of antenna Q,' *IEEE Transactions on Antennas and Propagations*, Vol. AP-12, pp. 23-27, Jan 1964.

[23] J.S. McLean, 'A re-examination of the fundamental limits on the radiation Q of electrically small antennas,' *IEEE Transactions on Antennas and Propagation*, Vol. 44, no. 5, pp. 672-676, May 1996.

[24] V.I. Slyusar, '60 Years of Electrically Small Antennas Theory,' *International Conference of Antenna Theory and Techniques*, pp. 116-118, Sep 2007.

[25] Bhatti, R.A., Yun-Taek Im, and Seong-Ook Park, "Compact PIFA for Mobile Terminals Supporting Multiple Cellular and Non-Cellular Standards," *Antennas and Propagation, IEEE Transactions on* , vol.57, no.9, pp.2534-2540, Sept. 2009.

[26] Ya-Chung Yu, and Jenn-Hwan Tarng, "A Novel Modified Multi-band Planar Inverted-F Antenna," *Antennas and Wireless Propagation Letters, IEEE* , vol.8, no., pp.189-192, 2009.

[27] P. Salonen, M. Keskilammi and M. Kivikoski, "Single-feed dual-band planar inverted-F antenna with U-shaped slot," *IEEE Trans. Antennas Propagat.,* Vol. 48, pp.1262-1264, 2000.

[28] W.-C. Liu, W.-R. Chen, and C.-M. Wu, "Printed double S-shaped monopole antenna for wideband and multi-band operation of wireless communications," IEE Proc.-Microw. Antennas Propag. vo1. 151, no. 6, pp. 473-476, Dec 2004.

[29] RongLin Li, Bo Pan, J. Laskar, and M. M. Tentzeris, "A Compact Broadband Planar Antenna for GPS, DCS-1800, IMT-2000, and WLAN Applications," *Antennas and Wireless Propagation Letters, IEEE* , vol.6, no., pp.25-27, 2007.

[30] RongLin Li, Bo Pan, J. Laskar, and M.M. Tentzeris, "A Novel Low-Profile Broadband Dual-Frequency Planar Antenna for Wireless Handsets," *Antennas and Propagation, IEEE Transactions on* , vol.56, no.4, pp.1155-1162, April 2008.

[31] RongLin Li,. Bo Pan, T. Wu, J. Laskar, and M.M. Tentzeris, "A triple-band low-profile planar antenna for wireless applications," *Antennas and Propagation Society International Symposium, 2008. AP-S 2008. IEEE* , vol., no., pp.1-4, 5-11 July 2008.

[32] RongLin Li,. T. Wu, and M.M. Tentzeris, "A triple-band unidirectional coplanar antenna for 2.4/3.5/5-GHz WLAN/WiMax applications," *Antennas and Propagation Society International Symposium, 2009. APSURSI '09. IEEE* , vol., no., pp.1-4, 1-5 June 2009.

[33] CST Microstripes. http://www.cst.com/Content/Products/MST/Overview.aspx

[34] J. Mitola III, "Cognitive Radio for Flexible Mobile Multimedia Communication", *Proc. IEEE International Workshop on Mobile Multimedia Communications (MoMuC) 1999*, pp 3-10, Nov. 1999.

[35] K. Lim and J. Laskar, "Emerging Opportunities of RF IC/System for Future Cognitive Radio Wireless Communications," *IEEE Radio and Wireless Symposium*, pp. 703-706, Jan 2008.

[36] P.S. Hall, P. Gardner, J. Kelly, E. Ebrahimi, M.R. Hamid, and F. Ghanem, "Antenna Challenges in Cognitive Radio," *International Symposium on Antennas and Propagation*, Oct. 2008.

[37] M.K. Fries, M. Grani, R. Vahldieck, "A reconfigurable slot antenna with switchable polarization," *IEEE Microwave and Wireless Components Letters*, vol 13, issue 11, pp. 490 – 492, Nov. 2003.

[38] B.A. Cetiner, H. Jafarkhani, Jiang-Yuan Qian, Hui Jae Yoo, A. Grau, and F. De Flaviis, "Multifunctional reconfigurable MEMS integrated antennas for adaptive MIMO systems," *IEEE Communications Magazine*, vol. 42, issue 12, pp. Page(s):62 – 70, Dec. 2004.

[39] A.E. Fathy, A. Rosen, H.S. Owen, F. McGinty, D.J. McGee, G.C. Taylor, R. Amantea, P.K. Swain, S.M. Perlow, and M. ElSherbiny, **"**Silicon-based reconfigurable antennas-concepts, analysis, implementation, and feasibility,**"** *IEEE*

Transactions on Microwave Theory and Techniques, vol. 51, issue 6, pp. 1650-1661, June 2003.

[40] C. Zhang,; S. Yang, H.K. Pan, A. E. Fathy, S. El-Ghazaly, V. Nair, "Reconfigurable Antenna for Simultaneous Multi-Service Wireless Applications," *IEEE Radio and Wireless Symposium*, 2007 pp. 543 – 546 9-11 Jan. 2007.

[41] L.N. Pringle, P.H. Harms, S.P. Blalock, G.N. Kiesel, E.J. Kuster, P.G. Friederich, R.J. Prado, J.M. Morris, and G.S Smith, "A reconfigurable aperture antenna based on switched links between electrically small metallic patches," *IEEE Transactions on Antennas and Propagation*, vol 52, issue 6, pp. 1434 – 1445, June 2004.

[42] A. Mirkimali and P. S. Hall, "Log periodic printed dipole array for wideband frequency reconfiguration," IET Seminar on Wideband/Multi-band Antennas and Arrays for Civil or Defence Applications, London, 13 March 2008.

[43] S. Zhang, G.H. Huff, J. Feng, J.T. Bernhard, "A pattern reconfigurable microstrip parasitic array," *IEEE Transactions on Antennas and Propagation*, vol. 52, issue 10, pp. 2773 – 2776, Oct. 2004.

[44] C. Alakija and S.P. Stapleton, "A Mobile Base Station Phased Array Antenna", *International Conference on Selected Topics in Wireless Communications*, Vancouver, June 1992.

[45] C. A. Balanis, Antenna Theory: Analysis and Design, 3nd ed. Wiley & Sons, New Jersey, pp. 946-951, 2005.

[46] S. K. Palit and A. Hamadi, "Design and development of wideband and dual-band microstrip antennas," *IEE Proc.-Microw. Antennas Propag.*, vol. 146, no. 1, pp. 35-39, Feb. 1999.

[47] F. Tefiku and C. A. Grimes, "Design of broad-band and dual-band antennas comprised of series-fed printed-strip dipole pairs" *IEEE Transactions on Antennas Propagation*, vol. 48, no. 6, pp. 895-900, June 2000.

[48] P. Li, K. M. Kuk, and K. L. Lau, "A dual-feed dual-band L-probe patch antenna," *IEEE Transactions on Antennas & Propagation*, vol. 53, no. 7, pp. 2321-2323, July 2005.

[49] T.-Y. Yun, C. Wang, P. Zepeda, C. T. Rodenbeck, M. R. Coutant, M. Li, and K. Chang, "A 1-21 GHz low-cost, multi-frequency and full-duplex phased array antenna system," *IEEE Trans. Antennas Propag.*, vol. 50, no. 5, pp. 641-650, May 2002.

[50] R. Sarkis, C. Craeye, A. Ferreol, P. Morgand, "Design of triple band antenna array for GSM/DCS/UMTS handset localization," *Antennas and Propagation, 2009. EuCAP 2009. 3rd European Conference on* , vol., no., pp.3051-3054, 23-27 March 2009.

[51] N. Crispim, R. Peneda, C. Peixeiro, "Small dual-band microstrip patch antenna array for MIMO system applications," *Antennas and Propagation Society International Symposium, 2004. IEEE* , vol.1, no., pp. 237- 240 Vol.1, 20-25 June 2004.

[52] P. Li, K. M. Luk, and K. L. Lau, "A dual-feed dual-band L-probe patch antenna," *IEEE Trans. Antennas Propag.*, vol. 53, no. 7, pp. 2321-2323, July 2005.

[53] R. Pokuls, J. Uher, D.M. Pozar, "Dual-frequency and dual-poliarization microstrip antennas for SAR applications," *Antennas and Propagation, IEEE Transactions on* , vol.46, no.9, pp.1289-1296, Sep 1998.

[54] D.M. Pozar, S.D. Targonski, "A shared-aperture dual-band dual-polarized microstrip array," *Antennas and Propagation, IEEE Transactions on* , vol.49, no.2, pp.150-157, Feb 2001.

[55] L.L. Shafai, W.A. Chamma, M. Barakat, P.C. Strickland, G. Seguin, "Dual-band dual-polarized perforated microstrip antennas for SAR applications," *Antennas and Propagation, IEEE Transactions on* , vol.48, no.1, pp.58-66, Jan 2000.

[56] L. Yang, A. Rida, R. Vyas, and M. M. Tentzeris, "RFID Tag and RF Structures on a Paper Substrate Using Inkjet-Printing Technology," *IEEE Trans. Microwave Theory Tech.*, vol. 55, no. 12, pp. 2894-2901, Dec. 2007.

[57] M. Berggren, T. Kugler, T. Remonen, D. Nilsson, M. Chen, and P. Norberg, "Paper electronics and electronic paper," in *Proc. IEEE Polymers and Adhesives in Microelectron. Photon. Conf.*, Oct. 2001, pp. 300–303.

[58] D. C. Thompson, O. Tantot, H. Jallageas, G. E. Ponchak, M. M. Tentzeris, and J. Papapolymerou, "Characterization of Liquid Crystal Polymer (LCP) Material and Transmission Lines on LCP Substrates from 30 to 110 GHz," *IEEE Trans. Microwave Theory Tech.*, vol. 52, no. 4, pp. 1343-1352, April 2004.

[59] R. L. Li, K. Naishadham, T. Wu, L. Yang, M. M. Tentzeris, "Interleaved Dual-Band Printed Antenna Element for Phased Array Applications," *Antenna Applications Symposium*, 2009.

[60] Wonbin Hong, Behdad, N., and Sarabandi, K. , "Size reduction of cavity-backed slot antennas," *IEEE Transactions on Antennas and Propagation*, vol.54, no.5, pp.1461-1466, May 2006.

[61] Wonbin Hong, Sarabandi, K., "Platform Embedded Slot Antenna Backed by Shielded Parallel Plate Resonator," *IEEE Transactions on Antennas and Propagation*, vol.58, no.9, pp.2850-2857, Sept. 2010.

[62] R.L. Li, B. Pan, T. Wu, K. Lim, J. Laskar, M.M. Tentzeris, "Equivalent-Circuit Analysis and Design of a Broadband Printed Dipole with adjusted integrated Balun

and a Printed Array for Base Station Applications," *IEEE Transactions on Antennas and Propagation*, vol. 57, no. 7, July 2009.

[63] C. Ha, Y. Qian, T. Itoh, "A modified quasi-Yagi planar antenna with wideband characteristics in C-band," *IEEE Antennas and Propagation Society International Symposium*, vol 3, pp. 154-157, 8-13 July 2001.

[64] H.K. Kan, R.B. Waterhouse, A.M. Abbosh, M.E. Bialkowski, K.L. Chung, "A Simple Broadband Planar Quasi-Yagi Antenna" *IEEE TENCON 2006*. 14-17 Nov. 2006.

[65] B. Edward and D. Rees, "A broadband printed dipole with integrated balun," *Microwave Journal*, pp. 339-344, May 1987.

[66] P. Lindberg, E. Ojefors, Z. Barna, A. Thornell-Pers, A. Rydberg, , "Dual wideband printed dipole antena with integrated balun," *IET Microwaves, Antennas & Propagation*, Vol. 1, Iss. 3, pp. 707 – 711, June 2007.

[67] E.R. Brown, "RF-MEMS switches for reconfigurable integrated circuits," *IEEE Transactions on Microwave Theory and Techniques*, vol. 46, no.11, pp. 1868-1880, Nov.1998.

[68] T.A. Milligan, *Modern Antenna Design*, 2nd ed. McGraw-Hill, New York, pp. 106-107, 2005.

[69] Ku-Band Synthetic Aperture Radar Imagery, Sandia National Laboratories, http://www.sandia.gov/radar/imageryku.html.

[70] F.Akyildiz, W.Su, Y.Sankarasubramaniam, and E.Cayirci, "A survey on sensor networks", *IEEE Communication Magazine*, pp. 102-114, Aug 2002.

[71] A. Sleman and R. Moeller, "Integration of wireless sensor network services into other home and industrial networks; using Device Profile for Web Services (DPWS)," *IEEE Information and Communication Technologies: From Theory to Applications conference*, 2008.

[72] A. Hac, Wireless Sensor Network Designs, Wiley, 2003.

[73] D. Malan, T. Fulford-Jones, M. Welsh, and S. Moulton, "CodeBlue: An ad hoc sensor network infrastructure for emergency medical care," MobiSys 2004 Workshop on Applications of Mobile Embedded Systems, June 2004.

[74] Huntinton Botanical Gardens, SensorWare Systems. http://www.sensorwaresystems.com/historical/resources/huntington_sw31.shtml

[75] Solar Powered Wireless Sensor Networks Monitor Bridge Spans, MicroStrain Inc., Aug 2007.

http://microstrain.com/news/MicroStrain%20Solar%20Powered%20Bridge%20Pre
ss%20Release_rev%20d.pdf

[76] D. M. Doolin and N. Sitar. "Wireless sensors for wildfire monitoring," *Proceedings of SPIE Symposium on Smart Structures & Materials 2005*, San Diego, California, March 6-10, 2005.

[77] Prismark Wireless Technology Report, Prismark, Cold Spring Harbor, NY, 2009.

[78] M. Karpiriski, A. Senart, and V. Cahill, "Sensor networks for smart roads," *IEEE Pervasive Computing and Communications Workshops*, March 2006.

[79] H. Karl and A. Willig, Protocols and Architecture for Wireless Sensor Networks, Chichester: Wiley, 2005.

[80] D. Niyato, E. Hossain, and A. Fallahi, "Sleep and wakeup strategies in solar-powered wireless sensor/mesh networks: performance analysis and optimization," *IEEE Transactions on Mobile Computing*, vol. 6, issue 2, pp. 221-236, Feb 2007.

[81] Jiang, X.; Polastre, J.; Culler, D.; , "Perpetual environmentally powered sensor networks," *IEEE Information Processing in Sensor Networks Symposium* , pp. 463-468, 15 April 2005

[82] Chewed Antennas: Huntinton Botanical Gardens, SensorWare Systems. http://www.sensorwaresystems.com/historical/resources/pictures/hunt-011.shtml

[83] N. Henze, A. Giere, H. Fruchting, P. Hofmann, "GPS patch antenna with photovoltaic solar cells for vehicular applications," *IEEE VTC*, vol 1, pp.50-54, October 2003.

[84] J. Huang, "Mars rover antenna for solar-array integration," *The Telecommunications and Mission Operations Progress Report*, 42-136, pp. 1-13, October-December 1998.

[85] Shynu, S.V.; Ons, M.J.R.; Ammann, M.J.; Gallagher, S.; Norton, B.; , "Inset-Fed Microstrip Patch Antenna with Integrated Polycrystalline Photovoltaic Solar Cell," *EuCAP 2007*, pp.1-4, 11-16 Nov. 2007.

[86] Henze, N.; Weitz, M.; Hofmann, P.; Bendel, C.; Kirchhof, J.; Fruchting, H.; , "Investigation of planar antennas with photovoltaic solar cells for mobile communications," *Personal, Indoor and Mobile Radio Communications, 2004*vol.1, pp. 622- 626 Vol.1, 5-8 Sept. 2004.

[87] N. Nikolic, J.S. Kot, T.S. Bird, "Theoretical and experimental study of a cavity-backed annular-slot antenna," *Microwaves, Antennas and Propagation, IEE Proceedings* , vol.144, no.5, pp.337-340, Oct 1997.

[88] B. Jecko, "New kind of microstrip antenna: the monopolar wire-patch antenna ," *Electronics Letters* , vol.30, no.22, pp.1819, 27 Oct 1994.

[89] E. Seeley, J. Burns, K. Welton, "Cap-loaded folded antenna," *IRE International Convention Record* , vol.6, no., pp. 133- 138, Mar 1958.

[90] K.L. Lau, K.M. Luk, "A wide-band monopolar wire-patch antenna for indoor base station applications," *Antennas and Wireless Propagation Letters, IEEE* , vol.4, no., pp. 155- 157, 2005.

[91] H. Morishita, K. Hirasawa, K. Fujimoto, "Analysis of a cavity-backed annular slot antenna with one point shorted" *Antennas and Propagation, IEEE Trans. Antennas and Propagation*, vol.39, no.10, pp.1472 – 1478, October 1991.

[92] S. Nikolaou; R. Bairavasubramanian, C. Jr. Lugo, I. Carrasquillo, D.C. Thompson, G.E. Ponchak, J. Papapolymerou, M.M. Tentzeris, "Pattern and frequency reconfigurable annular slot antenna using PIN diodes," *Antennas and Propagation, IEEE Transactions on* , vol.54, no.2, pp. 439- 448, Feb. 2006.

[93] "A True System-on-Chip Solution for 2.4-GHz IEEE 802.15.4 and Zigbee Applications," TI, April 2009. http://focus.ti.com/lit/ds/symlink/cc2530.pdf

[94] "Synapse RF Engine," Synapse, 2008. http://www.synapse-wireless.com/documents/products/SYNAPSE_RF_Engine.pdf

[95] M. Winter, R.J. Brodd, "What Are Batteries, Fuel Cells, and Supercapacitors?" Chemical Reviews, vol. 104, no. 10, pp. 4259, 2004.

[96] Wiles, J., "Perspectives on PV," IAEI magazine, August 2004. http://www.iaei.org/subscriber/magazine/04_d/wiles.htm

[97] F. Zhang, Q. Wu, J-C Lee; , "A Simple T-shaped Wide-band Slot Antenna for Rectenna System," *Microwave Conference, 2008 China-Japan Joint* , pp.444-446, 10-12 Sept. 2008.

[98] S. Chaimool, S. Kerdsumang, P. Akkraeakthalin, and V. Vivek, "A broadband CPW-fed square slot antenna using loading metallic strips and a widened tuning stub," *TENCON 2004.*, vol.C, pp. 539- 542 Vol. 3, Nov. 2004.

[99] Sohn, Hoon; Farrar, Charles R.; Hemez, Francois M.; Shunk, Devin D.; Stinemates, Daniel W.; Nadler, Brett R.; Czarnecki, Jerry J. *A Review of Structural Health Monitoring Literature: 1996–2001*. Los Alamos, NM: Los Alamos National Laboratories. 2004.

[100] Michie, W.C., Culshaw, B., Roberts, S.J., and Davison, R., "Fiber Optic Technique for the Simultaneous Measurement of Strain and Temperature Variations in Composite Materials, *Fiber Optic Smart Structures and Skins IV,* SPIE, Vol. 1588, Boston, USA, 1991.

[101] Measuring Strain with Strain Gages, National Instruments, 2010. ftp://ftp.ni.com/pub/devzone/pdf/tut_3642.pdf

[102] Liu, L. and Yuan F. G., "Wireless sensors with dual controller architecture for active diagnosis in strcutural health monitoring", *Smart Mater. Struct.* **17**, 025026, 2008.

[103] Kurata N., Spencer B.F., and Ruiz-Sandoval M., "Risk monitoring of buildings with wireless sensor networks," *Struct. Control Health Monit.* 12 315–27, 2005.

[104] Glynne-Jones P, White NM. Self-powered systems: A review of energy sources. *Sensor Review*. 21(2):91-97, 2001.

[105] Wang L. and Yuan F.G., "Energy harvesting by magnetostrictive material (MsM) for powering wireless sensors," *SHM Proc.* SPIE 6529 652941, 2007.

[106] Beeby SP, Tudor MJ, White NM. Energy harvesting vibration sources for microsystems applications. *Meas. Sci. & Technol.*, 17(12):R175-R195, 2006.

[107] Yeager, D.J., Sample, A.P., Smith J.R., "WISP: A Passively Powered UHF RFID Tag with Sensing and Computation," *RFID Handbook: Applications, Technology, Security, and Privacy,* CRC Press, March 2008.

[108] Jia, Y., Sun, K., Agosto, F. J., and Quinones, M. T. "Design and characterization of a passive wireless strain sensor." *Measurement Science and Technology*, 17(11), 2869-2876, 2006.

[109] Loh, K.J., Lynch, J.P. and Kotov, N. (2006), "Passive Wireless Strain and pH Sensing using Carbon Nanotube-Gold Nanocomposite Thin Films," *Smart Struc. and Syst.*, Vol. 4, No. 5 pp.531-548, 2008.

[110] Thomson, D.J., Card, D., Bridges, G.E., "RF Cavity Passive Wireless Sensors With Time-Domain Gating-Based Interrogation for SHM of Civil Structures," *Sensors Journal, IEEE*, vol.9, no.11, pp.1430-1438, Nov. 2009.

[111] Deshmukh S. and Huang H., "Wireless interrogation of passive antenna sensors", *Meas. Sci. Technol.*, **21,** 035201, 2010.

[112] Penttila, K., Keskilammi, M,. Sydanheimo, and L., Kivikoski, M., "Radio frequency technology for automated manufacturing and logistics control," *International Journal Of Advanced Manufacturing Technology*, 31 (1-2): 116-124, 2006.

[113] Rida, A., Yang, L., and Tentzeris, M. *RFID-Enabled Sensor Design and Applications*, Artech House, Boston, 2010.

[114] Marrocco, G., Mattioni, L., Calabrese, C., "Multiport Sensor RFIDs for Wireless Passive Sensing of Objects—Basic Theory and Early Results," *APT, IEEE*, vol.56, no.8, pp.2691-2702, Aug. 2008.

[115] Garg, R., Bhartia, P., Bahl, I., and Ittipiboon, A., *Microstrip Antenna Design Handbook*, Boston: Artech House, 2001.

[116] Tata U, Huang H, Chiao J C and Carter R, "Exploiting patch antenna for strain measurement" Meas. Sci. Technol., vol. 20 015201, 2009.

[117] Liu, J., Gan, D., Hu, C., Kiene, M., Ho.P.S., Volksen, W., and Miller, R.D., Porosity effect on the dielectric constant and thermomechanical properties of organosilicate films, *Appl. Phys. Lett.* vol.81, pg4180, 2002.

[118] Baklanov, M.R., and Maex, K, "Porous low dielectric constant materials for microelectronics," *Phil. Trans. R. Soc. A*, vol. 364 no. 1838 201-215, 2006.

[119] "Porosity," Wikipedia, 2010. http://en.wikipedia.org/wiki/Porosity.

[120] "PTFE data sheet," Bearing works Inc., 2010. http://www.bearingworks.com/content_files/pdf/retainers/PTFE%20datasheet.pdf

[121] Jackson, K.M., "Fracture strength, elastic modulus and Poisson's ratio of polycrystalline 3C thin-film silicon carbide found by microsample tensile testing," Sensors and Actuators A: Physical. Vo. 125, 1, pg. 34-40, Oct 2005.

[122] Heinola, J.-M.; Latti, K.-P.; Silventoinen, P.; Strom, J.-P.; Kettunen, M.; , "A method to evaluate effects of moisture absorption on dielectric constant and dissipation factor of printed circuit board materials," *Advanced Packaging Materials: Processes, Properties and Interfaces, 2004. Proceedings. 9th International Symposium on* , vol., no., pp. 241- 246, 2004.

[123] Climate/humidity table. http://www.tis-gdv.de/tis_e/misc/klima.htm